MODELLING OF GAS INJECTION WITH CONSTANT PRESSURE BOUNDARIES

XIAOLONG LIU

Modelling of Gas Injection with Constant Pressure Boundaries

by

©Xiaolong Liu

A Thesis submitted to the School of Graduate Studies in partial fulfillment of the requirements for the degree of

Master of Engineering

Faculty of Engineering and Applied Science

Memorial University of Newfoundland

March 2013

St. John's Newfoundland

Abstract

Gas injection is one of the most widely applied enhanced oil recovery methods. Existing analytical solutions to gas injection processes are based on the standard fractional flow assumption of a constant flow rate. Realistically, most reservoirs are operated with constant injection and production pressures where the total volumetric flux varies with time. An analytical model for the gas injection process with constant pressure boundaries and a numerical compositional model are developed in this thesis.

By using the standard fractional flow analysis, the Riemann problem associated with the ternary gas injection process is solved. Based on the solution of the eigenvalue and elementary waves, the time dependent total flux, pressure distribution, and saturation profile with constant pressure boundaries are directly calculated by applying the approach developed by Johansen and James (2012). The analysis of the ternary gas injection problem provides the fundamental method for systems with higher numbers of components.

The solution from the two-dimensional numerical model interprets the effects from the component property and heterogeneity in the reservoir to the displacement performance. The analytical solution is compared with the numerical solution. It shows that the grid block refinement plays a significant role in the behaviour of the numerical solution. By studying both the analytical and numerical methods, agreement and disparity of solutions between the two approaches can be investigated.

Acknowledgements

As a member of the MUN Enhanced Oil Recovery research group, I conclude my research and describe my main contribution in this thesis.

First of all, I would express my deep gratitude to my supervisors, Dr. Lesley James and Dr. Thormod Johansen. I have enjoyed the time learning, discussing and working together with you. I strongly admire your wisdom and sense of humour. You enlightened and guided me through each step toward the accomplish of this thesis. Thank you so much for your kind support and insightful advice whenever I have encountered difficulties in the research work or life.

I want to thank my colleagues in the research group: Jie Cao, Nan Zhang, Huan Yang, Ali Souri Laki and Hashem Nekouiewho helped me greatly with the modelling techniques; Xiaoyan Tang, Hskandari Saeed, Mahsa Moayed who shared with me research information. I also want to express my appreciation to Norah Hyndman who helped me with thesis correction.

Finally, to my dear parents and grandmother, it is everything you did that I could complete my study far abroad. You are supporting, concerning and taking care of me through all my life. with your support, care and protection, I will always feel safe and warm. Also I want to thank Aunt Liu, Aunt Yang, Uncle Liu for your support. Thank you to my best friends: Xing Xin, Yu Huang, Xiaohui Zheng, Tian Wang, Chen Yang, Tongrong Xing, and etc. We had so many precious memories together.

Table of Contents

List of Tables

List of Figures

Nomenclature

η	Tie-line parameter
$\hat{f}$	Fugacity
Λ	Eigenvalue
λ	Mobility
μ	Viscosity
ω	Mass concentration
ϕ	Porosity
ρ	Phase molar density
ρ_c	Component molar density
τ	Pore volume injected (dimensionless time
θ	Tie-line interception
φ	Tie-line slope
ξ	Dimensionless distance
C	Overall volume fraction of a component

c	Phase volume fraction of a component
F	Overall fractional flow function
f	Fractional flow function
K	Permeability
K_i	Equilibrium ratio K-value
L	Length
m	Mass
nc	Number of component
np	Number of phase
nt	'Nontie-line' as per equation 3.40
p	Pressure
P_c	Capillary pressure
R	Universal gas constant
S	Saturation
S_{cg}	Critical gas saturation
S_{or}	Residual oil saturation
S_{wc}	Connate water saturation
t	Time (t = 'tie line' as per equation 3.40
u	Volumetric flux

V_b	Bulk volume
V_i	Propagation velocity
v_i	Elementary wave
x	Grid size in x direction
y	Grid size in y direction
y_{ij}	Phase mole fraction of a component
Z	Compressibility factor

Chapter 1

Introduction

1.1 Enhanced Oil Recovery

Enhanced Oil Recovery (EOR) is a method to recover additional oil or gas by injecting fluids that are not initially contained in the reservoir (Lake, 1989). Production from a reservoir is normally driven by pressure depletion along with gas cap or aquifer in early production life. Secondary stage recovery by water flooding or gas injection may be implemented for the purpose of maintaining reservoir pressure.The purpose of tertiary recovery is to maximize the recovery of the residual reservoir fluid. Normally an EOR process is applied as a secondary or tertiary displacement method (Lake, 1989). A variety of EOR methods have been developed and commercially applied in fields during the past decades. Most EOR methods have the features of improvement in residual oil recovery, however they are more expensive in comparison to conventional production operations. Therefore, early evaluation work including reservoir simulation and laboratory experiments play an important role in EOR project planning.

Existing EOR methods include: polymer flooding, alkaline injection, gas injection,

CO_2 injection and flue gas injection. Some of the methods, for example polymer flooding, have been successfully implemented in many fields, while others have shown limitations in performance or economics. Gas injection and flue gas injection have been widely studied for potential applications due to their potential environmental benefits. The feasibility of flue gas injection application in offshore Newfoundland, Canada, has been studied by Thomas *et al.* (2010) using data from the White Rose field screening study.

The application of an EOR method to a particular field can be summarized as follows: EOR method selection, geological studies, numerical modelling, economic analysis, design of EOR process parameters and project implementation (Hite *et al.*, 2004). Increased demand for oil supplies necessitates increased research and development of EOR processes. Modelling is one of the critical stages of EOR implementation, hence the development of its theories and techniques play a key role.

1.2 Reservoir Simulation Methods

EOR processes can be modelled by a system of flow and property behaviour equations. Essential flow equations with simplified property correlations and assumptions can be solved analytically and the solution obtained can show the major principles, driving mechanisms, and relationships between parameters. However, due to the simplified assumptions, the solutions will not accurately reflect all fluid and phase behaviours occurring during the displacement process. If more complicated equations and correlations are incorporated in the model system, the analytical approach will reach its limit. When incorporating comprehensive aspects of an EOR process into the model, for example phase density change, numerical modelling techniques are employed which

are extremely time consuming.

A water flooding process can be modelled by using a black oil model in which oil and water phases are treated as two immiscible components, where mass is considered to be conserved for each phase. When we need to track each component within the fluid, a compositional model can be used. A compositional model can be summarized as a component based model in which the mass conservation equation is applied to each single component. Mass conservation for a single component can be expressed as:

$$\textit{For an arbitrary control volume over } \Delta t: \ \Delta m(i) = q_{in}(i) - q_{out}(i)$$

where $\Delta m(i)$ is the mass change of component i over a time period Δt, $q_{in}(i)$ and $q_{out}(i)$ are the mass flow of component i into and out of the control volume, respectively, over the same time period Δt. For an n-component displacement system, n - 1 mass conservation equations will lead to an n - 1 partial differential equation (PDE) system to solve. The PDE system could either be a linear or a strongly coupled, nonlinear system for which unknowns include: component concentration, pressure, phase volume fraction (phase saturation), fluid and rock properties (including viscosity, density, porosity etc.). A compositional simulator is a solver for the PDE system with all unknowns and properties being updated at each time step. That solutions of saturation profile, component concentration profile and pressure distribution etc. are generated for evaluation and analysis.

1.3 Standard Fractional Flow Theory

Modelling of EOR processes and general reservoir simulation have two principles: fractional flow theory and phase behaviour (Lake, 1989). Fractional flow theory was

first developed for a classic water-displacing-oil problem by Buckley and Leverett (1941). The flux of water and oil phases are denoted as $u_w, and\ u_o$ and total flux is denoted as $u_T = u_w + u_o$. The assumptions of fractional flow theory are:

- One-dimensional medium
- Fluid and rock are incompressible
- The displacement process is isothermal
- Total flux u_T is constant

The mass conservation equation and fractional flow function for the water phase are written as:

$$\phi\frac{\partial S_w}{\partial t} + \frac{\partial u_w}{\partial x} = 0 \tag{1.1}$$

$$f_w = \frac{u_w}{u_T} \rightarrow u_w = u_T f_w \tag{1.2}$$

Substituting Eq.1.2 into Eq.1.1 and taking the constant u_T out of the partial derivative term, we have:

$$\phi\frac{\partial S_w}{\partial t} + u_T\frac{\partial f_w}{\partial x} = 0$$

After rearrangement:

$$(\frac{\partial S_w}{\partial t})_x = -\frac{u_T}{\phi}(\frac{\partial f_w}{\partial x})_{S_w} \tag{1.3}$$

The above equation can be transformed as:

$$(\frac{\partial x}{\partial t})_{S_w} = \frac{u_T}{\phi}(\frac{\partial f_w}{\partial S_w})_x \tag{1.4}$$

Eq.1.4, shows that for a fixed value of water saturation S_w, the traveling velocity $\frac{\partial x}{\partial t}$ is equal to $\frac{u_T}{\phi}\frac{\partial f_w}{\partial S_w}$. Since f_w, as defined in Eq.1.2, is a function of S_w, the plot of the f_w curve can be shown in Fig.1.1 and $\frac{\partial f_w}{\partial S_w}$ is therefore the slope of the tangent

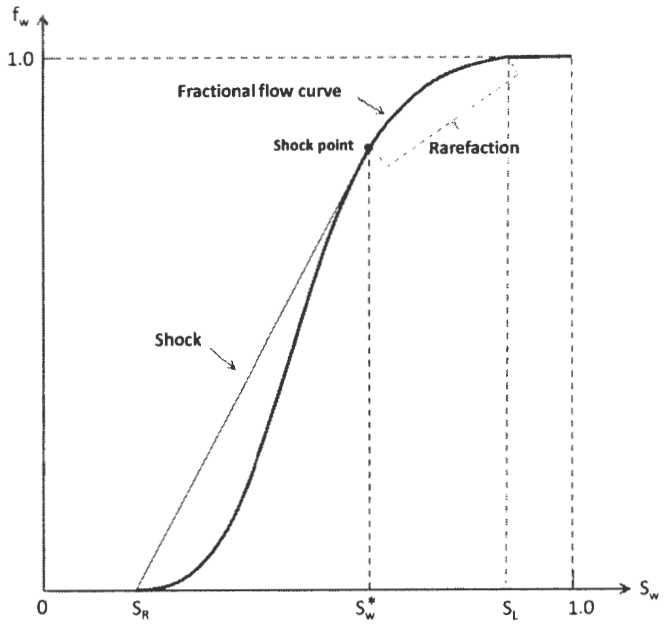

Figure 1.1: A typical fractional flow curve for water flooding

to the f_w curve. Moving from the left state of S_w (left state of S_w is the injection water saturation, it normally equals 1 - S_{or}, where S_{or} is the residual oil saturation) to the right state of S_w (right state of S_w is the initial water saturation, it is normally the connate water saturation S_{wc}), the propagation velocity of each saturation value can be obtained by calculating the slope of the tangent at this saturation point on the fractional flow curve. In Fig.1.1, if we trace from S_L (left hand side of water saturation) to S_R (right hand side of water saturation) along the f_w curve, there is a point from which the slopes start to decrease. A shock will be needed at this point, otherwise it leads to the unphysical solution of multiple saturation values existing at one location.

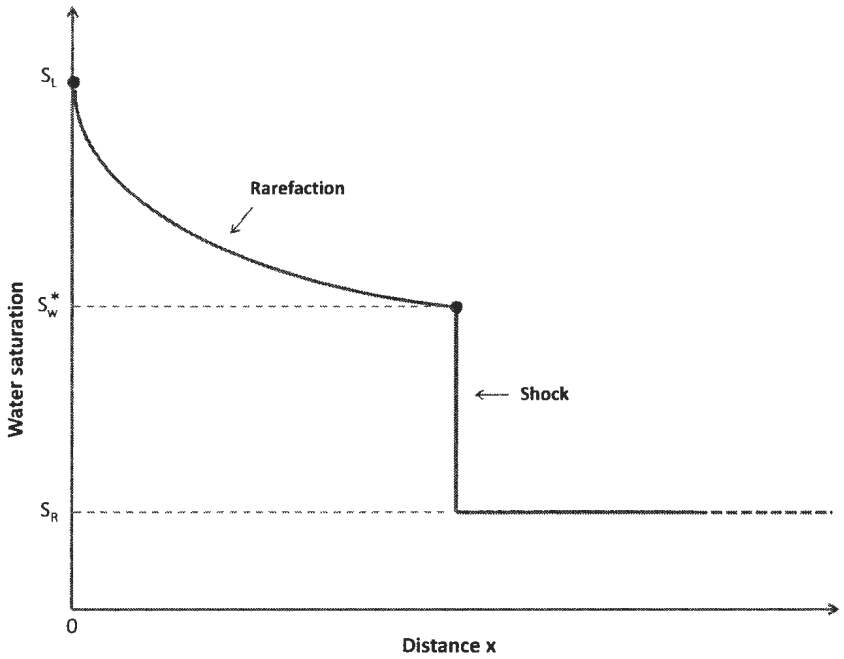

Figure 1.2: A sample saturation profile solution of water flooding

A shock is a jump or discontinuity between two points on the fractional flow curve. A rarefaction is a continuous variation along the fractional flow curve. Upstream or ahead of the shock, the slope of the tangent is equal to the shock slope as shown in Fig.1.1. By using this equality condition, the shock point saturation can be determined using an iterative approach, or it can be determined graphically by constructing a straight line from S_R tangent to the fractional flow curve as shown in Fig.1.1. Knowing the rarefaction, shock and the corresponding saturations, the solution of velocities for each saturation can be constructed. A typical velocity solution is shown in Fig.1.2, this analysis approach is known as fractional flow theory. The fractional flow theory was developed from the classic water-oil displacement problem. It is also applicable to other displacement problems including EOR processes. Assuming a constant flow rate, u_T, the governing system of equations can be simplified and solved analytically using the method of characteristics.

1.4 The IMPES Method

The acronym IMPES stands for 'Implicit in Pressure and Explicit in Saturation' as introduced by Coats (1968) and has been generalized and applied in different models. The water flooding problem from Section 1.3 is used as an example to introduce the IMPES method. The mass conservation equation for the oil phase can be written as:

$$\phi \frac{\partial S_o}{\partial t} + \frac{\partial u_o}{\partial x} = 0 \tag{1.5}$$

Sum Eq.1.1 and Eq.1.5, we have:

$$\phi \frac{\partial}{\partial t}(S_w + S_o) + \frac{\partial}{\partial x}(u_w + u_o) = 0 \tag{1.6}$$

The water phase and oil phase occupy the entire pore volume, hence we have: $S_w + S_o = 1$. The flux of water (u_w) and oil (u_o) can be expressed as functions of S_w and p by using Darcy's law:

$$u_w = \frac{K k_{rw}(S_w)}{\mu_w} \frac{\partial p}{\partial x} \tag{1.7}$$

$$u_o = \frac{K k_{ro}(1 - S_w)}{\mu_o} \frac{\partial p}{\partial x} \tag{1.8}$$

where k_rw and k_ro are relative permeability of water and oil phase, p is the pressure (we assume the capillary pressure is zero that the pressure of water phase and oil phase are identical, p therefore is the pressure of the entire fluid in the pore volume). Eq.1.6 can then be expressed as:

$$u_w(S_w^n, p^{n+1}) + u_o(S_w^n, p^{n+1}) = 0 \tag{1.9}$$

where n represents the time step. In the above expression, we treat the pressure as an unknown and use the known quantity S_w^n for the flux calculation. The unknown p^{n+1} can be solved from Eq.1.9. Eq.1.1 can be discretized as:

$$\phi \frac{S_w^{n+1} - S_w^n}{\triangle t} + \frac{u_{w,i+1} - u_{w,i}}{\triangle x} = 0 \tag{1.10}$$

By substituting p^{n+1} into the equation above, S_w^{n+1} can be solved so that the pressure and saturation are both obtained for the next time level. Eq.1.9 leads to an linear equation system and the pressure unknown can be expressed as an unknown vector. This method of formulating the conservation equations and solving the pressure unknowns is called the IMPES method. The fully implicit method is to treat both saturation and pressure as unknowns in Eq.1.9 and use an iterative method to solve the unknowns.

1.5 Problem Statement

The mathematical system of equations describing the fluid displacement process can be solved analytically under certain simplified conditions. If one tries to model more complex or realistic scenarios beyond the simplified cases outlined above, the limit of analytical solutions is soon reached and numerical methods are required. The analytical method provides fundamental theories and direct analysis approaches for all simulation work while numerical method provides the approach for complex and realistic simulation scenarios. Development in both analytical and numerical methods therefore are important modelling techniques.

As stated in the previous section, the fractional flow theory is based on the assumption of constant total flux, u_T. For most laboratory and real field gas injection operations,

fixed injection and production pressures are applied, hence the constant u_T assumption is invalid. Under fixed pressure boundaries, u_T will be a time dependent variable as is the pressure distribution. Johansen and James (2012) developed the generalized calculation and analysis approach for the fixed pressure boundaries (Referring to the pre-print in Appendix.C). If u_T is either constant or time dependent, the eigenvalue solution and elementary wave structure remain the same for both conditions. Based on the analysis of the three-component problem developed by Johansen and Winther (1990), the eigenvalue and elementary wave solution are calculated. The solution to the three-component problem with constant pressure boundaries, is provided by applying the generalized calculation method.

A two-dimensional numerical compositional model incorporating rock and fluid properties is developed. Based on the work by Nghiem et al. (1981), a modified pressure and concentration solving scheme is applied. Rather than using an iterative method for solving for pressure, a linear solver is used. A single point upstream scheme is used to solve for concentrations. By studying both the analytical and numerical methods, agreement and disparity of solutions between the two approaches is investigated.

1.6 Thesis Outline

1.6.1 Chapter summary

Chapter 1

The definition and basic categories of EOR processes are discussed in Chapter 1.The development of the work in this thesis starts from classic fractional flow theory and numerical compositional modelling. Fundamental methodology including sample application of fractional flow theory to a water-oil displacement problem and the struc-

ture of a numerical compositional model is briefly discussed.

Chapter 2

Chapter 2 includes a review of the literature regarding application of fractional flow theory, solution of the three-component gas injection process, and the fractional flow analysis for a multi-component problem with constant pressure boundaries. A literature review of the numerical compositional simulation method is also included.

Chapter 3

This chapter illustrates the construction of the solution of the three-component gas injection problem under fixed pressure boundaries. Eigenvalues, elementary waves and compositional paths with the standard fractional flow assumption are generated. Based on the generated eigenvalue and elementary wave solution, the time dependent total flux and pressure distribution are the calculated using the generalized approach by Johansen and James (2012). This chapter describes the full analytical model for three-component gas injection problem with constant pressure boundaries.

Chapter 4

In Chapter 4, a numerical compositional model is developed. Starting from the governing equation system, this chapter introduces the model structure, the method for solving the equation system and fluid and rock property correlations. Chapter 4 also includes two case studies of three-component gas injection simulation in one-dimensional and two-dimensional flow.

Chapter 5

Chapter 5 includes two case studies. The first case study uses different components to

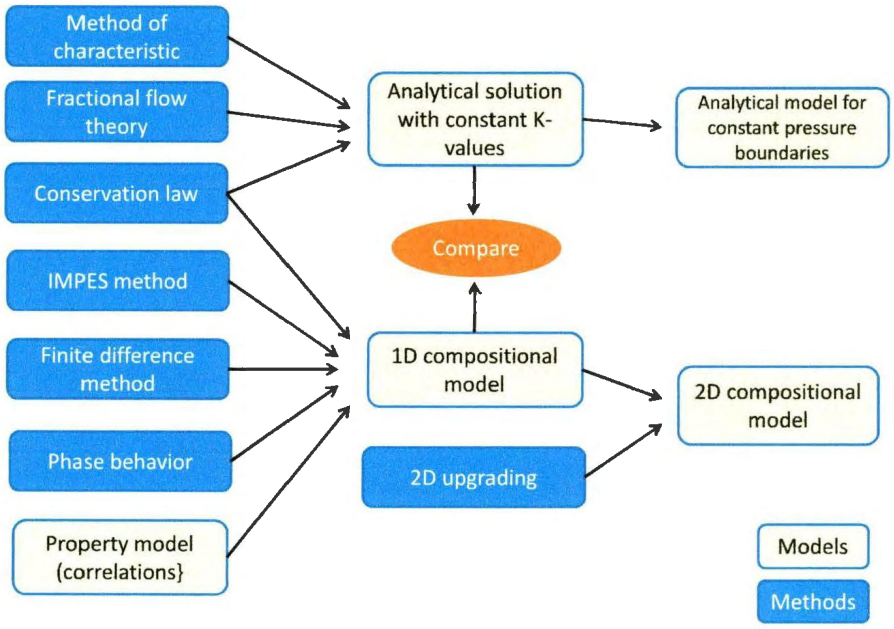

Figure 1.3: Research concept map

show how the component property affect the simulation solution and the second one is a 2D simulation to discuss the effect from heterogeneity. A comparison between the numerical and analytical solutions are also provided in this chapter which illustrates the effect from numerical dispersion.

Chapter 6

This chapter concludes the work in this thesis and discusses recommendation for future potential extension of the research.

1.6.2 Research concept map

A research concept map illustrates the knowledge structure associated with the research topic. As shown in Fig.1.3, the relationship between the key methods that have been applied during the development of the research is presented. The concept

map outlines the research path of this thesis. Starting from the fundamental methods, including method of characteristic, fractional flow theory, conservation law etc., the analytical model under constant pressure boundaries and a numerical compositional model are developed. The solution of elementary waves is used to validate the numerical model.

Prior to the analytical model developed in this thesis as shown in the concept map, numerical simulation is the only approach to model the displacement process. The work in this thesis fills the blank of the constant pressure boundary gas injection modelling and provides the analysis approach for such displacement problem.

Chapter 2

Literature Review

2.1 Application of Fractional Flow Theory

The fractional flow theory developed by Buckley and Leverett (1941) describes a simplified one-dimensional water flooding problem. The fractional flow function for the water phase is defined as the fraction of the displacing fluid flux and the total volumetric flux. As an unique function of water phase saturation, the fractional flow function can be plotted versus water saturation and shown as a fractional flow curve. The expression of the travelling velocity for a fixed saturation is the derivative of the fractional flow function with respect to water saturation. Knowing the propagation velocities of the water saturations, the wave solution to the water flooding problem can be constructed. However, a straight forward construction of the solution along the fractional flow curve will lead to an unphysical water saturation distribution pattern (multiple saturations at one location). Therefore, a shock is needed for the solution. The approach to determine the shock point saturation on the fractional flow curve and the effect from the viscosity ratio and capillary pressure are also provided in the fractional flow theory development work. The fractional flow theory has become one

of the essential approaches in reservoir simulation and has been applied and extended to many different types of displacement problems (Lake, 1989).

The extended application of the fractional flow theory to EOR processes has been provided by several authors. Polymer flooding is one of the most widely applied EOR methods with more complexity than water flooding. Patton*et al.* (1971) applied the fractional flow theory with the method of characteristics to a linear polymer flooding problem and examines the numerical modelling solution against the developed analytical solution. By assuming that water viscosity is a function of polymer concentration only, it is shown that two fractional flow curves correspond to each of the viscosity values present. When constructing the wave solution using fractional flow theory, a shock connects the two fractional flow curves corresponding to the two states of polymer concentration. Compared to the water flooding solution, Patton *et al.* (1971) proved that the fractional flow theory could be applied to a three component case (water, oil, polymer) with more shocks and constant states appearing in the solution.

The solution to the carbonated water flooding problem is solved by Nevers *et al.* (1964). The solution interprets the transferring of carbon dioxide within the phases and the effect of viscosity reduction and swelling in the oil phase. Fractional flow theory is also applied to alcohol displacement by Taber *et al.* (1961). Welge *et al.* (1961) developed an analytical method for enriched gas displacement process. Shutler and Boberg (1972) provide an analytical solution to steam flooding. A summary of fractional flow theory applied to low-tension flooding, hot water flooding, and two and three phase flow is provided by Pope (1980).

2.2 The Riemann Problems for Gas Injection Modelling

The conservation law with discontinuities and piecewise constant data is know as Riemann problem. The mass conservation equations for used in fractional flow theory to model EOR processes yield a hyperbolic partial differential equation system. To construct the solution of the hyperbolic system is to solve the associated Riemann Problem where the injection fluid composition (or saturation) and the initial reservoir fluid composition (or saturation) are the initial states. A water flooding problem can be treated as a two-component problem, while other EOR processes can generally be analyzed as three- or multi-component problems. The three-component system is a typical problem that interprets significant features of the displacement mechanism yet is sufficiently simple to be solved analytically. The sample calculation and case study of the analytical model in this thesis will be using a three-component gas injection system.

Johansen and Winther (1990) gave a comprehensive analysis of three- and four-component Riemann problems. By defining the fractional flow function and choosing the independent variables for the fractional flow function, the model for a three-component, two phase flow problem was re-formulated to a simplified form. The expressions of the two associated eigenvalues and eigenvectors for the re-formulated hyperbolic system were solved. They show that the elementary wave solution consists of rarefaction waves, shock waves and linear waves. It was proved that the elementary waves connecting each of the states are unique solutions to the Riemann problem.

By applying a similar analysis approach, Johansen and Winther (1988, 1989) proved

the solution and analysis for single and multi-component polymer flooding problems. The single-component polymer flooding problem with one chemical component being dissolved in the injected water was analyzed as a three-component Riemann problem. They showed that there are two fractional flow curves associated with each of the polymer concentration states with a shock wave connecting the two fractional flow curves.

Based on the analysis of the Riemann problems for conservation law modelling, gas injection process can be modelled by specifying each of the components to be the gas and oil constituents. Orr (2007) provides the analysis and modelling techniques for the gas injection process using both analytical and numerical methods.

2.3 Solution for Constant Pressure Boundaries

All fundamental work on the analysis of EOR process modelling problems is based on the standard fractional flow theory with the assumption of a constant total volumetric flux. This assumption is invalid for displacement processes with fixed pressure boundaries. In the case of constant pressure boundaries, the total flux and the pressure distribution are time dependent. Johansen and James (2012) developed a method for calculating the time dependent total flux, pressure distributions and breakthrough time of each state. A fully analytical model for constant pressure boundaries displacement can be developed instead of the conventional numerical method. In their work, the elementary wave analysis of a general multi-component Riemann problem, and the approach for calculating the time dependent total flux and pressure distribution at different stages of breakthrough of elementary waves are provided. The saturation (or concentration) propagation profile, under constant pressure boundaries, can be

constructed using the calculated total flux at each point in time. Prior to this work, the numerical method was the only approach to obtain a solutions to the constant pressure boundary problem.

2.4 Numerical Compositional Simulation

2.4.1 The IMPES method

The IMPES formulation method is one of the principle methods used in numerical simulation. Coats (1968) illustrates this formulation method to solve the pressure and saturation unknowns for a black oil reservoir model. The IMPES method has been generalized for an arbitrary number of components and it is still being applied in various reservoir simulation models. An alternative approach is the fully implicit method, in which the pressure and saturation are both treated as unknowns. The unknowns are solved by using an iterative method, for example the Newton–Raphson method. Comparing iterative methods, the fully implicit method is more time consuming compared to the IMPES method. But the fully implicit method is more stable because due to the fact that the waves exhibit more smearing.

2.4.2 Numerical simulation using EOS based flash calculation

One of the major features of the gas injection process is the mass transfer of the components within the phases. In order to model the gas injection process and track the distribution of each component, a compositional model can be applied. A compositional model is based on the mass conservation for each single component presented in the fluid system containing the injection and initial reservoir components. The mass transfer behaviour and fluid pressure, volume and temperature (PVT) properties can be modelled using equation of state (EOS) based flash calculation, where we assume

the fluid system is in thermodynamic equilibrium.

The method of incorporating EOS based flash calculation into a compositional model was introduced by Nghiem *et al.* (1981). The mass conservation equations were formulated into the pressure equations for solving the pressure unknown using the IMPES method. The updated pressures are used to calculate overall compositions of each component. By performing a flash calculation on the updated pressure and overall composition at each grid block using the Peng-Robinson EOS, the phase saturation and PVT properties at each grid block are calculated. When all variables are updated for the next time step, the calculation is again performed for that time step. An iterative procedure for solving the pressure unknowns was introduced requiring the assembly of the Jacobin matrix and also the convergence of solution. In the scheme of finite different approximation, a two-point upstream method is used for the purpose of numerical stability.

The compositional model developed by Nghiem *et al.* (1981) provide a fundamental method for the numerical compositional simulation using flash calculation. Various compositional models have been developed including different features for the purpose of representing a particular behaviour in different displacement scenarios.

2.4.3 Flow in heterogeneous media

A homogeneous medium is often assumed in simulation, hence the use of a single permeability value. However, real reservoir formations are heterogeneous. The porous media properties vary with location and orientation. Permeability is one of the basic reservoir parameters, and it is a function of the local pore size, grain size and depositional history. The heterogeneity of a reservoir is difficult to precisely define yet it has

a significant effect on the displacement performance. The variation of permeability will strongly affect the fluid flow path and component distribution within the reservoir. When numerical simulation is performed in heterogeneous media, dispersion both from the numerical method and from the heterogeneity will occur and affect the simulated displacement behaviour.

Law (1944) studied the horizons from a sandstone reservoir and shows the log-normal reservoir permeability distribution. Lambert (1981) and Jensen *et al.* (1987) provide the frame work of modelling permeability distribution and estimating the effective permeability based on the statistical analysis. They concluded that the permeability is not necessarily log-normally distributed. Arya *et al.* (1988) analyzes the effect from heterogeneity on numerical simulation dispersion. Based on a two-dimensional randomly distributed permeability numerical model, a miscible displacement was modelled showing that variation in heterogeneity significantly affects dispersion.

Chapter 3

Analytical Model for the Three-Component System with Constant Pressure Boundaries

Existing analytical solutions to the gas injection problem are based on the assumption of a constant volumetric flux. Injection processes operated under the constant injection and production pressures exhibit time variable volumetric flux for most real field applications. In this thesis, the solution for a three-component linear gas injection problem with constant pressure boundaries is provided by applying the generalized approach developed by Johansen and James (2012).

Hence, we start with the formulation of the conservation equation system for the three-component problem with constant total flux. The solution to the system of conservation equations for a three-component gas injection problem has two associated eigenvalues. The two eigenvalues and elementary waves are identified using the fractional flow theory with the constant total flux assumption. Based on the

eigenvalue and elementary wave solution, we calculate the time dependent total flux, breakthrough time of each elementary wave, saturation profile and pressure distribution with given constant pressure boundaries. The behaviour of the total flux, during each elementary wave breakthrough, is interpreted from the solution.

A fully analytical model for the three-component gas injection problem is developed instead of the conventional numerical method. Prior to this work, the numerical method was the only possible approach to obtain the solutions for constant pressure boundaries. This application for the three-component problem demonstrate the fundamental calculation method that could be applied to the multi-component gas injection problem.

3.1 Material Balance Equation

The essential equations behind reservoir simulators are derived from the basic material balance equations. In general, the material balance equation is described as: the net flow of the fluid equal to the volume change of the fluid within an arbitrary fixed volume over the same time period. All the formulae or equations are derived for one-dimensional flow. The following derivation refers to Lake (1989).

We define the 'mass concentration' ω for an arbitrary fixed bulk volume V:

$$\omega = \frac{m_i}{V} \tag{3.1}$$

where m_i is the mass of component i. The bulk volume is a porous medium in our case, so the flowing fluid will not occupy the entire bulk volume. Therefore, the rate

of change of mass is:

$$\frac{\partial}{\partial t}\iiint_V \omega dV \tag{3.2}$$

The net mass flowing into the volume V per unit time is:

$$-\iiint_{S(V)} \vec{F}\cdot\vec{n}dS \tag{3.3}$$

where $\vec{F}$ is the mass flux , $\vec{n}$ is the outer surface unit normal. Addition (injection) or removal (production) of the fluid from V can be expressed as:

$$\iiint_V \tilde{q}dV \tag{3.4}$$

where $\tilde{q}$ is the mass injection or removal per unit time and unit bulk volume. According to the mass conservation for V:

$$\frac{\partial}{\partial t}\iiint_V \omega dV = -\iiint_{S(V)} \vec{F}\cdot\vec{n}dS + \iiint_V \tilde{q}dV \tag{3.5}$$

Using the Divergence theorem and assuming zero source term ($\tilde{q}=0$), we have:

$$\iiint_V (\frac{\partial \omega}{\partial t} + \nabla\cdot\vec{F})dV = 0 \tag{3.6}$$

$$\frac{\partial \omega}{\partial t} + \nabla\cdot\vec{F} = 0 \tag{3.7}$$

we can express ω for component i in terms of moles:

$$\sum_{j=1}^{np} \phi y_{ij}\rho_j S_j; i = 1, ..., nc \tag{3.8}$$

where ϕ is porosity, ρ_j is molar density of phase j, S_j is saturation of phase j, y_{ij} is the mole fraction of component i in phase j, nc is the number of components and

np is the number of phases. The mass flux of component i in phase j is denoted as $\vec{F}_{ij}$ which can be expressed by $y_{ij}\rho_j\vec{u}_j$. We use Darcy's law for the volumetric flux of phase j: $\vec{u}_j$:

$$y_{ij}\rho_j\vec{u}_j = y_{ij}\lambda_j\nabla p_j \tag{3.9}$$

$$\lambda_j = \frac{Kk_{rj}}{\mu_j}\rho_j; j = 1, ..., np \tag{3.10}$$

where K is the reservoir permeability, k_{rj} and μ_j are the relative permeability and viscosity for each phase, and λ is the phase mobility, respectively. Substituting Eq.3.8 and Eq.3.10 into Eq.3.7, and ignoring the gravity term, the resulting material balance equation is:

$$\frac{\partial}{\partial t}(\sum_{j=1}^{np}\phi y_{ij}\rho_j S_j) + \nabla[\sum_{j=1}^{np}(y_{ij}\lambda_j\nabla p_j)] = 0; i = 1, ..., nc \tag{3.11}$$

Eq.3.11 can be simplified for one-dimensional flow as:

$$\frac{\partial}{\partial t}(\sum_{j=1}^{np}\phi y_{ij}\rho_j S_j) + \frac{\partial}{\partial x}[\sum_{j=1}^{np}(y_{ij}\lambda_j\frac{\partial p_j}{\partial x})] = 0; i = 1, ..., nc \tag{3.12}$$

The conservation equation expressed in Eq.3.12 will be simplified to the governing equations for the analytical model.

3.2 Eigenvalue and Composition Path

The governing equations for the three-component problem are derived from the general material balance equation. The eigenvalues and composition path solution are solved for the three-component problem. The method used for solving the eigenvalue and composition path solution and associated derivation is given by Johansen and Winther (1990).

3.2.1 Governing equations for the analytical model

3.2.1.1 Fractional flow function

From the expression of volumetric flux u_j of phase j, the fractional flow function of the corresponding phase f_j is defined as:

$$f_j = \frac{u_j}{u_T} = \frac{\frac{Kk_{rj}}{\mu_j}\frac{\partial p}{\partial x}}{u_T} \tag{3.13}$$

$$u_T = \sum_{j=1}^{np} u_j \tag{3.14}$$

where u_T is the total volumetric flux of the entire flowing fluid. Based on the definition shown in Eq.3.13, the exact expression of the fractional flow function depends on the relative permeability model used. In this chapter, we use the relative permeability model developed by Brooks and Corey (1964) which states that the oil relative permeability (k_{ro}) and gas relative permeability (k_{rg}) can be expressed as:

$$k_{ro} = \left(\frac{1 - S - S_{or}}{1 - S_{cg} - S_{or}}\right)^2 \tag{3.15}$$

$$k_{rg} = \left(\frac{S - S_{cg}}{1 - S_{cg} - S_{or}}\right)^2 \tag{3.16}$$

where S is the vapour phase saturation, S_{cg} is the critical gas saturation and S_{or} is the residual oil saturation. If we set S_{cg} and S_{or} to be zero, the fractional flow function for vapour phase is expressed as:

$$f = \frac{S^2}{S^2 + \frac{(1-S)^2}{M}} \tag{3.17}$$

where M is the ratio between the oil phase viscosity (μ_o) and vapour phase viscosity (μ_g) :

$$M = \frac{\mu_o}{\mu_g} \tag{3.18}$$

3.2.1.2 Derivation of the governing equations

The analytical solution of Eq.3.12 requires certain assumptions as shown below:

- No volume change upon mixing (u_T is constant)
- Constant equilibrium ratio (K-value) for each component
- The phase and rock are incompressible (densities of the phases and rock are constant)
- Diffusive effects are negligible
- Gravity term is negligible
- There are a maximum of two phases
- The saturations of residual oil, connate water and critical gas are zero

The governing equation is derived from Eq.3.12 by first writing Eq.3.12 in its dimensionless form as:

$$\frac{\partial}{\partial \tau}(\sum_{j=1}^{np} y_{ij}\rho_j S_j) + \frac{\partial}{\partial \xi}[\sum_{j=1}^{np}(y_{ij}\rho_j f_i)] = 0 \tag{3.19}$$

where τ is the dimensionless time and ξ is the dimensionless distance:

$$\tau = \frac{u_T t}{\phi L} \tag{3.20}$$

$$\xi = \frac{x}{L} \tag{3.21}$$

If we denote the volume fraction of component i in phase j as c_{ij}, we have the following relation with mole fraction y_{ij}:

$$\rho_{ci} c_{ij} = \rho_j y_{ij} \tag{3.22}$$

In the above equation, ρ_{ci} is the molar density of component i. Substituting Eq.3.22 into Eq.3.19, the dimensionless conservation equation for two phase flow is given by:

$$\frac{\partial C_i}{\partial \tau} + \frac{\partial F_i}{\partial \xi} = 0; \; i = 1, ..., nc \tag{3.23}$$

where the overall volume fraction C_i and overall fractional flow function F_i for component i are defined as:

$$C_i = \sum_{j=1}^{np} c_{ij} S_j = \sum_{j=1}^{np} C_{ij} \tag{3.24}$$

and

$$F_i = \sum_{j=1}^{np} c_{ij} f_j = \sum_{j=1}^{np} f_{ij} \tag{3.25}$$

It is shown in Eq.3.2.1.2 that C_i is the summation of the volume fraction of each component (C_{ij}) in phase j. Eq.3.25 shows that F_i is the summation of the flux of component i in each phase (f_{ij}). By using volume fraction with component molar density, the constant component molar density can be removed from Eq.3.19 which further simplifies the equation. If the solution in terms of mole fraction is required, it is easy to convert it back by using phase molar densities.

3.2.2 Eigenvalue solution

Solving the system of partial derivative equations defined by Eq.3.23 involves finding the relationship between the parameters (*i.e.* how does each parameter change with respect to the others). The method of characteristic is implemented to solve the material balnce equation system introduced later in this chapter. We begin with the

features of a ternary system with constant equilibrium ratios or K-values.

3.2.2.1 Ternary system with constant K-values

A three-component system is normally represented using a ternary diagram. A single point inside the ternary diagram represents a unique combination of the three components. Normally the three components can be characterized as 'heavy', 'medium' and 'light' components.

The two phase region inside the ternary diagram is isolated by the 'binodal curve' that consists of the liquid locus and the vapour locus. Composition combinations that have the same equilibrium phase compositions will sit on a single straight line in the ternary diagram that is called a 'tie line'. A tie line is a significant structure that controls the behaviour of ternary displacement. More precisely, two key tie lines determine the solution behaviour of the three-component problem: the injection tie line, and the initial tie line. These are the tie lines upon which the injection composition and initial composition rest. A ternary diagram with constant K-values has the following properties (proof of their properties will not be discussed here):

- Tie lines do not intersect inside the ternary diagram (each tie line can be uniquely identified)
- Vapour and liquid loci are straight lines

Observing the linear behaviour of the phase envelope, the correlations for tie lines can be obtained. Each straight line in a ternary diagram can be expressed as a linear

equation and as can an arbitrary tie line. A single tie line can be expressed as:

$$C_2 = \varphi(\eta)C_1 + \theta\eta \tag{3.26}$$

In the above equation, φ is the slope of the tie line and θ is the interception with $C_1 = 0$ the boundary. The parameter that uniquely identifies a tie line is η. This could be the liquid phase composition (c_{i1}), or the vapour phase composition (c_{i2}) on the tie line ('1'and '2' represent the liquid and the vapour phase, respectively).

The equilibrium liquid phase composition (c_{11}) can be calculated using any composition (C_1, C_2) lying on the same tie line using the following equations:

$$c_{11} = \frac{-b \pm \sqrt{b^2 - 4ac}}{2a} \tag{3.27}$$

where

$$a = \frac{K_1 - K_3}{K_2 - K_3}\frac{K_1 - K_2}{K_2 - 1}$$
$$b = \frac{K_1 - K_3}{K_2 - K_3}C_1 + \frac{K_1 - 1}{K_2 - 1}C_2 - \frac{1 - K_3}{K_2 - K_3}\frac{K_1 - K_2}{K_2 - 1}$$
$$c = -\frac{1 - K_3}{K_2 - K_3}C_1$$

With constant K-values, the phase envelope in a ternary diagram is bounded by straight lines and the K-values of the intermediate component significantly affect the phase envelope behaviour. As shown in Fig.3.1, with $K_1 = 2.5$ and $K_3 = 0.05$, the four ternary phase diagrams are generated with different K-values of the intermediate component (K_2). The shape of the two phase region and direction of the tie lines change significantly depending on the value of different K_2. The direction of tie lines directly lead to different driving mechanisms and miscibility development.

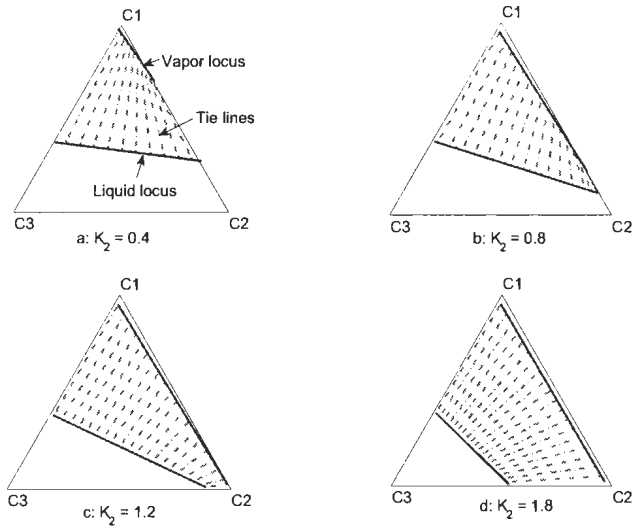

Figure 3.1: Phase envelop and tie lines behaviour with difference intermediate component K-value

If we have an initial composition in the liquid phase region and an injection composition in the vapour phase region, the composition path connecting the initial and injection compositions has to cross the two phase region with constant K-values. Miscibility in such a case is therefore meaningless.

According to the K-value of the intermediate component and the location of the initial and injection compositions, the displacement can be categorized by different driving mechanisms. In this chapter, we demonstrate the calculation using the following two types of problems:

1. Condensing gas drive with a low volatility intermediate (LVI) component ($K_2 < 1$). We denote this type of problem as 'LVI condensing '.

2. Vapourizing gas drive with a high volatility intermediate (HVI) component ($K_2 > 1$). We denote this type of problem as 'HVI vapourizing '.

3.2.2.2 Method of characteristics

It can be shown that the overall fractional flow function F_i can also be expressed in the form of Eq.3.28:

$$F_2 = \alpha(\eta)F_1 + \phi(\eta) \tag{3.28}$$

Substituting Eq.3.26 and Eq.3.28 into Eq.3.23 and using chain rule we get:

$$\left(C_1\frac{d\alpha}{d\eta} + \frac{d\phi}{d\eta}\right)\frac{\partial\eta}{\partial\tau} + \left(F_1\frac{d\alpha}{d\eta} + \frac{d\phi}{d\eta}\right)\frac{\partial\eta}{\partial\xi} = 0 \tag{3.29}$$

$$\frac{\partial C_1}{\partial\tau} + \frac{\partial F_1}{\partial C_1}\frac{\partial C_1}{\partial\xi} + \frac{\partial F_1}{\partial\eta}\frac{\partial\eta}{\partial\xi} = 0 \tag{3.30}$$

The above equations can be shown in the form of:

$$\frac{\partial u}{\partial\tau} + A(u)\frac{\partial u}{\partial\xi} = 0 \tag{3.31}$$

where

$$A(u) = \begin{pmatrix} \frac{\partial F_1}{\partial C_1} & \frac{\partial F_1}{\partial\eta} \\ 0 & \frac{F_1+\epsilon}{C_1+\epsilon} \end{pmatrix} \tag{3.32}$$

$$\epsilon = \frac{1-K_3}{K_1-K_2}\frac{K_2-1}{K_1-K_3}c_{11}^2 \tag{3.33}$$

By solving the displacement problem discribed by Eq.3.23, we determine how the compositions propagate and distribute along the displacement space with time. The value of η determines a unique tie line, and C_1 determines the unique point on the tie line, hence η and C_1 together can identify a unique point in the ternary space. For a fixed C_1 and η we have :

$$dC_1 = \frac{\partial C_1}{\partial\tau}d\tau + \frac{\partial C_1}{\partial\xi}d\xi = 0 \tag{3.34}$$

$$d\eta = \frac{\partial \eta}{\partial \tau} d\tau + \frac{\partial \eta}{\partial \xi} d\xi = 0 \tag{3.35}$$

Substituting Eq.3.34 and Eq.3.35 into Eq.3.31 leads to the following eigenvalue problem:

$$\begin{pmatrix} \frac{\partial F_1}{\partial C_1} - \Lambda & \frac{\partial F_1}{\partial \eta} \\ 0 & \frac{F_1 + \epsilon}{C_1 + \epsilon} - \Lambda \end{pmatrix} \begin{pmatrix} \frac{\partial C_1}{\partial \xi} \\ \frac{\partial \eta}{\partial \xi} \end{pmatrix} = 0 \tag{3.36}$$

where

$$\Lambda = \frac{d\xi}{d\tau} \tag{3.37}$$

The solution to Eq.3.36 gives the two eigenvalues:

$$\Lambda_t = \frac{\partial F_1}{\partial C_1}, \quad and \quad \Lambda_{nt} = \frac{F_1 + \epsilon}{C_1 + \epsilon} \tag{3.38}$$

The expression for Λ_t can be further simplified to:

$$\Lambda_t = \frac{df}{dS} \tag{3.39}$$

Substituting the two eigenvalues into Eq.3.36 leads to two corresponding eigenvectors, *e.g*:

$$\vec{e}_t = \begin{pmatrix} 1 \\ 0 \end{pmatrix}, \quad \vec{e}_{nt} = \begin{pmatrix} 1 \\ \frac{\Lambda_{nt} - \Lambda_t}{\frac{\partial F_1}{\partial \eta}} \end{pmatrix} \tag{3.40}$$

where the notation t is the tie line eigenvector and nt is the non-tie line eigenvector. The tie line eigenvector shows the change of η is zero which indicates that the propagation occurs along a fixed tie line. As the composition varies along a tie line, its propagation velocity is Λ_t. The same explanation applies for the nontie-line eigenvector: when η is changing along a nontie-line eigenvector, the compositions propagate with Λ_{nt}. The compositions propagating along a nontie-line eigenvector are called the nontie-line paths and they cross different tie lines.

3.2.3 Composition path

A ternary diagram is a composition space in which not all the compositions satisfy the conservation equations. According to the eigenvalue solution, only the compositions which vary along an eigenvector will appear in the solution. As stated previously, the composition and the tie line parameter η can determine a unique point in a ternary diagram, hence if the dependence of composition and η is known, the path along which the conservation equation is valid is also known. The relationship between the composition and η along eigenvectors can be determined by integrating the eigenvectors. The solutions to the conservation equations consist of the compositions that connect the initial and injection compositions. These compositions are called the composition path.

Integration of the eigenvectors shows that two types of composition paths exist in a ternary diagram: the tie line path and the nontie-line path. Integration of the tie line eigenvector is shown as a straight line that coincides with the tie line. By choosing the liquid phase composition (c_{11}) for η and using the fractional flow function shown as Eq.3.17, the integration of the nontie-line eigenvector with respect to the vapour saturation (S) is expressed as:

$$\begin{aligned} c_{11} = c_{11}^0 \frac{f^0 - S^0}{f - S} + \frac{1 - K_3}{K_1 - K_2}\frac{K_2 - 1}{K_1 - K_3}\left\{\frac{f^0 - S^0}{f - S} - 1\right\} \\ + \frac{\frac{1-K_3}{K_1-K_2}\frac{K_2-1}{K_1-K_3}(K_1 - 1)}{f - S}(S^0 f^0 - Sf) + \frac{2\frac{1-K_3}{K_1-K_2}\frac{K_2-1}{K_1-K_3}(K_1 - 1)}{f - S}\int_{S^0}^{S} f dS \end{aligned} \tag{3.41}$$

where

$$\int_{S^0}^{S} f dS = \frac{S - S^0}{1 + \frac{1}{M}} + \frac{\frac{1}{M}(\frac{1}{M} - 1)}{\sqrt{\frac{1}{M}}(1 + \frac{1}{M})^2} \left\{ \arctan\left(\frac{S(\frac{1}{M} + 1) - \frac{1}{M}}{\sqrt{\frac{1}{M}}} \right) - \arctan\left(\frac{S^0(\frac{1}{M} + 1) - \frac{1}{M}}{\sqrt{\frac{1}{M}}} \right) \right\} + \frac{\frac{1}{M}}{\left(\frac{1}{M} + 1\right)^2} \ln\left\{ \frac{\frac{1}{M} - \frac{2}{M}S + \left(1 + \frac{1}{M}\right) S^2}{\frac{1}{M} - \frac{2}{M}S^0 + \left(1 + \frac{1}{M}\right) (S^0)^2} \right\} \quad (3.42)$$

In the above equation, c_{11}^0 and S^0 are reference values on the nontie-line path and f^0 is the corresponding reference fractional flow function. By using Eq.3.41, the compositions along a nontie-line path can be calculated.

3.3 Elementary Wave Solution

The solution of the displacement problem consists of different elementary waves (an elementary wave is denoted as v_i) connecting the injection vapour saturation (left state of vapour saturation, denoted as S_L) and the initial vapour saturation (right state of vapour saturation, denoted as S_R). The corresponding saturations that parametrize the elementary waves are associated with either of the two eigenvalues. The elementary waves are separated by the key saturations, we denote the key saturation separating v_{i-1} and v_i as S_{i-1}.

An elementary wave can either be a rarefaction wave or a shock wave. If v_i is a rarefaction wave, the eigenvalues along v_i can be calculated using the saturations from S_{i-1} to S_i. For a shock wave, the eigenvalue of this shock can be calculated by

applying the shock mass conservation expressed as:

$$v_i = \frac{F_1(S_i) - F_1(S_{i-1})}{C_1(S_{i-1}) - C_1(S_i)};\ i = 1, ..., N \tag{3.43}$$

where N is the number of the elementary waves and v_i is calculated using the overall fractional flow function and composition of component 1.

In this chapter, two cases of the three-component problem will be evaluated. The first is a LVI condensing case with $K_2 = 0.5$. Condensing gas drive occurs when the injection tie line lies to the right of the initial tie line as shown in Fig.3.2. For the condensing gas drive case, the intermediate component condenses from the injected vapour phase condenses into liquid phase during the displacement. The second is an HVI vapourizing case with $K_2 = 1.6$. Vapourizing gas drive occurs when the injection tie line lies to the left of the initial tie line as shown in Fig.3.3. For the vapourizing case, the intermediate component vapourizes from liquid phase into vapour phase during the displacement.

The parameters utilized in the two case studies are summarized in Table.3.1. The solutions for both cases are provided and we use the LVI condensing case for sample calculations and detailed analysis.

3.3.1 Fractional flow analysis

Each of the composition points can propagate with either of the two eigenvalues. The fractional flow analysis is used to determine with which eigenvalue the compositions are propagating. Once the elementary wave is along a tie line path, it is associated with a tie line eigenvalue. If the elementary wave is on a nontie-line path, it is as-

Table 3.1: Input data for analytical model sample solution

Parameter	LVI condensing case	HVI vaporizing case
Injection composition (C_1, C_2)	$(0.7, 0.3)$	$(0.9, 0.1)$
Initial composition (C_1, C_2)	$(0.2, 0)$	$(0.2, 0.25)$
K-Values (K_1, K_2, K_3)	$(2.5, 0.5, 0.05)$	$(2.5, 1.6, 0.05)$
Viscosity ratio μ_o/μ_g	10	
Injection pressure P_{inj}	$15MPa$	
Production pressure P_{pro}	$14.9MPa$	
Displacement Length L	$1m$	
Permeability K	$0.3D$	
Porosity ϕ	0.18	
Residual oil saturation S_{or}	0	
Connate water saturation S_{wc}	0	
Critical gas saturation S_{cg}	0	

sociated with a nontie-line eigenvalue. We trace the saturation from S_L to S_R and identify the eigenvalue for each saturation value. While identifying eigenvalues, two conditions must be satisfied which can be described as:

Velocity condition: The velocity (eigenvalue) within the two phase region has to decrease monotonically for continuously varying saturation values traced from downstream points to upstream points on the composition path (Helfferich, 1981).

Entropy condition: The shock velocity (eigenvalue) must not be greater than the upstream velocity, and must not be less than the down stream velocity (Lax, 1973).

The fractional flow analysis for the LVI condensing case can be separated into the following parts:

(a) Identifying the two key tie lines

The two key tie lines are: i) the injection tie line on which the injection composition point is located, and ii) the initial tie line on which the initial composition point is located. The overall fractional flow curves along the injection and the initial tie lines

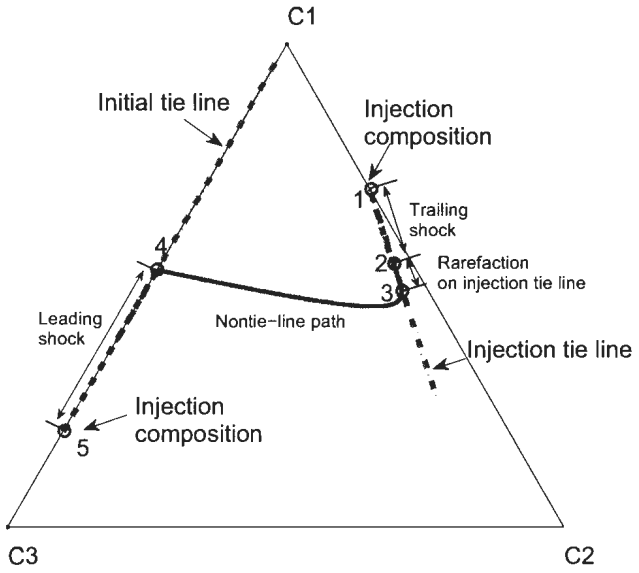

Figure 3.2: Fractional flow analysis for LVI condensing case shown in the ternary diagram

are shown in Fig.3.4. The two key tie lines are shown in Fig.3.2, the shocks and rarefactions in the corresponding ternary diagram are also shown in Fig.3.2.

(b) The trailing shock

As shown in Fig.3.4, starting from the injection composition (point 1), a shock is needed so as to not violate the velocity and entropy conditions. This shock is a jump from point 1 in the vapour phase region to point 2 in the two phase region. The propagation velocity of this shock is the slowest and it is called the tailing shock. The tie line eigenvalue at point 2 is smaller than the leading shock velocity, hence the composition at point 2 propagates with two velocities which is shown as a constant state bank.

(c) Rarefaction along the injection tie line

The eigenvalue is the slope of the tangent to the fractional flow curve on a tie line

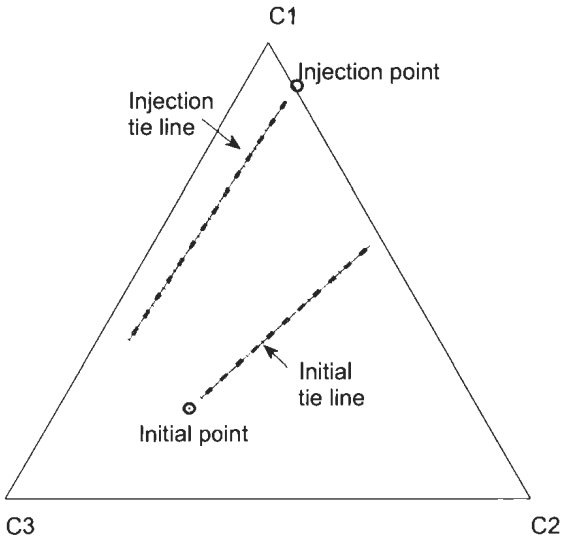

Figure 3.3: Compositions and key tie lines for HVI vapourizing case

path. As shown in Fig.3.4, the slope of the tangent to the injection fractional flow curve increases monotonically from point 2 to point 3, a rarefaction from point 2 to point 3 is therefore allowed according to the velocity condition. Point 3 is the equal eigenvalue point at which the tie line eigenvalue equals the nontie-line eigenvalue. The equal eigenvalue point is the connecting point of a tie line path and a nontie-line path. It is the point at which the composition path switches from the injection tie line to the initial tie line. The second figure in fig3.4 shows a closeup view of the dashed region of point 2, 3 and 4. The tie line eigenvalues and nonite-line eigenvalues along the injection tie line are shown in Fig.3.5 where points two and three are the same points as the points two and three in Fig.3.4. It is shown in Fig.3.5 that the tie line eigenvalue equals the nontie-line eigenvalue at point 3.

(d) A rarefaction along the nontie-line path

Point 4 in Fig.3.4 is the intersection of the nontie-line path and the initial tie line, between point 3 and point 4 are the nontie-line eigenvalues on the nontie-line path. To

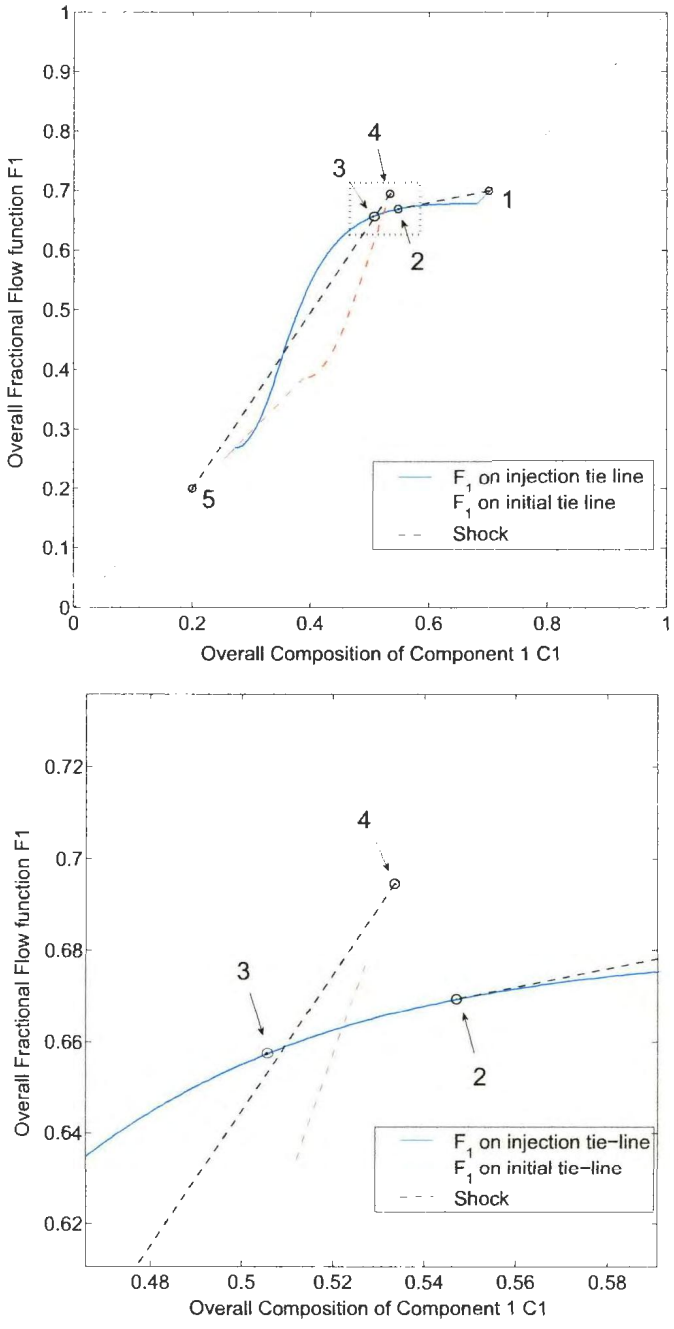

Figure 3.4: Fractional flow curve on key tie lines

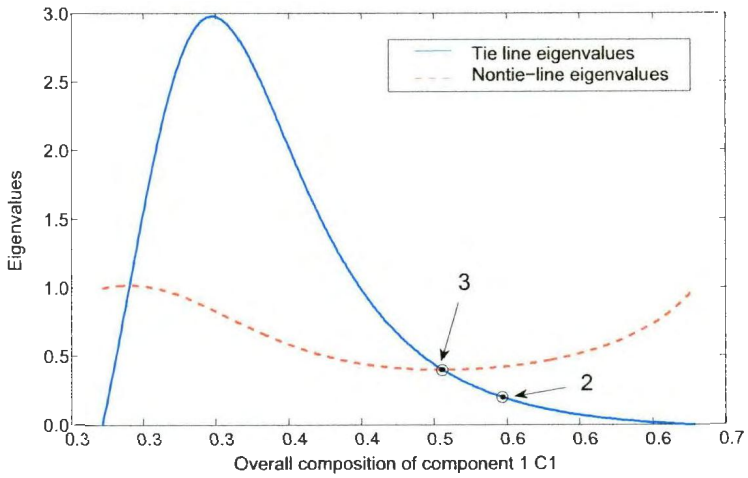

Figure 3.5: Eigenvalues on the injection tie line

show the nontie-line eigenvalues on the fractional flow curve, we look at the geometrical meaning of the nontie-line eigenvalue. The nontie-line eigenvalue, as provided in Eq.3.38, can be expressed as the slope of a line between point (C_1, F_1) and point $(-\epsilon, -\epsilon)$ on the fractional flow curve plot. By using the saturations from point 3 to point 4, c_{11} along the nontie-line path can be calculated using Eq.3.41, hence C_1, F_1 and ϵ can be calculated. Plotting the points (C_1, F_1) and $(-\epsilon, -\epsilon)$ on the fractional flow curve plot and connecting each (C_1, F_1) to the corresponding $(-\epsilon, -\epsilon)$, the nontie-line eigenvalues are shown in Fig.3.6 as the highlighted tangent envelope from point 3 to point 4. The points of $(-\epsilon, -\epsilon)$ are shown in Fig.3.7 (note: for clarity, not all points are connected). Tracing along the nontie-line path direction shown in Fig.3.6, the slope of the tangent is increasing, therefore, the rarefaction along the nontie-line path satisfies the velocity condition.

(e) The leading shock

The nontie-line eigenvalue at point 4 is smaller than the leading shock velocity, hence the composition at point 4 propagates with two velocities which is shown as a con-

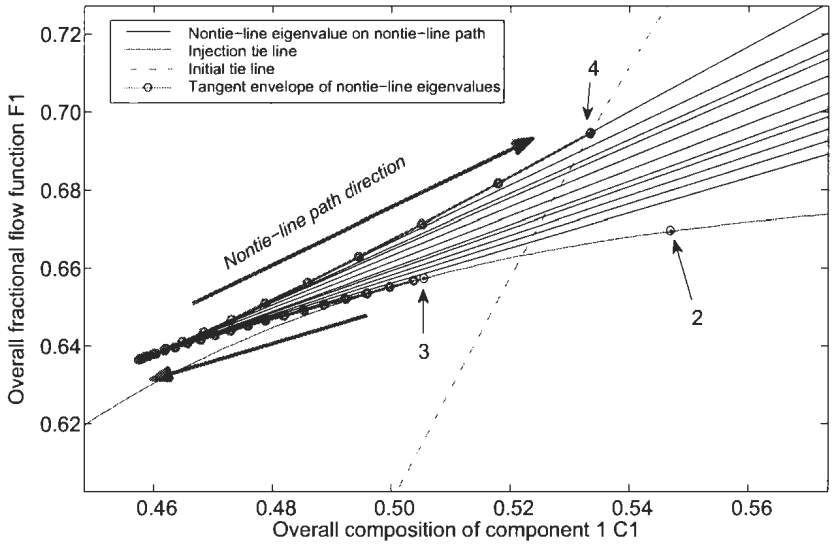

Figure 3.6: Nontie-line eigenvalues on fractional flow curve (close-up view)

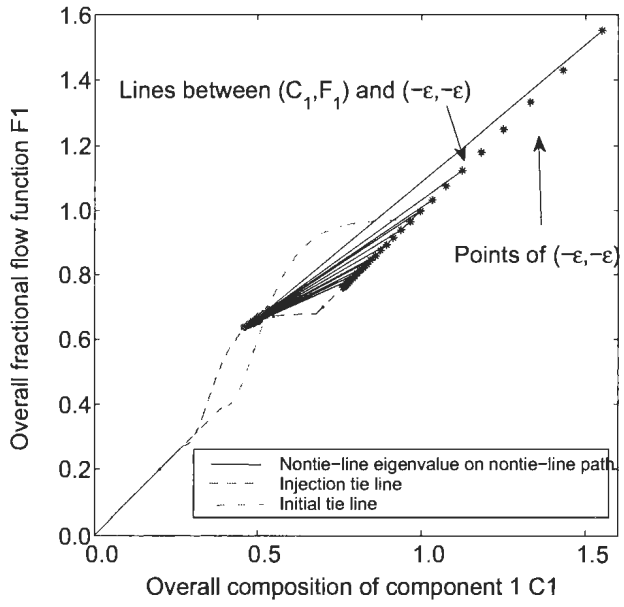

Figure 3.7: Nontie-line eigenvalues on fractional flow function (full view)

stant state bank. At point 4, the composition is located on the initial tie line. The unique solution that satisfies the velocity condition is a shock connecting point 4 and the initial composition point (point 5) as shown in Fig.3.4. The propagation velocity of this shock is the fastest and it is called the leading shock. The fractional flow analysis is completed for the LVI condensing case. From the injection composition to the initial composition, the propagation velocities (eigenvalues) are monotonically increasing.

The leading shock is is the displacement front connecting to the initial composition. As shown in Fig.3.2, the intermediate component is becoming leaner along the nontie-line path to the leading shock point (point 4), hence, the intermediate component is condensed into the liquid phase along the nontie-line path.

3.3.2 Key saturations and elementary waves

As previously stated, each tie line can be uniquely identified by the equilibrium liquid phase composition (c_{11}) associated with this tie line. The compositions which appear in the solution located on the injection and initial tie lines and across the tie lines along the non-tie line path. On the injection and initial tie line, c_{11} can be calculated using Eq.3.27, and c_{11} along nontie-line path can be calculated using Eq.3.41.

The fractional flow analysis in the previous section shows that the elementary wave solution for the LVI condensing case consists of two shock waves, two rarefaction waves and a linear wave (the constant state bank). There are five key points (point 1 to point 5) in Fig.3.4 separating the elementary waves. Each of the key saturations can be identified as following:

Point 1 (S_L): Referring to the fractional flow curve in Fig.3.4, point 1 is pure vapour phase which is the left state of saturation (S_L), by denoting the saturation at this point to be S_0, we have: $S_0 = S_L = 1$.

Point 2: At point 2, the shock velocity is equals to the tie line eigenvalue (*i.e.* the slope of the line connecting point 1 and 2 is equals to the slope of the tangent to the fractional flow curve at point 2). It can be calculated by solving the equation below, and the saturation at point 2 is denoted as S_1:

$$\frac{F_1(S_1) - F_1(S_0)}{C_1(S_1) - C_1(S_0)} = f\prime(S_1) \tag{3.44}$$

Point 3: Point 3 is the equal eigenvalue point, the saturation at point 3 is denoted as S_2 and can be obtained by solving:

$$\frac{F_1(S_2) + \epsilon}{C_1(S_2) + \epsilon} = f\prime(S_2) \tag{3.45}$$

Point 4: The nontie-line path intersects the initial tie line at point 4, c_{11} on the nontie-line path at this point is equals to c_{11} on the initial tie line. The saturation at point 4 is denoted as S_3 and can be calculated by solving the equation:

$$c_{11}(\text{nontie-line path}) = c_{11}(\text{initial tie line}) \tag{3.46}$$

where c_{11} on the nontie-line path is a function of saturation expressed by Eq.3.41.

Point 5 (S_R): Point 5 is the right state of saturation (S_R) that is the pure liquid phase. By denoting the saturation at point 5 as S_4, we have: $S_4 = S_R = 0$.

Table 3.2: Key saturations and eigenvalues for LVI condensing case

Elementary wave	**Key saturation point**	**Saturation value**	**Eigenvalue**
Trailing	$S_0(S_L)$	1	0.1994
shock (v_1)	S_1	0.6768	0.1994
Rarefaction on	S_1	0.6768	0.1994
nontie-line path (v_2)	S_2	0.5747	0.4029
Rarefaction on	S_2	0.5747	0.4029
initial tie line (v_3)	S_3	0.2505	0.8416
Linear	S_3	0.2505	0.8416
wave	S_3	0.2505	0.8416
Leading	S_3	0.2505	1.4833
shock (v_4)	$S_4(S_R)$	0	1.4833

All the key saturations that separate the elementary waves are identified. The eigenvalue of each elementary wave can be calculated using the saturation values along the wave. Based on the fractional flow analysis, the trailing shock (v_1) is associated with the tie line eigenvalue Λ_t, the rarefaction on the injection tie line (v_2) is associated with Λ_t, the rarefaction on the nontie-line path (v_3) is associated with the nontie-line eigenvalue Λ_{nt} and the leading shock (v_4) is associated with Λ_t. Between the leading edge of v_3 and v_4 is the linear wave. The key saturations and the associated eigenvalues are summarized in Table.3.2.

The elementary wave solution is shown in Fig.3.8, where saturation is plotted versus the corresponding eigenvalues. The elementary waves can be shown in terms of overall composition of each component by using c_{11}, S and K-values as shown in Fig.3.9.

The composition path presented in the ternary diagram is shown as Fig.3.10. The numbered points in Fig.3.10 correspond to the points in Fig.3.4. Fig.3.10 clearly shows the initial and injection tie lines, between which is the nontie-line path.

Following the same procedure, the key saturations and elementary waves are con-

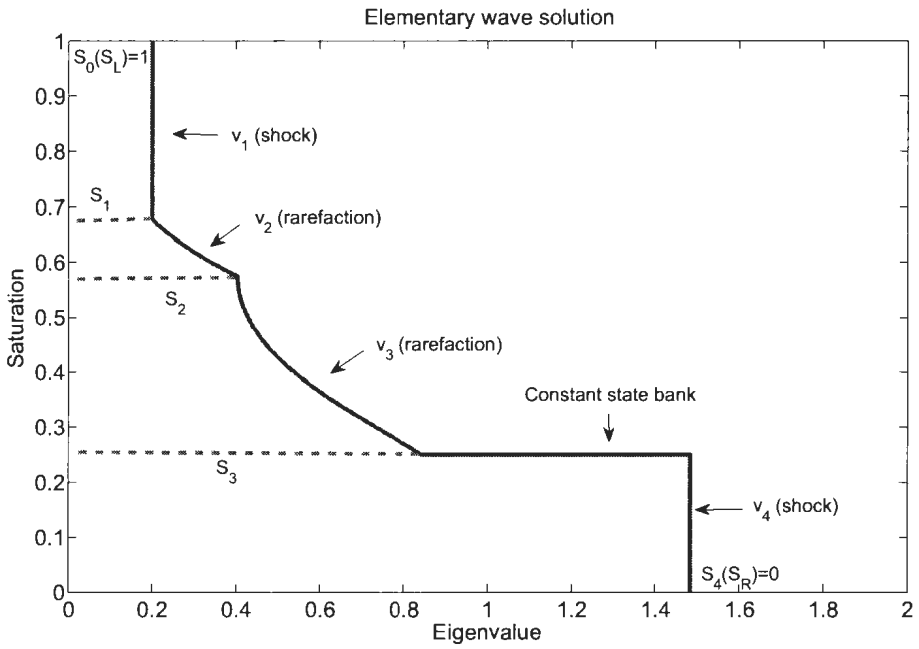

Figure 3.8: Elementary waves of saturation (LVI condensing case)

structed for the HVI vapourizing case. The key saturations and corresponding eigenvalues are summarized in Table.3.3. The solution of elementary waves and the composition path are shown from Fig.3.11 to Fig.3.13.

It should be noted that for the LVI condensing case, we use C4 to represent the intermediate component. We use CO_2 to represent the intermediate component for the HVI vapourizing case as shown in the composition elementary wave solutions.

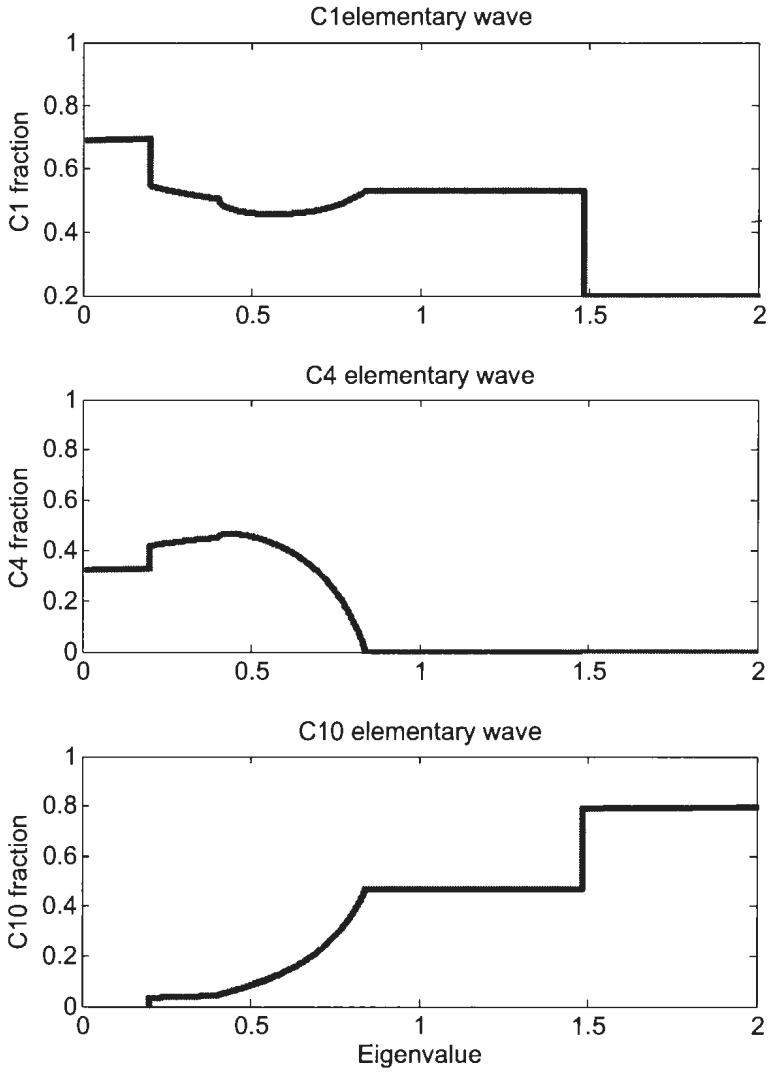

Figure 3.9: Elementary waves of component concentration (LVI condensing case)

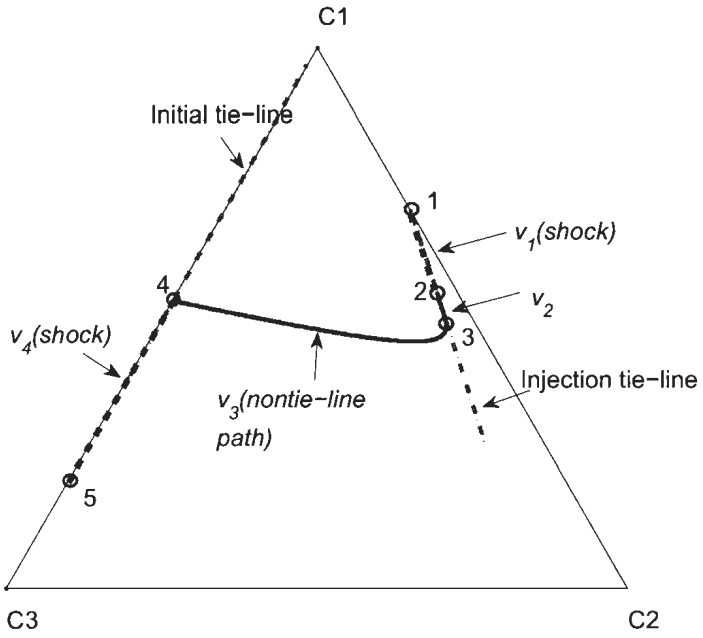

Figure 3.10: Composition path (LVI condensing case)

Table 3.3: Key saturations and eigenvalues for HVI vapourizing case

Elementary wave	**Key saturation point**	**Saturation value**	**Eigenvalue**
Trailing	$S_0(S_L)$	1	0.1994
shock (v_1)	S_1	0.6768	0.1994
Rarefaction on	S_1	0.6768	0.1994
injection tie line (v_2)	S_2	0.5585	0.4490
Linear	S_2	0.5585	0.4490
wave	S_2	0.5585	1.1801
Rarefaction on	S_2	0.5585	1.1801
nontie-line path (v_3)	S_3	0.3995	1.2537
Rarefaction on	S_3	0.3995	1.2537
initial tie line(v_4)	S_4	0.3220	1.9501
Leading	S_4	0.3220	1.9501
shock(v_5)	$S_5(S_R)$	0	1.9501

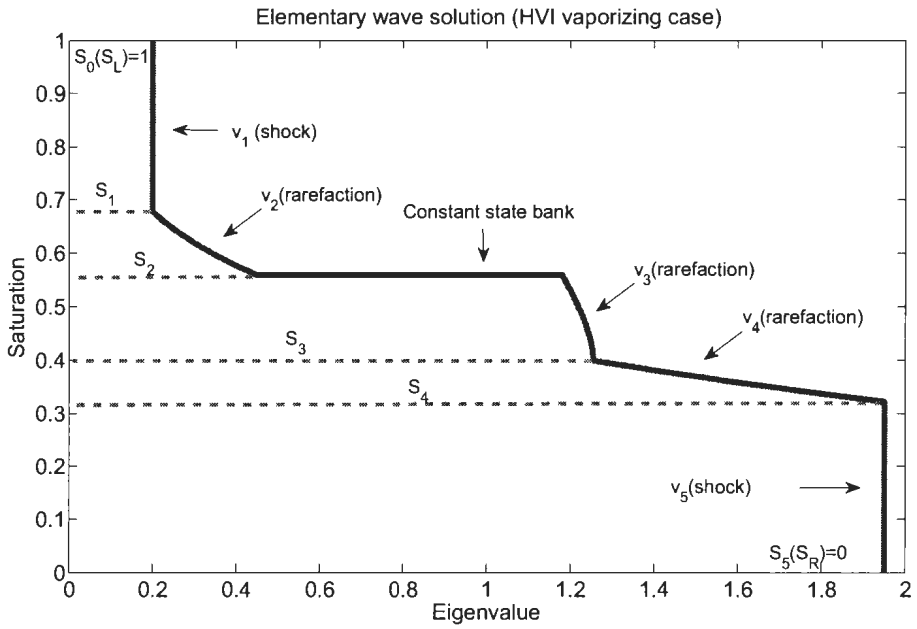

Figure 3.11: Elementary wave of saturation (HVI vaporizing case)

3.4 Total Flux Solution with Constant Pressure Boundaries

Based on the elementary wave solution calculated in the previous two sections, the time dependent u_T, pressure distribution and saturation profiles can be calculated with constant pressure boundaries by applying the approach developed by Johansen and James (2012). It should be noted that the 'propagation velocities' calculated in the previous section are not the real velocities, they are eigenvalues, the actual propagation velocity is related to u_T as:

$$V_i(t) = \frac{u_T(t)}{\phi} v_i;\ i = 1, ..., N \tag{3.47}$$

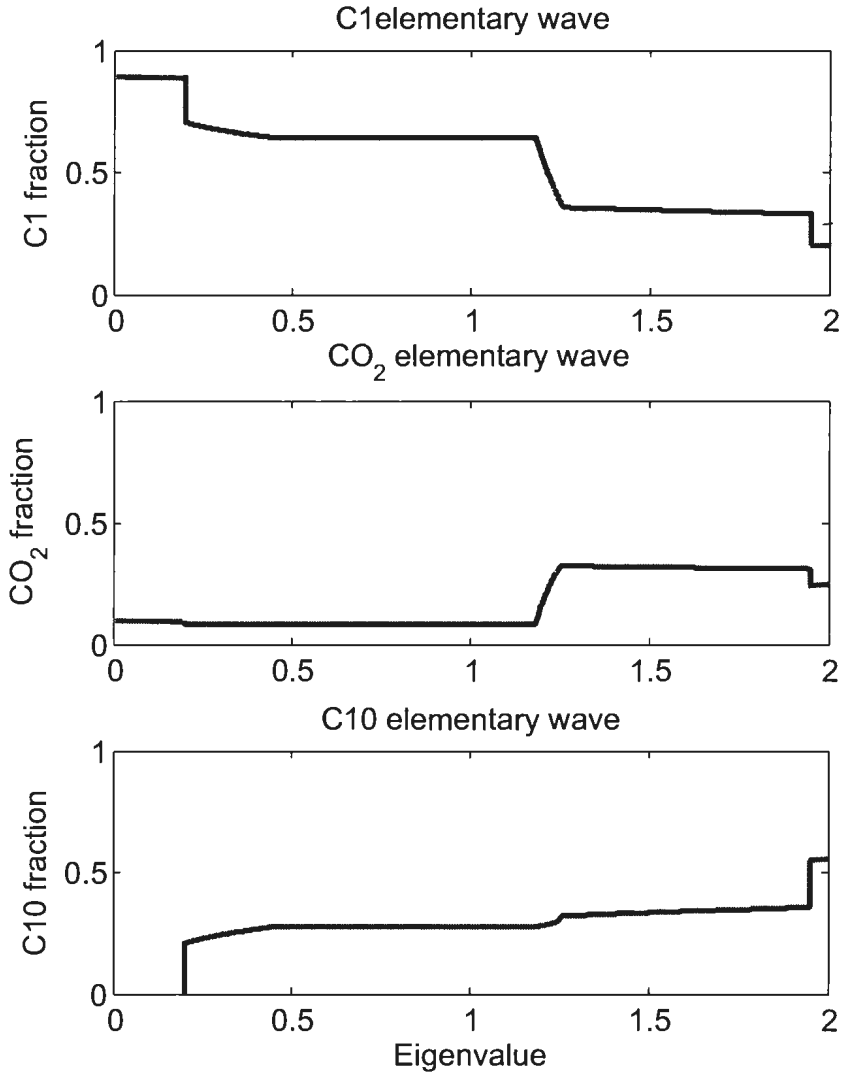

Figure 3.12: Elementary wave of component concentration (HVI vaporizing case)

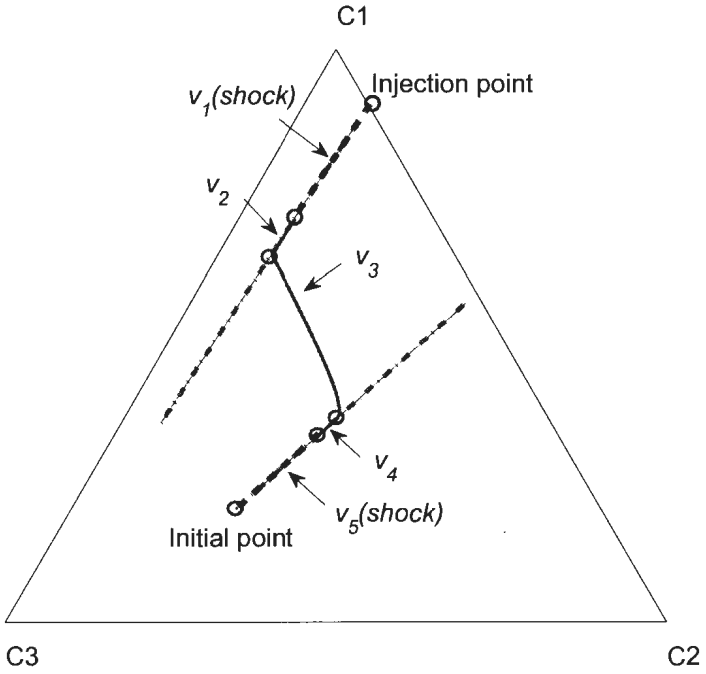

Figure 3.13: Composition path (HVI vaporizing case)

where v_i is the eigenvalue of wave i. The actual propagation velocity of v_i is denoted as V_i. As u_T is a function of time t, the actual velocity V_i is also a time dependent function.

3.4.1 The period before v_4 breaks through

Before v_4 breaks through, the saturations are all at S_4 ahead of the leading edge of v_4. Referring to the formula developed by Johansen and James (2012) the total flux can be calculated by:

$$u_T(t) = \frac{\Delta p}{\sqrt{B^2 + ACt}} \tag{3.48}$$

and breakthrough time of v_4 can be calculated by:

$$t_{BT,4} = \frac{AL^2 + 2BL}{C} \tag{3.49}$$

The data required for the calculation are provided in Table.3.1 and the parameters A, B, C are given by:

$$A = \sum_{i=1}^{N} r_i + \frac{1}{v_N(S_R)} \sum_{i=1}^{N} \mathcal{L}_i - \frac{1}{\lambda_T(S_R)} \tag{3.50}$$

$$B = \frac{1}{\lambda_T(S_R)} \tag{3.51}$$

$$C = \frac{2\triangle p v_N(S_R)}{\phi} \tag{3.52}$$

The total mobility λ_T is defined as:

$$\lambda_T = \frac{KK_{ro}}{\mu_o} + \frac{KK_{rg}}{\mu_g} \tag{3.53}$$

and the functions r_i and $\mathcal{L}_i$ are defined as:

$$r_i = \frac{v_i(S_{i-1}) - v_{i-1}(S_{i-1})}{v_N(S_R)\lambda_T(S_{i-1})} \tag{3.54}$$

$$\mathcal{L}_i = \int_{S_{i-1}}^{S_i} \frac{v_i^{'}}{\lambda_T} dS \tag{3.55}$$

It can be seen that for shocks $\mathcal{L}_i = 0$. In general, r_i represents the 'length' of a constant state bank and $\mathcal{L}_i$ represents the 'length' of each rarefaction wave. The term $\mathcal{L}_i$ can take two forms for a three component problem, either the integration of the tie line eigenvalue or the integration of the nontie-line eigenvalue. Prior to v_4 breaking

through, $N = 4$ and $S_R = S_4$. Hence we have the following expressions for r_i:

$$r_1 = \frac{f\prime(S_0) - 0}{v_4(S_R)\lambda_T(S_0)}$$

$$r_2 = \frac{f\prime(S_1) - f\prime(S_1)}{v_4(S_R)\lambda_T(S_1)}$$

$$r_3 = \frac{\frac{F_1(S_2)+\epsilon(S_2)}{C_1(S_2)+\epsilon(S_2)} - f\prime(S_2)}{v_4(S_R)\lambda_T(S_2)}$$

$$r_4 = \frac{\frac{F_1(S_3)-F_1(S_R)}{C_1(S_3)-C_1(S_R)} - \frac{F_1(S_3)+\epsilon(S_3)}{C_1(S_3)+\epsilon(S_3)}}{v_4(S_R)\lambda_T(S_3)}$$

Expressions for $\mathcal{L}_i$ are:

$$\mathcal{L}_1 = 0$$

$$\mathcal{L}_2 = \int_{S_1}^{S_2} \frac{v_2'}{\lambda_T} dS = \int_{S_1}^{S_2} \frac{\frac{2}{M}(\frac{1}{M}+1)(2S^3 - 3S^2) + \frac{2}{M^2}}{[S^2 + \frac{1}{M}(1-S)^2]^3 \lambda_T} dS$$

$$\mathcal{L}_3 = \int_{S_2}^{S_3} \frac{[\frac{F_1(S)+P(S)}{C_1(S)+P(S)}]'}{\lambda_T} dS$$

$$\mathcal{L}_4 = 0$$

where M is viscosity ratio defined in section 3.2.1.1. It can be observed from the elementary wave plot that $r_2 = 0$ and $r_3 = 0$ and that the integration of the shock waves v_1 and v_4 are zero. For time $0 < t < t_{BT,4}$, u_T can then be calculated using Eq.3.48.

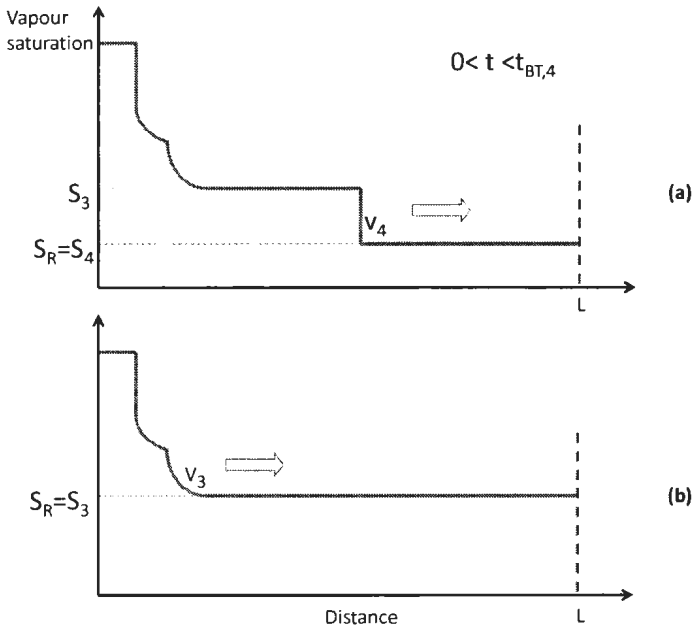

Figure 3.14: Two scenarios of wave when $0 < t < t_{BT,4}$

3.4.2 The period after v_4 breaks through, before the leading edge of v_3 breaks through

After the shock wave v_4 breaks through, v_3 becomes the leading wave ahead of which is a constant state with $S_R = S_3$. Before proceeding with the calculation, two scenarios must be compared.

In Fig.3.14 (a), is the elementary wave solution we have for the LVI condensing case having $S_R = S_4$. By removing v_4 from (a), we have the wave (b) having $S_R = S_3$. Let u_{Ta} be the total flux for (a) and u_{Tb} for (b) for $0 < t < t_{BT,4}$. We have:

$$u_{Ta}(t) = \frac{\Delta p}{\sqrt{B_a^2 + A_a C_a t}}$$

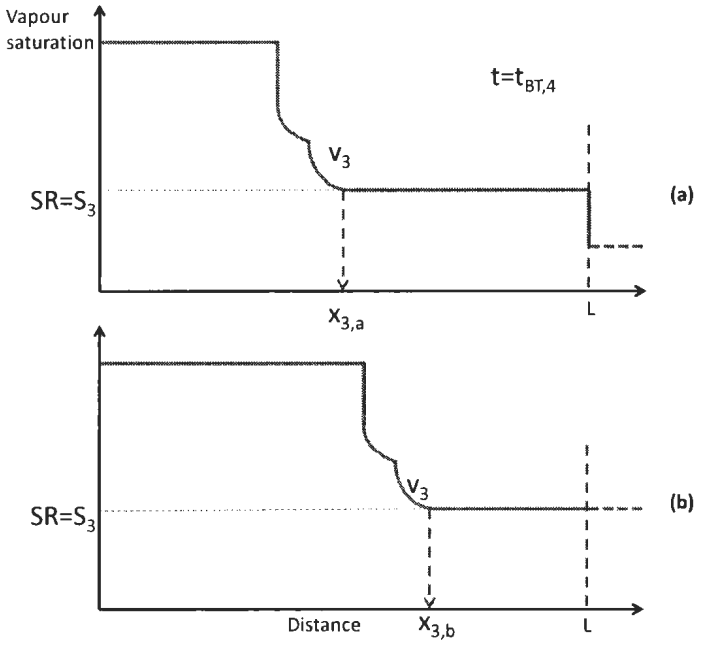

Figure 3.15: Two scenarios of wave at $t = t_{BT,4}$

$$u_{Tb}(t) = \frac{\Delta p}{\sqrt{B_b^2 + A_b C_b t}}$$

At the period $0 < t < t_{BT,4}$, (a) and (b) have different wave structures, $u_{Ta}(t)$ and $u_{Tb}(t)$ are therefore different for $0 < t < t_{BT,4}$.

As shown in Fig.3.15, $x_{3,a}$ is the location of the leading edge of v_3 for (a) and $x_{3,b}$ is the location of the leading edge of v_3 for (b). Prior to $t_{BT,4}$, (a) and (b) are travelling at different velocities, $x_{3,a}$ and $x_{3,b}$ are therefore different at each point in time.

The propagation velocity of the leading edge of a wave is expressed as:

$$\frac{dx_N}{dt} = \frac{u_T}{\phi} v_N(S_R) = \frac{\triangle p v_N(S_R)}{\phi(Ax_N + B)} \tag{3.56}$$

Integration of the above equation gives:

$$Ax_N^2 + 2Bx_N = Ct + c \tag{3.57}$$

where c is the integration constant. We first apply Eq.3.57 for case (b). When $t = 0$, $x_{3,b} = 0$, then the integration constant $c = 0$. Let $x_{3,b} = x'$ at $t = t_{BT,4}$, hence for $t_{BT,4} < t < t_{BT,3}$ we have:

$$A_b x'^2 + 2B_b x' = C_b t_{BT,4} \tag{3.58}$$

Now apply Eq.3.57 for case (a) for $t_{BT,4} < t < t_{BT,3}$. Let $x_{3,a} = x$ at $t = t_{BT,4}$. For $t_{BT,4} < t < t_{BT,3}$, (a) has the same A, B, C with (b), so we have:

$$A_b x^2 + 2B_b x = C_b t_{BT,4} + c \tag{3.59}$$

Comparing Eq.3.58 and Eq.3.59, $x' \neq x$ as discussed, so $c \neq 0$ in Eq.3.59. The difference between the two scenarios can be explained as following:

Case (b): parameters A, B, C become A_b, B_b, C_b from $t = 0$ to $t = t_{BT,3}$, hence if we trace t back to $t = 0$ with A_b, B_b, C_b, $x_{3,b}$ is zero and the integration constant c is therefore zero for $0 < t < t_{BT,3}$.

Case (a): parameters A, B, C become A_b, B_b, C_b only for the time period $t_{BT,4} < t < t_{BT,3}$, hence if we trace t back to $t = 0$ with A_b, B_b, C_b, $x_{3,a}$ will not be zero and the integration constant c is therefore not zero for $t_{BT,4} < t < t_{BT,3}$.

This also can be explained as: from $t = t_{BT,4}$, (a) and (b) are both having $A = A_b, B = B_b, C = C_b$, but they have a different total flux history before $t = t_{BT,4}$. For

(a) to use A_b, B_b, C_b for $t_{BT,3} < t < t_{BT,4}$, the difference in historical accumulation of travelled distance with (b) can be adjusted by the integration constant c. This integration constant will be needed whenever we apply Eq.3.48 for a time period after the breakthrough of the trailing edge of the leading wave.

The integration constant can be evaluated simply by substituting $x_{3,a} = x$ and $t = t_{BT,4}$ into Eq.3.59. The location of any saturation point S on v_i, at any time t, is given by:

$$x(S,t) = \frac{v_i(S)}{\phi}\Psi(t); i = 1, ..., N \tag{3.60}$$

where $\Psi(t)$ is given as:

$$\Psi(t) = \int_0^t u_T dt \tag{3.61}$$

Using Eq.3.60, $x(S_3, t_{BT,4})$ can be calculated:

$$x(S_3, t_{BT,4}) = \frac{v_3(S_3)}{\phi}\int_0^{t_{BT,4}} u_T dt$$

where u_T for $0 < t < t_{BT,4}$ is known from the previous section. Now u_T for $t_{BT,4} < t < t_{BT,3}$ and the breakthrough time of v_3 ($t_{BT,3}$) can be calculated by using Eq.3.48 with the integration constant c:

$$t_{BT,3} = \frac{AL^2 + 2BL - c}{C} \tag{3.62}$$

$$u_T(t) = \frac{\Delta p}{\sqrt{B^2 + A(Ct + c)}} \tag{3.63}$$

The parameters A, B and C need to be updated for the new wave structure with $S_R = S_3$ and $N = 3$.

3.4.3 The period when v_3 is continuously breaking through

We denote the time period $0 < t < t_{BT,4}$ as t_1, the total flux for t_1 as u_{T1}, $t_{BT,4} < t < t_{BT,3}$ as t_2, with u_{T2} as the total flux for t_2, and time period $t_{BT,2} < t < t_{BT,3}$ as t_3 and u_{T3} as the total flux for t_3. The common feature of the wave structure for t_1 and t_2 is a constant saturation continuously breaking through the outlet end. During t_3, the saturation values along v_3 are continuously breaking through. The calculation here can be expressed as:

$$u_T(t_S) = \frac{\phi[L^2 - x(S, t_{BT,N})^2]}{2Lv_N(S)(t_S - t_{BT,N})} \tag{3.64}$$

$$t_S = t_{BT,N} + \frac{\phi[L^2 - x(S, t_{BT,N})^2]}{2\Delta p v_N(S)^2} \left\{ \sum_{i=1}^{N} r_i v_N(S) + \sum_{i=1}^{N-1} \mathcal{L}_i + \int_{S_{N-1}}^{S} \frac{v_N'(S)}{\lambda_T} dS \right\} \tag{3.65}$$

where t_S is the breakthrough time of an arbitrary S on v_N and $x(S, t_{BT,N})$ is the location of S at $t_{BT,N}$. By using Eq.3.64 with Eq.3.65, t_S is calculated using the location of S at the breakthrough time of the previous value of S. In other words, the calculation here is an application of Eq.3.64 in an iterative way (*i.e.* $x(S, T_{BT,N})$ and $t_{BT,N}$ are updated while each S is breaking through).

The calculation procedure can be described as the following steps:

(1) First we break v_3 into discrete saturation values: $S(1), S(2), ..., S(n-1), S(n)$, starting from $S(1) = S_3$ to $S(n) = S_2$.

(2) The value of u_T at $t_{BT,3}$ (denoted as $u_T(t_{BT,3})$) is known.

(3) Calculate the location of $S(2)$ at $t_{BT,3}$ (denoted as $x(S(2), t_{BT,3})$) using Eq.3.61, then $t_{S(2)}$ and $u_T(t_{S(2)})$ can be calculated using Eq.3.65 and Eq.3.64, respectively.

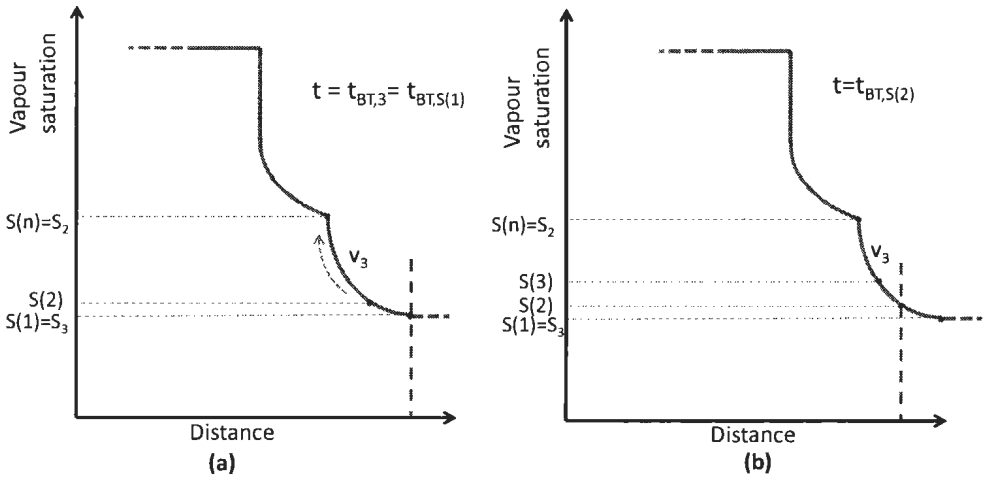

Figure 3.16: Calculation method illustration for breaking through of rarefaction wave

When calculating $x(S(2), t_{BT,3})$, $\Psi(t_{BT,3})$ needs to be calculated as:

$$x(S(2), t_{BT,3}) = \frac{v_3(S(2))}{\phi} \left(\int_0^{t_{BT,4}} u_{T1} dt + \int_{t_{BT,4}}^{t_{BT,3}} u_{T2} dt \right) \tag{3.66}$$

(4) The waves continue to advance until $S(2)$ breaks through as shown in Fig.3.16 (b). To calculate $x(S(3), t_{S(2)})$, $\Psi(t_{S(2)})$ needs to be updated as:

$$x(S(3), t_{S(2)}) = \frac{v_3(S(3))}{\phi} \left(\int_0^{t_{BT,4}} u_{T1} dt + \int_{t_{BT,4}}^{t_{BT,3}} u_{T2} dt + \int_{t_{BT,3}}^{t_{S(2)}} u_T dt \right)$$

The integration of u_T over the two points of $t_{BT,4}$ and $t_{S(2)}$ can be calculated by the numerical integration method of the trapezoidal rule:

$$\int_{t_{BT,3}}^{t_{S(2)}} u_T dt = \frac{[u_T(t_{BT,3}) + u_T(t_{S(1)})][t_{S(2)} - t_{BT,3}]}{2}$$

After calculating $x(S(3), t_{S(2)})$ using Eq.3.60, $t_{S(3)}$ can be obtained using Eq.3.65:

$$t_{S(3)} = t_{S(2)} + \frac{\phi[L^2 - x(S, t_{S(2)})^2]}{2\Delta p v_3(S(3))^2} \left\{ \sum_{i=1}^{3} r_i v_3(S(3)) + \sum_{i=1}^{2} \mathcal{L}_i + \int_{S_2}^{S(3)} \frac{v_3'(S)}{\lambda_T} dS \right\}$$

and $u_T(t_{S(3)})$ is calculated as:

$$u_T(t_{S(3)}) = \frac{\phi[L^2 - x(S(3), t_{S(2)})^2]}{2L v_3(S(3))(t_{S(3)} - t_{S(2)})}$$

(5) The same procedure can be performed for the following saturations until $S(n)$. After the calculation for $S(n)$, we have $t_{S(n)} = t_{BT,2}$, $\Psi(t_{S(n)})$ is still need to be updated:

$$\Psi(t_{S(n)}) = \int_0^{t_{S(n)}} u_T dt = \int_0^{t_{BT,2}} u_T dt$$

3.4.4 The period when v_2 is continuously breaking through

After the trailing edge of v_3 breaks through, v_2 will continuously break through and the calculation procedure will be the same as the calculation for v_3, but now we have $N = 2$. During the calculation of u_{T3} , the nontie-line eigenvalue is a rather complicated function of S, so integration of v_3' can also be performed numerically. For wave v_2, the tie line eigenvalue is relatively simple to calculate. After breakthrough of the trailing edge of v_2, u_T will remain constant, since there is only a single vapour phase flowing.

3.4.5 Sample solution

Based on the procedure outlined in the previous sections, the time dependent global flux and the locations of all waves can be generated for each time period. Fig.3.17 shows the total flux solution for the LVI condensing case.

As shown in Fig.3.17, due to the different features of each elementary wave, u_T has a different behaviour at each time period. It can be seen from the saturation profile that the less viscous vapour phase is increasing in the displacement space, while the more viscous liquid phase is being displaced. Generally, the whole fluid system within the displacement space is flowing more easily. As observed in Fig.3.17, u_T is increasing with time, but with a changing rate at different time periods.

As u_T is known at each point in time, the location of all saturation values at each corresponding point in time can be calculated using Eq.3.60. The wave locations at the time before v_4 breaks through, $t = 0.5t_{BT,4}$, $t = t_{BT,3}$ and $t = t_{BT,2}$ are calculated and shown in Fig.3.18. The advancement of the saturation wave is now able to be observed, as is the breakthrough of each elementary wave.

By using the same analysis approach, the key saturations and elementary wave for the HVI vapourizing case can be obtained. The key saturations are summarized in Table.3.3 and the elementary waves and the composition path are shown in Fig.3.11 and Fig.3.13. The time dependent u_T for the HVI vaporizing drive case is shown in Fig.3.19 and the location at different points in time is shown in Fig.3.20. The calculated u_T at the breakthrough time of each elementary wave for both cases are summarized in Table.3.4.

3.5 Pressure Gradient Calculation

From the expression of u_T:

$$u_T = -\lambda_T \frac{\partial p}{\partial x} \tag{3.67}$$

Table 3.4: Total flux solution summary

	LVI condensing	**HVI vapourizing**
$t_{BT,4}$ (s)	3212	2148.9
u_T $(10^{-4}$ $m/s)$	0.51	0.7559
$t_{BT,3}$	47286	2725.7
u_T	0.7588	1.036
* $t_{BT,c}$	-	2803.3
u_T	-	1.1699
$t_{BT,2}$	67143	4655.6
u_T	1.6982	1.5892
$t_{BT,1}$	8750.5	4655.6
u_T	2.9977	2.9981

* $t_{BT,c}$ is the breakthrough time of the leading edge of the constant state bank for HVI vapourizing case

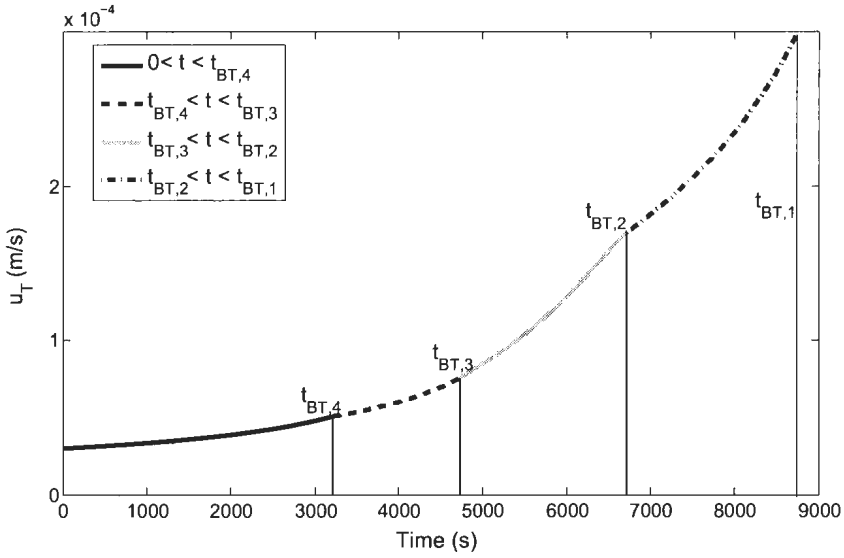

Figure 3.17: Time dependent u_T solution for LVI condensing drive case

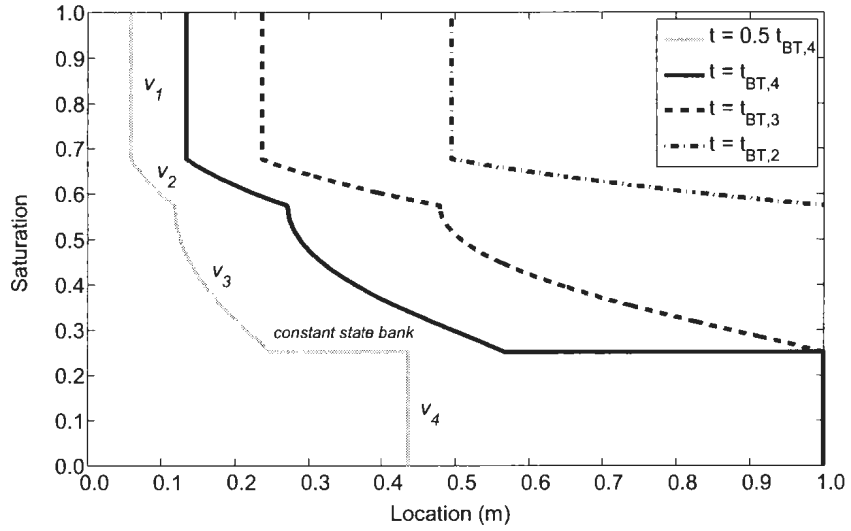

Figure 3.18: Locations at different times for LVI condensing drive case

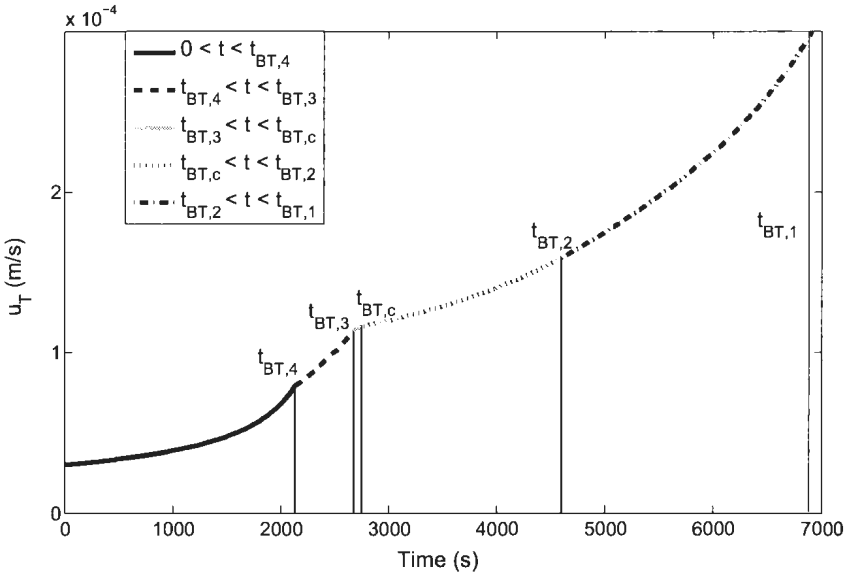

Figure 3.19: Time dependent u_T solution for HVI vaporizing drive case

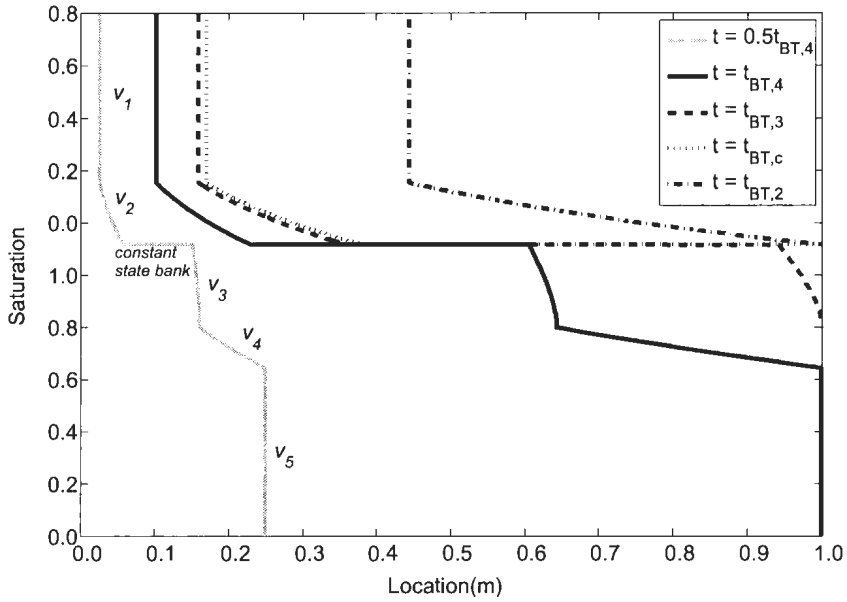

Figure 3.20: Locations at different times for HVI vaporizing drive case

The integration of the above equation will give the relationship of u_T and the pressure difference:

$$p_1 - p_2 = u_T \int_{x_1}^{x_2} \frac{dx}{\lambda_T} \tag{3.68}$$

If we let p_1 to be the known pressure at the inlet, then the pressure at any location at a given point in time can be calculated using Eq.3.68. The calculation can be generally classified into two types: i) location on the elementary waves and ii) location on the constant state banks. The approach of the pressure gradient calculation is shown by a sample solution calculation at $\hat{t} = 0.5t_{BT,4}$ for LVI condensing case.

First we show the calculation of a location on an elementary wave. As shown in Fig.3.21, we have an arbitrary point S on v_3. The location of this point is x_S and we need to calculate the pressure at this location p_{xs}. The wave between p_{inj} and p_{xs} consists of three constant states, two complete waves, and a segment of v_3 from S_2 to

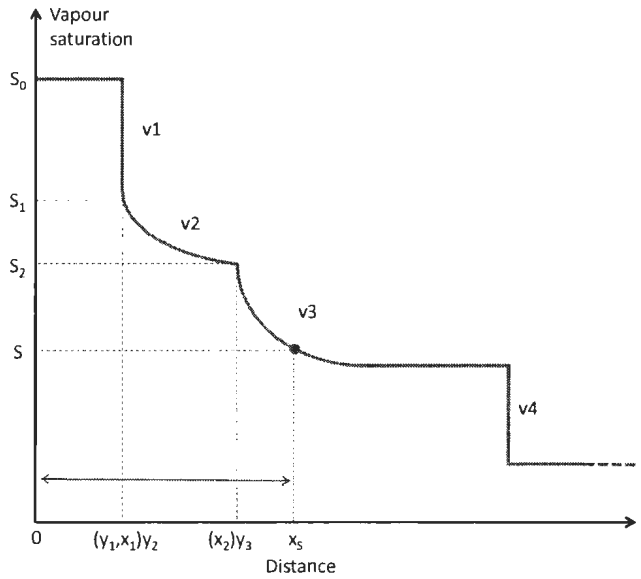

Figure 3.21: Pressure calculation for locations on rarefaction waves

S. If we denote the leading edge of v_i to be x_i and the trailing edge as y_i, referring to Fig.3.21 and applying Eq.3.68, p_{xs} can be expressed as:

$$p_{xs} = p_{inj} - u_T(\hat{t}) \left[\int_0^{y_1} \frac{dx}{\lambda_T} + \int_{y_1}^{x_1} \frac{dx}{\lambda_T} + \int_{x_1}^{y_2} \frac{dx}{\lambda_T} + \int_{y_2}^{x_2} \frac{dx}{\lambda_T} + \int_{x_2}^{y_3} \frac{dx}{\lambda_T} + \int_{y_3}^{x_S} \frac{dx}{\lambda_T} \right] \tag{3.69}$$

For shock waves we have $x_i = y_i$, and for waves that are connected with a zero length constant bank we have $y_i = x_{i-1}$. Hence the expression above can be simplified and rearranged to:

$$p_{xs} = p_{inj} - u_T(\hat{t}) \left[\sum_{i=1}^{3} \frac{y_i - x_{(i-1)}}{\lambda_T(S_{i-1})} + \frac{x(S,\hat{t})}{v_3(S)} (\sum_{i=1}^{2} \mathcal{L}_i + \int_{S_3}^{S} \frac{v_3'(S)}{\lambda_T} dS) \right] \tag{3.70}$$

Applying the definition of r_i in Eq.3.54, we have:

$$p_{xs} = p_{inj} - u_T(\hat{t}) x(S,\hat{t}) \left[\sum_{i=1}^{3} r_i + \frac{1}{v_3(S)} (\sum_{i=1}^{2} \mathcal{L}_i + \int_{S_3}^{S} \frac{v_3'(S)}{\lambda_T} dS) \right] \tag{3.71}$$

Table 3.5: Pressure calculation summary for LVI condensing case

Point	**Location** (m)	**Pressure** (kPa)
Inlet point	0	15000
Trailing shock (v_1)	0.06	14999.3
Leading edge of v_2	0.12	14997.4
Leading edge of v_3	0.25	14988.1
Leading shock (v_4)	0.44	14968.7
Outlet point	1	14900

Note that for calculating $v_N(S_R)$ in r_i, N and S_R should correspond to the point we are calculating, hence for S we should use $v_3(S)$. All other similar points on the remaining waves can be calculated using Eq.3.71. For locations on a constant bank as shown in Fig.3.22, it can be derived through the same procedure, and it is given as:

$$p_{xc} = p_{inj} - u_T(\hat{t}) \left[\sum_{i=1}^{3} r_i x(v_3, \hat{t}) + \frac{x(v_3, \hat{t})}{v_3(S)} \sum_{i=1}^{3} \mathcal{L}_i + \frac{x_c - x(v_3, \hat{t})}{\lambda_T} \right] \tag{3.72}$$

where $x(v_3, \hat{t})$ is the location of the leading edge of v_3 and for the calculation of r_i, $v_N = v_3$ and $S_R = S_3$. For the location on a constant state bank between the leading wave and the outlet end such as x_c' in Fig.3.22, it is simple to calculate using the pressure difference between x_c' and the outlet pressure, which is given as:

$$p_{xc}' = p_{out} + \frac{u_T}{\lambda_T(S_R)}(L - x_c') \tag{3.73}$$

For x_c', $v_N = v_4$ and $S_R = S_4$. By calculating the pressure at each location from the inlet to the outlet, the pressure gradient at $\hat{t} = 0.5t_{BT,4}$ can be constructed, as shown in Fig,3.23. The pressures and corresponding locations at several key points are summarized in Table.3.5.

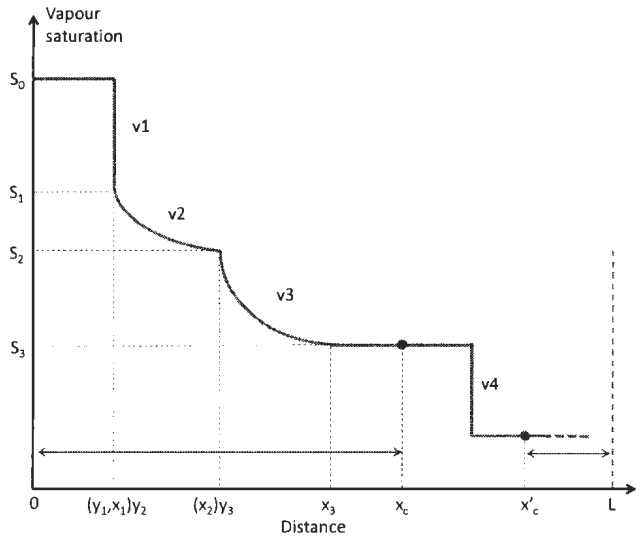

Figure 3.22: Pressure calculation for locations on constant state banks

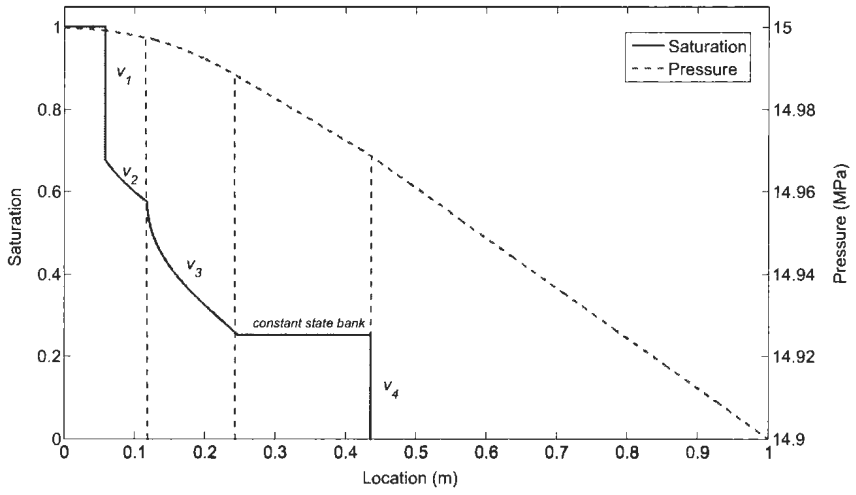

Figure 3.23: Pressure gradient at $t = 0.5t_{BT,4}$ for LVI condensing drive case

Chapter 4

Numerical Model with Constant Pressure Boundaires

4.1 Governing Equations

The goal of the numerical compositional simulations is to simulate the displacement process that most closely capture reality. In order to capture the behaviour of the reservoir fluid and porous media, we incorporate the correlations and a flash calculation procedure into the math model. The viscosities, capillary pressure, porosity and rock compressibility are modelled by the correlations. The phase molar densities are calculated by the flash procedure. The basic conservation laws express that the net mass flow of the fluid into the control volume is equal to the change of the mass of the fluid. The compositional model is based on the mass conservation for each component within the fluid system. We define the overall mole composition of each component as:

$$(\rho_o S_o + \rho_g S_g) z_i = y_{oi} \rho_o S_o + y_{gi} \rho_g S_g; \; i = 1, ..., nc \tag{4.1}$$

where y_{oi} and y_{gi} are the equilibrium liquid and vapour phase mole compositions. The liquid and vapour phase saturations are S_g and S_o, and ρ_g and ρ_o are the molar densities. The total number of components in the fluid system is defined as nc. We also have:

$$L = \frac{\rho_o S_o}{\rho_o S_o + \rho_g S_g}, V = 1 - L \tag{4.2}$$

where L and V are the liquid phase and vapour phase mole fractions, respectively. Once again we use the material balance equation from Eq.3.12 for each component in one-dimensional flow:

$$\frac{\partial}{\partial t}[\phi(\rho_g S_g + \rho_o S_o) z_i] = \frac{\partial}{\partial x}(y_{oi}\lambda_o \frac{\partial p_o}{\partial x}) + \frac{\partial}{\partial x}(y_{gi}\lambda_g \frac{\partial p_g}{\partial x});\ i = 1, ..., nc \tag{4.3}$$

$$p_g = p_o + p_{cgo} \tag{4.4}$$

where λ_j is defined as Eq.3.10 and z_i is the overall mole concentration of component i. The pressure of the oil phase (p_o) and the gas phase (p_g) are related by the capillary pressure between the two phases (p_{cgo}).

The remaining equations needed to solve the system come from the phase equilibrium constraint. Throughout the displacement process we assume that at each location we are at the thermodynamic equilibrium condition. For such an equilibrium system we have:

$$\hat{f}_{ig} = \hat{f}_{io}; i = 1, ..., nc \tag{4.5}$$

where $\hat{f}_{ig}$, $\hat{f}_{io}$ are fugacities of each component for the gas and oil phase. The constraints of equal fugacity on each component in all phases are calculated using the flash calculation performed using the pressure and overall composition at each location. The system consists of the equations and constraints above and the unknowns

of phase saturation. Once the saturations for next time step are solved, the phase mole fraction, pressure, overall composition and equilibrium phase compositions for next time step can then be solved.

4.2 Fluid and Rock Parameters

The correlation used in the model is introduced in this section. It should be noted that all symbols utilized refer to the original literature.

4.2.1 Relative permeability

The widely-used capillary pressure model developed by Brooks and Corey (1964) as shown in Eq.3.15 and Eq.3.16 is applied in the numerical model to obtain values for relative permeabilities.

4.2.2 Capillary pressure

The Brooks-Corey model is used for modelling the capillary pressure (P_c). It gives:

$$P_c = p_e(S_w^*)^{-\frac{1}{\lambda}} \tag{4.6}$$

$$S_w^* = \frac{S_w - S_{wr}}{1 - S_{wr}} \tag{4.7}$$

where S_{wr} is the residual saturation of the wetting phase and p_e is the entry capillary pressure. The entry capillary pressure (p_e) is the initial value of the capillary pressure and the atmosphere pressure of 14.69 psi is used for pe. The rock pore size distribution index (λ) reflects the rock property effect on capillary pressure. We assume $\lambda = 0.56$ to approximate the pore size distribution index of a average reservoir sandstone.

4.2.3 Gas viscosity

Chung (1984, 1988) proposed the method for pure gas viscosity prediction as:

$$\mu = 40.785 \frac{F_c (MT)^{1/2}}{V_c^{2/3} \Omega_v} \tag{4.8}$$

$$F_c = 1 - 0.2756\omega + 0.059035 u_r^4 + k \tag{4.9}$$

$$\Omega_v = [A(T^\star)^{-B}] + C[exp(-DT^\star)] + E[exp(-FT^\star)] \tag{4.10}$$

where μ is the viscosity of a pure gas component (cp), M is the molecular weight (g/mol), T is temperature ($^\circ K$), V_c is the critical volume (cm^3/mol), $T^* = 1.22593 T_r$, T_r is the reduced temperature. In the expression for F_c, ω is the acentric factor and k is a special correction for highly polar substances, in this case k is zero. The constants in Ω_v are $A = 1.16145, B = 0.14874, C = 0.52487, D = 0.77320, E = 2.1617$ and $F = 2.43787$.

After the viscosity of each of the pure components have been calculated, the method by Wilke (1950) is used to calculate the gas mixture viscosity. Wilke (1950) proposed:

$$\mu_m = \sum_{i=1}^{n} \frac{y_j \mu_i}{\sum_{j=1}^{n} y_j \phi_{ij}} \tag{4.11}$$

$$\phi_{ij} = \frac{[1 + (\mu_i/\mu_j)^{(1/2)} (M_j/M_i)^{(1/4)}]^2}{[8(1 + M_i/M_j)]^{(1/2)}} \tag{4.12}$$

where y_i is the mole fraction of each component and n is total number of components in the vapour phase.

4.2.4 Oil viscosity

A real oil sample contains a large number of hydrocarbon components and non-hydrocarbon components. The model proposed by Elsharkawy (2003) is:

$$\mu_o = a_1 T^{a_2} P^{a_3} (\gamma_{c7+})^{a_4} (G_L)^{a_5} (G_m)^{a_6} (G_h)^{a_7} \tag{4.13}$$

where $a_1 = 2248.089447, a_2 = -1.27846, a_3 = 0.117425, a_4 = 13.191727$, $a_5 = -0.32428, a_6 = 0.066623, a_7 = 0.655418$, and γ_{c7+} is specific gravity for $C7+$ components. The mole fraction of the light component group, the intermediate component group and the heavier component group are G_L, G_m and G_h, respectively. The temperature (T) is in $^\circ F$ and pressure (P) is in psi. Apply this model to the three-component system, the mole fraction of the three components corresponds to G_L, G_m and G_h respectively.

4.2.5 Porosity

A porosity model derived from rock compressibility is used:

$$\phi = \phi_0[1 + cp(P - P_0)] \tag{4.14}$$

where ϕ is porosity, cp is rock compressibility in Pa^{-1}, P_0 is the reference pressure in Pa and ϕ_0 is porosity at the reference pressure P_0.

4.2.6 Equation of state

A general flash calculation procedure is used with the Peng-Robinson equation of state (PR EOS). The detailed flash procedure and the PR EOS will be provided in Appendix.A.

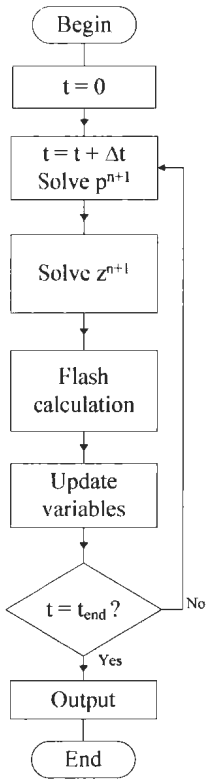

Figure 4.1: Model calculation procedure

4.3 Model Structure

The commonly used IMPES method is used for solving the governing equations. The calculation procedure flow is illustrated in Fig.4.1. The calculation begins when $t = 0$ and continue until t equals the specified termination time (t_{end}). After specifying all input parameters, the model will perform the calculation and update all variables. The associated data can be generally classified into sections including: rock property data, fluid property data, condition (*i.e.* pressure and temperature) data and grid block data, etc. The data structure for the model that illustrates the relationship between the data groups is shown in Fig.4.2.

It is illustrated in Fig.4.2 that the main variables include the overall composition and gas phase pressure. By using the flash calculation and correlations, the variables including the molar densities, saturations, phase compositions, viscosities and porosity are obtained. The grid block data controls the performance and configurations of the simulation process.

4.3.1 Method of solving pressure

4.3.1.1 Pressure equation

The gas phase pressure is used as the primary variable, hence the following 'pressure' refers to the gas phase pressure (*i.e.* p is p_g). Using Eq.4.3 for each component we have:

$$\sum_{i=1}^{nc} z_i = 1, \sum_{i=1}^{nc} y_{oi} = 1, \sum_{i=1}^{nc} y_{gi} = 1; \; i = 1, ..., nc \tag{4.15}$$

After summation of Eq. 4.3 we obtain:

$$\frac{\partial}{\partial t}[\phi(\rho_g S_g + \rho_o S_o)] = \frac{\partial}{\partial x}(\lambda_o \frac{\partial p_o}{\partial x}) + \frac{\partial}{\partial x}(\lambda_g \frac{\partial p_g}{\partial x}) \tag{4.16}$$

Substituting p_o by p, using Eq. 4.4, and defining α as:

$$\alpha = \rho_o S_o + \rho_g S_g \tag{4.17}$$

we get the pressure equation:

$$\frac{\partial}{\partial t}[\phi\alpha] = \frac{\partial}{\partial x}[\lambda_o \frac{\partial(p_g - p_{cgo})}{\partial x}] + \frac{\partial}{\partial x}(\lambda_g \frac{\partial p_g}{\partial x}) \tag{4.18}$$

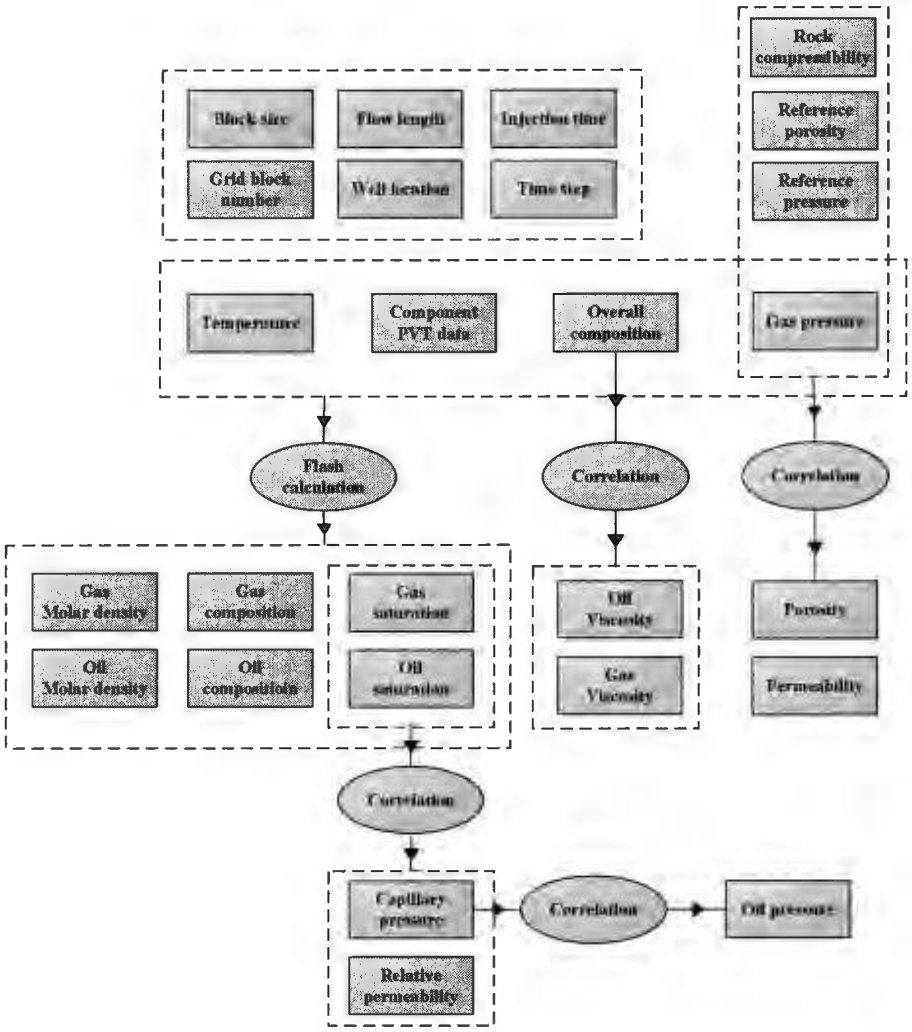

Figure 4.2: Model data structure

4.3.1.2 Discretization of pressure equation

Starting from the left hand side of Eq.4.18:

$$\frac{\partial}{\partial t}[\phi\alpha] = \alpha\frac{\partial\phi}{\partial p}\frac{\partial p}{\partial t} + \phi\frac{\partial\alpha}{\partial p}\frac{\partial p}{\partial t} \tag{4.19}$$

From Eq. 4.14 it can be shown that:

$$\frac{\partial\phi}{\partial p} = \phi_0 c_p \tag{4.20}$$

$$\frac{\partial\alpha}{\partial p} = (S_o\frac{\partial\rho_o}{\partial p} + S_g\frac{\partial\rho_g}{\partial p}) \tag{4.21}$$

The time discretization is:

$$\frac{\partial p}{\partial t} = \frac{p^{n+1} - p^n}{\Delta t} \tag{4.22}$$

where n stands for time step. The molar density of the gas and the oil phase can be expressed as:

$$\rho_j = \frac{p}{Z_j RT};\ j = o, g \tag{4.23}$$

hence, the molar density derivative term in Eq. 4.21 can be expressed as:

$$\frac{\partial\rho_j}{\partial p} = \frac{1}{Z_j RT}(1 - \frac{p}{Z_j}\frac{dZ_j}{dp}) \tag{4.24}$$

Firoozabadi et al. (1988) provided a detailed method for calculation of the compressibility derivative term in the above equation. This is shown in Appendix.A. The centre point finite difference method is used to discretize the partial derivatives. This method uses the parameters in the block centre to represent the whole block. An one-dimensional flow is used to show the modelling scheme as is shown in Fig.4.3. A two-dimensional scenario will be shown in a later section. In Fig.4.3, the potential

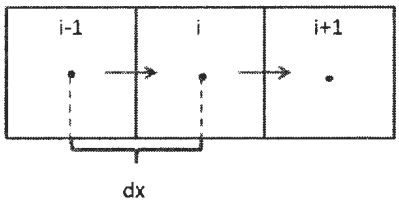

Figure 4.3: 1D blocks scheme

flow direction is set from left to right, where dx is the distance between each block node. For block i, the right hand side of Eq.4.18 can be written as:

$$\begin{aligned}&(\lambda_{oi+\frac{1}{2}}\frac{p_{i+1}^{n+1}-p_{cgo}(S_{i+1}^{n})-p_{i}^{n+1}+p_{cgo}^{n}(S_{i}^{n})}{\Delta x}\\&-\lambda_{oi-\frac{1}{2}}\frac{p_{i}^{n+1}-p_{cgo}(S_{i}^{n})-p_{i-1}^{n+1}+p_{cgo}(S_{i-1}^{n})}{\Delta x})\frac{1}{\Delta x}\\&+(\lambda_{gi+\frac{1}{2}}\frac{p_{i+1}^{n+1}-p_{i}^{n+1}}{\Delta x}-\lambda_{gi-\frac{1}{2}}\frac{p_{i}^{n+1}-p_{i-1}^{n+1}}{\Delta x})\frac{1}{\Delta x}\end{aligned}\tag{4.25}$$

where $\lambda_{i-\frac{1}{2}}$ is the mobility of either phase across the interface between block $i-1$ and i and $\lambda_{i-\frac{1}{2}}$ is the mobility across block i and $i+1$. The mobility is calculated using the upstream approximation in Eq.3.10:

$$\lambda_{i-\frac{1}{2}}=\frac{Kk_r(S_{i-1}^{n})}{\upsilon_{i-1}}\rho_{i-1},\ \lambda_{i+\frac{1}{2}}=\frac{Kk_r(S_{i}^{n})}{\upsilon_{i}}\rho_{i}$$

We first assume a homogeneous medium, therefore we have a single permeability K. When dealing with the heterogeneous cases, the permeability will be up scaled for the interface between blocks.This will be further discussed in the two-dimensional case modelling section.

Substituting Eq.4.19 to Eq.4.25 into Eq.4.18, we have the pressure equation in the

following form of:

$$
\begin{aligned}
&(\alpha\frac{\partial\phi}{\partial p}+\phi\frac{\partial\alpha}{\partial p})^n\frac{p_i^{n+1}-p_i^n}{\Delta t}= \\
&(\lambda_{oi+\frac{1}{2}}\frac{p_{i+1}^{n+1}-p_{cgo}(S_{i+1}^n)-p_i^{n+1}+p_{cgo}^n(S_i^n)}{\Delta x} \\
&-\lambda_{oi-\frac{1}{2}}\frac{p_i^{n+1}-p_{cgo}(S_i^n)-p_{i-1}^{n+1}+p_{cgo}(S_{i-1}^n)}{\Delta x})\frac{1}{\Delta x} \\
&+(\lambda_{gi+\frac{1}{2}}\frac{p_{i+1}^{n+1}-p_i^{n+1}}{\Delta x}-\lambda_{gi-\frac{1}{2}}\frac{p_i^{n+1}-p_{i-1}^{n+1}}{\Delta x})\frac{1}{\Delta x};\ i=1,...,N
\end{aligned}
\tag{4.26}
$$

It should be noted that Eq.4.26 only contains one unknown, p^{n+1} . If we have a total of N grid blocks, we will have a system of N equations to solve. By rearranging Eq.4.26, we obtain the pressure equation in the form of:

$$
a_i p_{i-1}^{n+1}+b_i p_i^{n+1}+c_i p_{i+1}^{n+1}=F_i;\ i=1,...,N \tag{4.27}
$$

where

$$
\begin{aligned}
a_i &= (\lambda_{oi-\frac{1}{2}}+\lambda_{gi-\frac{1}{2}})/\Delta x^2 \\
b_i &= -(\lambda_{oi-\frac{1}{2}}+\lambda_{gi-\frac{1}{2}}+\lambda_{oi-\frac{1}{2}}+\lambda_{gi-\frac{1}{2}}+\varepsilon_i)/\Delta x^2 \\
c_i &= (\lambda_{oi+\frac{1}{2}}+\lambda_{gi+\frac{1}{2}})/\Delta x^2 \\
F_i &= -\lambda_{oi-\frac{1}{2}}p_{cgo}(S_{i-1}^n)+(\lambda_{oi+\frac{1}{2}}+\lambda_{oi-\frac{1}{2}})p_{cgo}(S_i^n)-\lambda_{oi+\frac{1}{2}}p_{cgo}(S_{i+1}^n)+\epsilon_i p_i^n \\
\varepsilon_i &= (\alpha\frac{\partial\phi}{\partial p}+\phi\frac{\partial\alpha}{\partial p})^n/\Delta t
\end{aligned}
$$

Eq.4.27 represents a linear system of pressure equations. This can be directly solved by assembling a tridiagonal matrix. The unknown vector is defined as $(p_1, p_2, ...p_{N-1}, p_N)$.

The pressure equation coefficient matrix is shown as:

$$\begin{pmatrix} b_1 & c_1 & & & \\ a_2 & b_2 & c_2 & & \\ & \ddots & \ddots & \ddots & \\ & & a_{N-1} & b_{N-1} & c_{N-1} \\ & & & a_N & b_N \end{pmatrix} \begin{pmatrix} p_1 \\ p_2 \\ \vdots \\ p_{N-1} \\ p_N \end{pmatrix} = \begin{pmatrix} F_1 - a_1 p_0 \\ F_2 \\ \vdots \\ F_{N-1} \\ F_N - c_N p_{N+1} \end{pmatrix} \tag{4.28}$$

In this case, the fixed boundary pressure condition is used. In the equation above, p_0 represents the constant injection pressure and p_{N+1} represents the production pressure, specified as boundary conditions. By solving Eq.4.28, the pressure at each node can be updated simultaneously for the next time step.

4.3.2 Method of solving for composition

From the original pressure equation Eq.4.18, it also can be shown that:

$$(\phi\alpha)^{n+1} = (\phi\alpha)^n + \Delta t[\frac{\partial}{\partial x}(\lambda_o \frac{\partial(p - p_{cgo})}{\partial x}) + \frac{\partial}{\partial x}(\lambda_g \frac{\partial p}{\partial x})] \tag{4.29}$$

where the term $(\phi\alpha)^{n+1}$ can be calculated by using the newly solved pressure in Eq.4.29. The conservation equation for each component is used to calculate the overall composition of each component. Eq.4.3 can be written as:

$$\frac{(\phi\alpha)^{n+1} z_i^{n+1} - (\phi\alpha)^n z_i^n}{\Delta t} = \frac{\partial}{\partial x}(y_{oi}\lambda_o \frac{\partial(p - p_{cgo})}{\partial x}) + \frac{\partial}{\partial x}(y_{gi}\lambda_g \frac{\partial p}{\partial x});\ i = 1, ..., nc$$

For simplicity, the right hand side of the composition equation is expressed in partial differential form, where i in the equation stands for component index. This equation is repeated for each grid block. Rearranging the equation above, we get the following

composition equation:

$$z_i^{n+1} = \frac{(\phi\alpha)^n z_i^n + \Delta t[\frac{\partial}{\partial x}(y_{oi}\lambda_o\frac{\partial(p-p_{cgo})}{\partial x}) + \frac{\partial}{\partial x}(y_{gi}\lambda_g\frac{\partial p}{\partial x})]}{(\phi\alpha)^{n+1}} \tag{4.30}$$

The overall composition of each component can be calculated using Eq.4.30. The upstream values of phase composition y_o and y_g inside partial depreciative terms are used and the term $(\phi\alpha)^{n+1}$ is as calculated by Eq.4.29.

We use a single point upstream method to calculate the flux across the block interface that y_o(or y_g) at block $i-1$ is used to calculated the flux at the location of $i-1/2$.

4.3.3 Solving for saturation, phase composition and density

The pressure and overall compositions calculated from the previous two sections are the input values at the next time step. By using the updated pressure and overall compositions, the saturation, composition and phase molar densities at the next time step are calculated from the flash calculation.

The flash calculation is based on the constraints of isothermal phase equilibrium as expressed by Eq.4.5. During the iteration process, the equilibrium constant K-values are obtained which satisfy Eq.4.5. The vapour and liquid mole fractions and phase compositions are also obtained. From Eq.4.2, the phase saturation can be calculated. Phase molar densities are obtained from the EOS calculation. Note that if a single phase (either S_g or S_o =1) is predicted, the value of the overall composition (z_i) is used for y_g or y_o in the calculation.

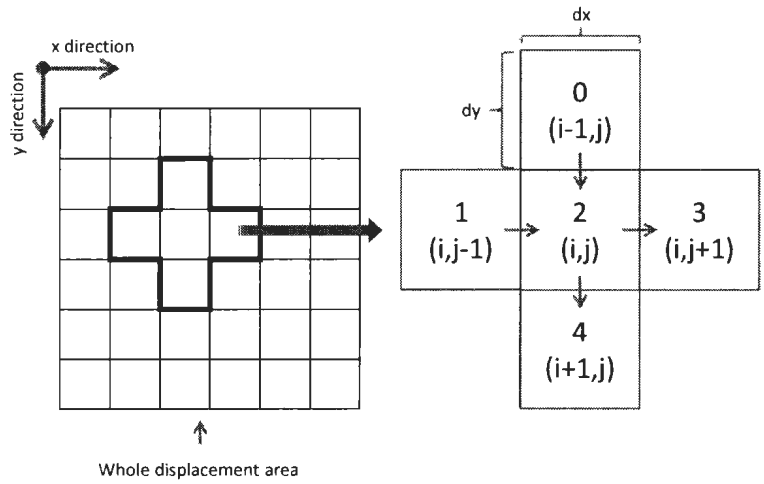

Figure 4.4: 2D grid block scheme

4.4 Upgrading to a Two-dimensional Model

4.4.1 Grid block arrangement

The displacement for a two-dimensional model can be decomposed into two directions (x and y directions) assuming the flow is in a horizontal plane and gravity is negligible. A typical grid block configuration used in this thesis is shown in Fig.4.4. For a single block, for example block 2, the flow will be related to the four adjacent blocks: block $0, 1, 3, 4$. It should be noted that block 2 is an arbitrary non-boundary block.

Assuming a flow direction as indicated by the arrows in Fig.4.4 and applying the IMPES formulation in both directions, we have:

$$u_{o,0-2} - u_{o,2-4} + u_{g,0-2} - u_{g,2-4} = u_{o,1-2} - u_{o,2-3} + u_{g,1-2} - u_{g,2-3} = 0 \qquad (4.31)$$

where u is defined as:

$$\lambda \frac{\partial p}{\partial x} \; or \; \lambda \frac{\partial p}{\partial y} \qquad (4.32)$$

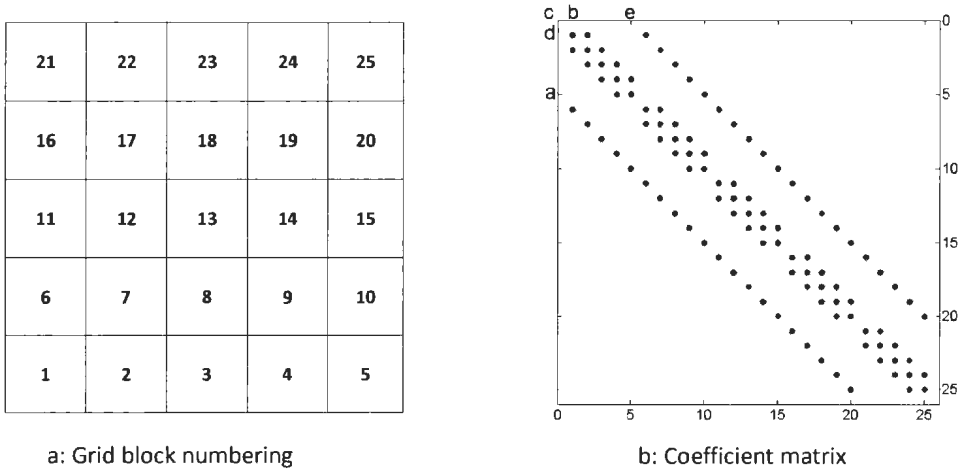

Figure 4.5: Grid block numbering and coefficient matrix

and λ is as defined in Eqs.3.10. From Eqs.4.31 we have:

$$u_{0-2} - u_{2-4} + u_{1-2} - u_{2-3} = 0 \tag{4.33}$$

By substituting λ into Eq.4.33, the pressure equation can be obtained. Rearranging Eq.4.33, we have the pressure equation in the form of :

$$a_k p^{n+1}_{(i-1,j)} + b_k p^{n+1}_{(i,j-1)} + c_k p^{n+1}_{(i,j)} + d_k p^{n+1}_{(i,j+1)} + e_k p^{n+1}_{(i+1,j)} = F_k;\ k = 1, ..., N \tag{4.34}$$

Once again, N is the total number of grid blocks. The pressure equation for the 2D case will define a different linear system. Using the example of, a 5×5 grid configuration as shown in Fig.4.5 (a), the constant coefficient matrix will be a 25×25 matrix as shown in Fig.4.5 (b). This example shows the exponential increase in required calculations with any refinement of the grid block configuration. The extension to a 2D model requires far greater computing resources as compared to the 1D case. After assembling the linear system, pressure can calculated. The calculation scheme for updating the composition and other properties is similar to the 1D model.

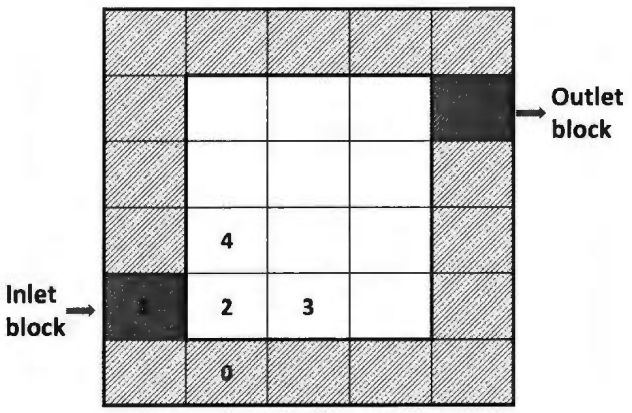

Figure 4.6: Boundary adjacent block treatment

4.4.2 Boundary treatment

Since a no flow boundary is applied, the boundary blocks will have the same pressure as the adjacent inner blocks. A five-spot configuration is shown in Fig.4.6, where shadowed blocks are used as boundaries, inner blocks are the numbered flowing grid blocks and the red blocks are the inlet and outlet block, respectively. As boundaries, p_1 is fixed at the injection pressure (p_{inj}) and p_0 is equal to p_2. The pressure equation of block 2 can thus be write as:

$$(a_2 + c_2)p_2^{n+1} + d_2p_3^{n+1} + e_2p_4^{n+1} = F_2 - b_2p_{inj} \tag{4.35}$$

Eq.4.35 shows that for block 2 in Fig.4.6, the coefficient in front of p_2^{n+1} in the matrix is actually $a_2 + c_2$ and a_2 is eliminated from the matrix shown in Fig.4.5. The same manipulation can be applied to all inner blocks adjacent to the boundary blocks. Using the no flow boundary condition, all inner block pressures are solved as unknowns.

4.4.3 Permeability upscaling

In a heterogeneous displacement field, variation in permeability and other rock properties will affect the fluid flow directions and pressure distribution. The permeability needs to be upscaled for approximating the flow across the adjacent block interface. A harmonic average scheme is used for permeability upscaling. For two adjacent blocks, 1 and 2, the upscaled permeability can be calculated by:

$$K_{1-2} = \frac{2dx}{\frac{dx}{K_1} + \frac{dx}{K_2}} \tag{4.36}$$

4.4.4 Sample solution of 2D model

A sample water flooding case was simulated to verify the 2D model formulation. The geological model SPE-10[1] was used as an example which is specified as a $60 \times 220 \times 85$ grid block dimension shown in Fig.4.7. The first layer of the SPE-10 model is used for the simulation. We take the logarithm of the permeabilities in the plot so that the high values and the low values of permeability both can be identified clearly shown in Fig.4.7(b). The permeabilities ranged from 0.003 mD to 4647 mD. The red circle region in Fig.4.7(a) and the corresponding region in Fig.4.7(b) is a low permeability region.

The water flooding process is simulated on a $60 \times 220 \times 0.1(m)$ grid block configuration. The sample solution for water saturation distribution is shown in Fig.4.8. The water is injected from the left bottom block [block$(1, 1)$] and produced at the right top block [block$(220, 60)$]. The figure illustratess that the water flows around the low permeability region toward the outlet (shown as the blue dished eclipse region in Fig.4.8).

[1]SPE 10th Comparative Solution Project Model 2

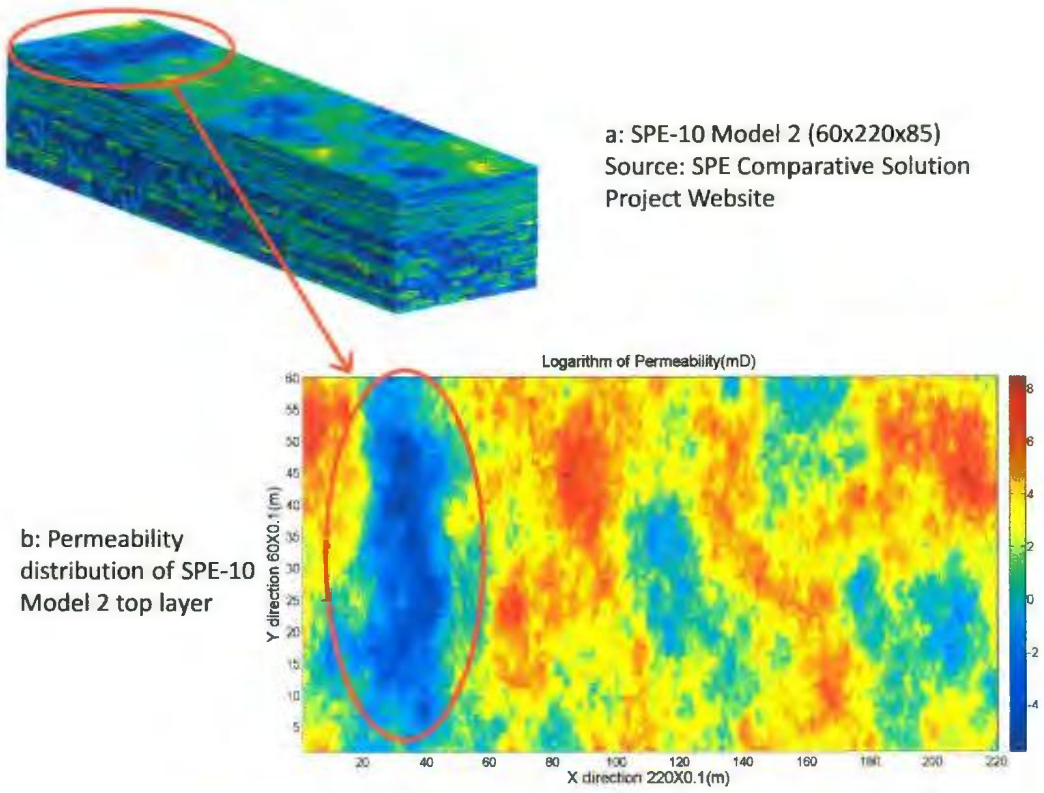

Figure 4.7: SPE-10 grid model and permeability distribution

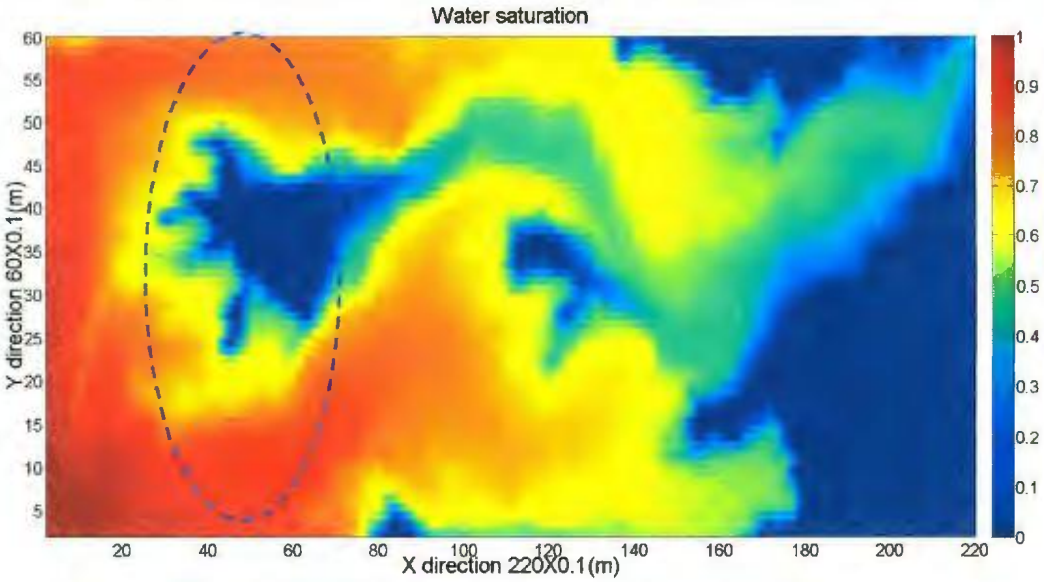

Figure 4.8: Water saturation distribution on SPE-10 model 2 top layer

Chapter 5

Numerical Model Validation and Case Study

The solution from the numerical model can be validated by comparing it to the analytical solution. As discussed in the previous chapter, when we increase the number of properties (for example viscosity, capillary pressure) that are modelled in the numerical simulation, these properties and the numerical method will smear the solutions, such they make shocks and each elementary wave are becoming identical. To verify the solution from numerical model, a comparison with the analytical solution is required. From the comparison, features of the displacement are expected to be revealed.

5.1 Numerical Model Validation

The numerical model can be validated by comparing the solution to the analytical solution. The analytical solution of the LVI condensing case from Chapter 3 is used for the comparison. We simplify the numerical model such that constant K-values are used and the property correlations are ignored. For both the analytical solution and

Table 5.1: Input data for comparison

Parameter	Numerical model	Analytical model
Injection composition	$C_1 = 0.7, C_2 = 0.3$	
Initial composition	$C_1 = 0.2, C_2 = 0$	
Constant K-values	$K_1 = 2.5, K_2 = 0.5, K_3 = 0.05$	
Residual oil saturaition	$S_{or} = 0$	
Connate water saturation	$S_{wc} = 0$	
Critical gas saturation	$S_{cg} = 0$	
Grid block number	50, 300, 1000	—
Length	$1m$	—
Time step/grid size	$\frac{\Delta t}{\Delta x} = 0.1$	—

the numerical solution, we use a constant total flux condition. The input data for the comparison is shown in Table.5.1.

The comparison of the saturation profile is shown in Fig.5.1. The numerical solution using 50 grid blocks shows that the leading shock is smeared. It is shown that the leading shock from the analytical solution has a velocity of 1.48 and the leading edge of the numerical solution using 50 grid blocks has a velocity of 1.64. As the grid block number is increased to 300, a relatively sharp leading shock can be identified, however, v_2 and v_3 (the wave notation refers to the elementary wave solution for LVI condensing case in Fig.3.8 in Chapter 3) can not be identified. When we use 1000 grid blocks, the solution shows quite a sharp leading shock and each of the elementary waves can be identified. By refining the grid blocks from 50 to 1000, it shows that the numerical solution approaches the analytical solution. The comparison of the components profile also interprets the same behaviour as shown in Fig.5.2.

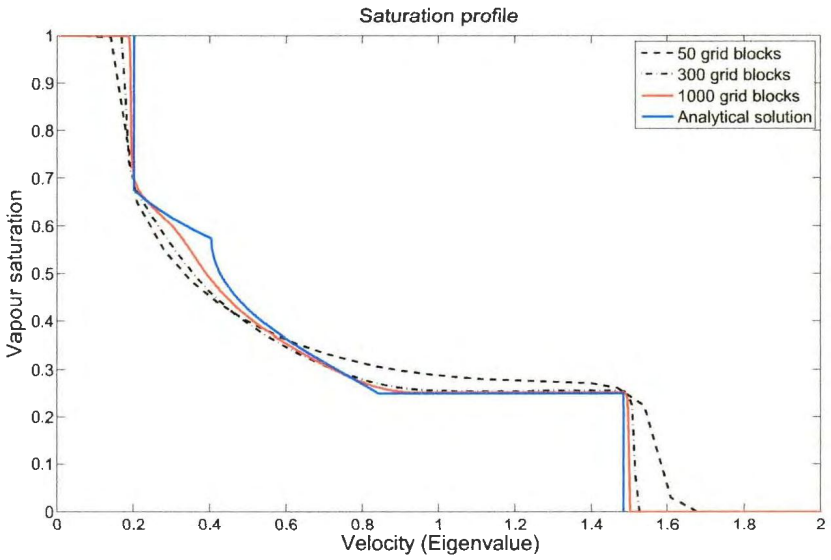

Figure 5.1: Saturation profile comparison

5.2 Case Study

5.2.1 Case study 1: 1-D ternary system injection

5.2.1.1 Preview

The most significant mechanisms for the gas injection process are component behaviour and transfer among phases. The performance of the composition based simulation system is also directly related to the properties of the components. This study uses two sets of ternary systems, C1, CO_2, C10 and C1, C4, C10 to demonstrate how different components affect the displacement performance. Carbon dioxide (CO_2) plays a critical role for flue gas injection processes. By choosing CO_2 and comparing this with normal gas injection, the advantages of flue gas injection can be presented. All parameters are kept the same for both cases, the only variation is to the critical properties of CO_2 and C4. Values for all the parameters are listed in Table.5.2.

Since the capillary pressure will smear the solution, we ignore the capillary pressure.

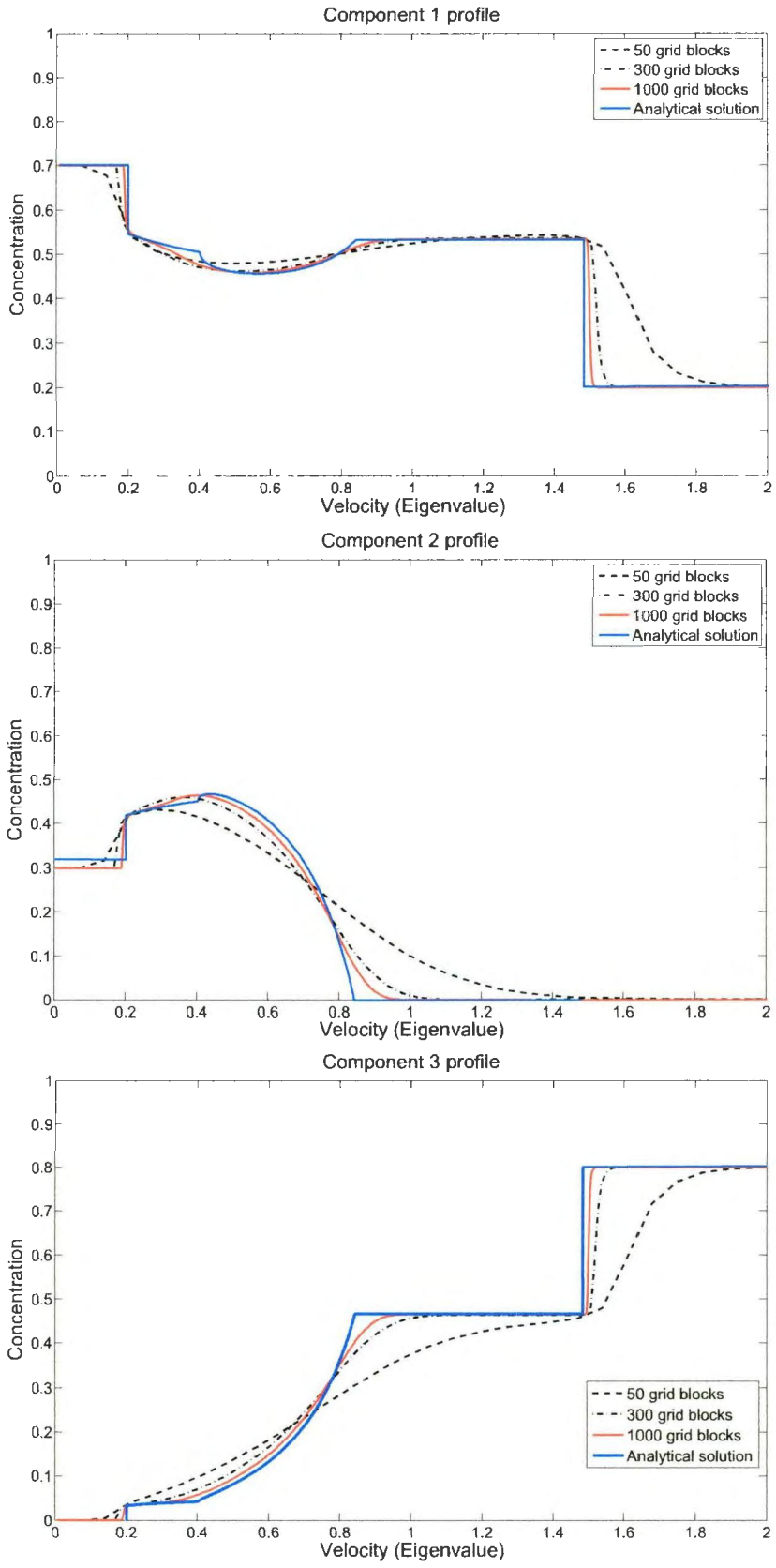

Figure 5.2: Elementary wave profile comparison

All properties' correlations are incorporated with the exception of capillary pressure. The accuracy of the results depends on the applicability of the correlations, the numerical method stability and the limitation of assumptions. In this case study, a ternary composition of C1, CO_2(C4) and C10 are used with the purpose of representing 'light', 'medium' and 'heavy' groups of components. As some of the correlations are developed based on real oil samples containing higher number of components, the correlations are not entirely suitable for a simple three-component system. However, these correlations will capture the trend and major effect of a particular property. This will be discussed below.

The viscosity correlation of Eq.4.13 is expressed in terms of the mole fraction of 'light', 'medium' and 'heavy' groups and the specific gravity of the C7+ group, hence in this case study, each of the three components are used to represent the three groups. A normal rock compressibility, $cp = 9.1 \times 10^{-9} \quad (Pa^{-1})$, and reference porosity of 0.18 is used. For the purpose of simplicity, residual oil saturation, connate water saturation and critical gas saturation are set at zero for both case studies.

In each case study, a fixed pressure boundary condition is applied. The fixed injection and production pressures are in accordance with real injection processes and are kept above the bubble point. Keeping the pressures above the liquid phase bubble point will insure there is only a single liquid phase present.

5.2.1.2 Results and conclusion

The saturation solutions and the concentration profile of each component, for both cases, are shown in Fig.5.3. From the comparison of saturation, it can be observed that CO_2 has a relatively higher vapour phase saturation within the displaced space

Table 5.2: Case 1 input data

Injection composition	$C1 = 0.7$, CO_2(C4)= 0.2
Initial composition	$C1 = 0.25$, CO_2(C4)= 0.05
Injection pressure	$P_{inj} = 15MPa$
Production pressure	$P_{pro} = 14MPa$
Temperature	$T = 400K$
Permeability	$K = 0.3D$
Reference Porosity	$\phi_0 = 0.18$
Rock compressibility	$cp = 9.1 \times 10^{-9}(pa^{-1})$
Pore index	0.54
Residual oil saturaition	$S_{or} = 0$
Connate water saturation	$S_{wc} = 0$
Critical gas saturation	$S_{cg} = 0$

and it has a slightly higher recovery than the C4 system. The composition path in the ternary diagram is shown in Fig.5.4. It can be shown that different components lead to different tie line directions and distributions. Using the same pressure boundaries and temperature, a different two-phase region and tie line directions will give two different displacement types, and hence different miscibility development trends.

5.2.2 Case study 2: 2-D ternary system injection

5.2.2.1 Preview

In one-dimensional flow a uniform permeability was used and all fluids advanced in a single direction. In a real situation, reservoirs are heterogeneous. The heterogeneous porous media will lead to variations in the fluid flow path. The high permeable areas will generally make fluid move relatively fast while low permeable areas will slow down the fluid or even restrain the flowing fluid. This difference in permeability and also variations in viscosity will produce a fingering flow pattern. Due to fingering flow, components will be distributed irregularly which will cause the composition at some locations to be miscible. The variation of the porous media permeabilities, therefore, has a significant effect on reservoir fluid miscibility development. The model devel-

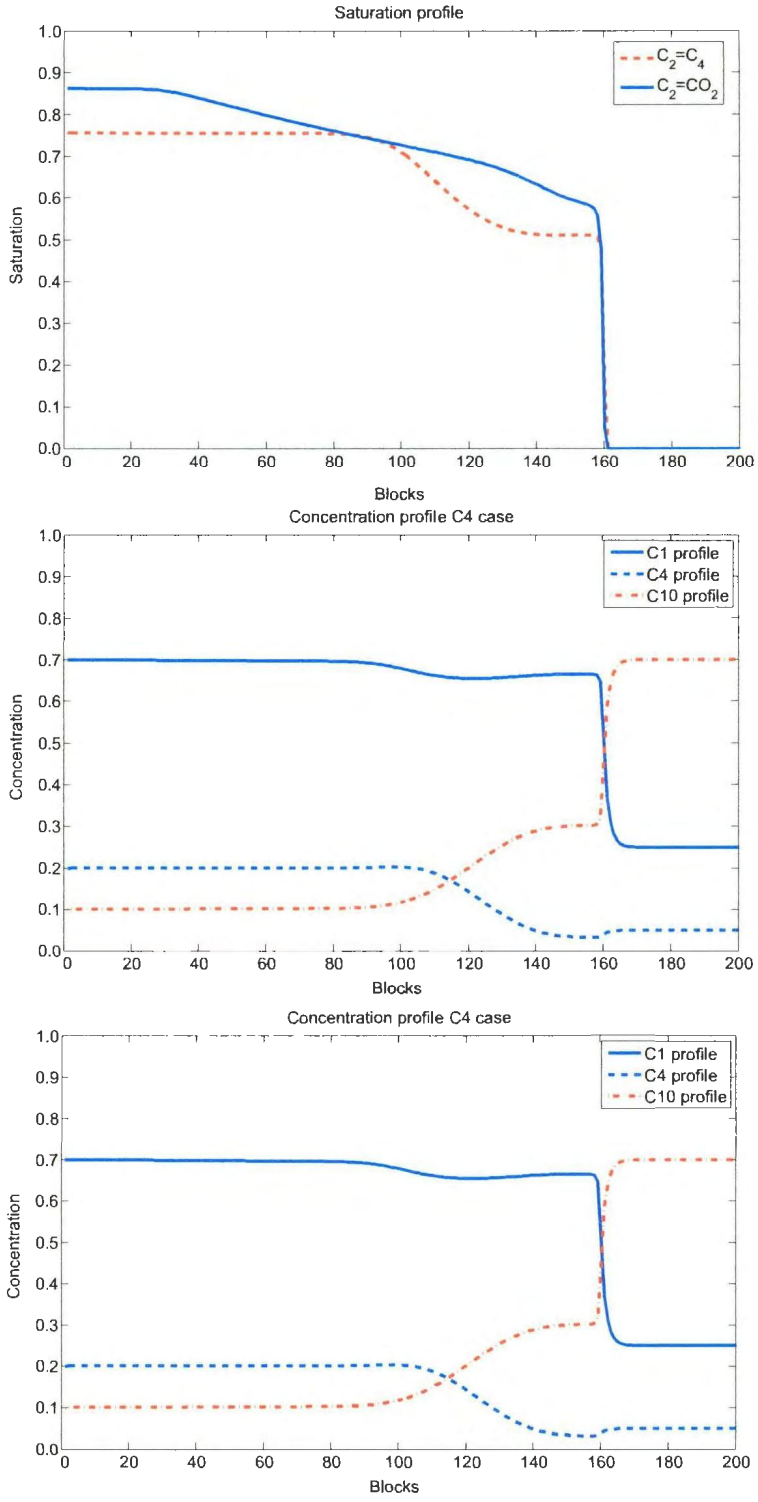

Figure 5.3: Profile solutions of both cases

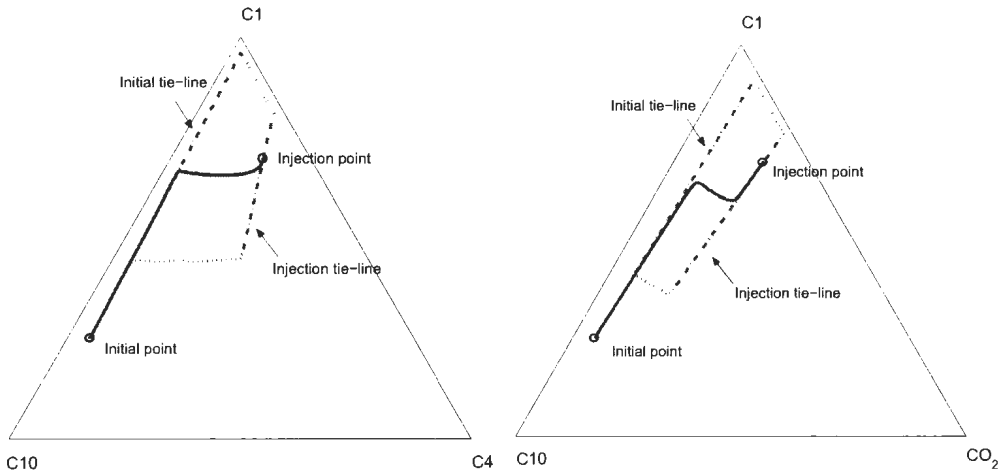

Figure 5.4: Composition path solutions

oped in this thesis does not capture behaviour of the miscible gas injection process, however a two dimensional simulation will show how the permeability variation affects component distribution and the flow path of the fluid.

The 2D simulation is conducted using a $50 \times 50 \times 0.02(m)$ grid setting. Using a quarter five-spot injection configuration, the injection cell is located at left bottom corner $(0, 0)$ block and the production cell is located at right top corner $(50, 50)$ block. For the first run, to simulate heterogeneity in the reservoir, the permeability distribution is generated using the built-in random number generation function in Matlab®. The generated permeability ranged from $3.87D$ to $0.11D$. The normalized permeability distribution map is shown in Fig.5.3 (a). In case study 2, a system of C1,CO_2 and C10 is used. The input data for the random permeability case is shown in Tab.5.3.

To demonstrate how heterogeneity is affecting fluid flow, a single rectangular low permeability region is set up in the second run while the rest of the flowing area remains a uniform higher permeability. This is shown in Fig.5.7 (a), where the high

Table 5.3: Case 2 input data

Injection composition (first run)	$C1 = 0.5$, $CO_2 = 0.4$
Injection composition (second run)	$C1 = 0.7$, $CO_2 = 0.2$
Initial composition	$C1 = 0.25$, $CO_2 = 0.05$
Injection pressure	$P_{inj} = 15MPa$
Production pressure	$P_{pro} = 10MPa$
Temperature	$T = 400K$
Reference Porosity	$\phi_0 = 0.18$
Rock compressibility	$cp = 9.1x10^{-9}(pa^{-1})$
Pore index	0.54
Residual oil saturaition	$S_{or} = 0$
Connate water saturation	$S_{wc} = 0$
Critical gas saturation	$S_{cg} = 0$

permeability region has a permeability of $K = 2D$ and low permeability region has a permeability of $K = 0.2D$. Between the low permeability and the high permeability regions, there is a gradually increasing transition with intermediate permeabilities. Injection composition is changed and other input parameters are kept same for both runs.

5.2.2.2 Results and conclusion

For the first run, the simulation is terminated at $t = 3.2h$. Fig.5.5 (b) shows the corresponding pressure distribution. Fig.5.6 (a) shows the profile solutions for the random permeability run. The displacing vapour phase distribution shows the fingering fronts. Beginning from the injection point, the injected vapour fluid diffuses into various directions due to the variation in permeability. The injection fluid begins to merge toward the outlet point from all directions. In Fig.5.6 (b), C1 moves at the displacing vapour phase edges. It can be shown from the CO_2 profile in Fig.5.6 (c), that CO_2 is more concentrated within the vapour phase and propagates more slowly than the other components. The component C10 mostly exists within the initial oil phase, as shown in Fig.5.6 (d); C10 becomes increasingly enriched toward the displacement

edges.

The solution using a randomly distributed permeability confirms that the heterogeneity of the displacement area is affecting the fluid flow pattern. Unlike the one-dimensional flow case, the component profile features (shocks and rarefaction) are determined by both the component phase behaviour and heterogeneity. In order to show exactly how a single heterogeneous region affects the local fluid flow in this random permeability field, a second run is conducted. This case uses a rectangular heterogeneous region as shown in Fig.5.7(a), and the simulation is terminated at $t = 8.39h$. The corresponding pressure distribution and the vapour phase profile is shown in Fig.5.7 (b) and 5.8 (a).

This solution clearly shows that when the injected phase is flowing from a relatively high permeability region and encounters a low permeability region, the fluid tends to avoid flowing though the low permeability region. The fluid flows more easily among the high permeability blocks, hence the fluid flow around the low permeability region is faster than the fluid flowing into the low permeability region. The fluid will flow through the low permeability region more slowly than the other region due to the difference in the permeabilities. In order words, the fluid will not enter the rectangular region if the rectangular region is not permeable such as a shale layer or sealed fault. The same features are shown for the components distributions in Fig.5.8 (b), (c) and (d). In Fig.5.9, from $t = 8.39h$ to $t = 12.46h$, the flowing trend of CO_2 can be clearly seen where the dashed rectangular area is the low permeability region.

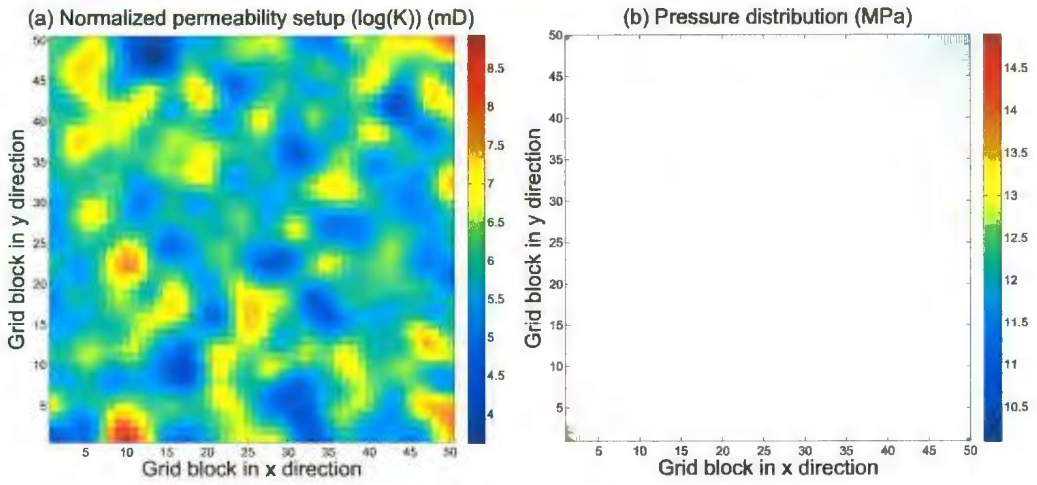

Figure 5.5: Permeability and pressure distribution (random permeability case)

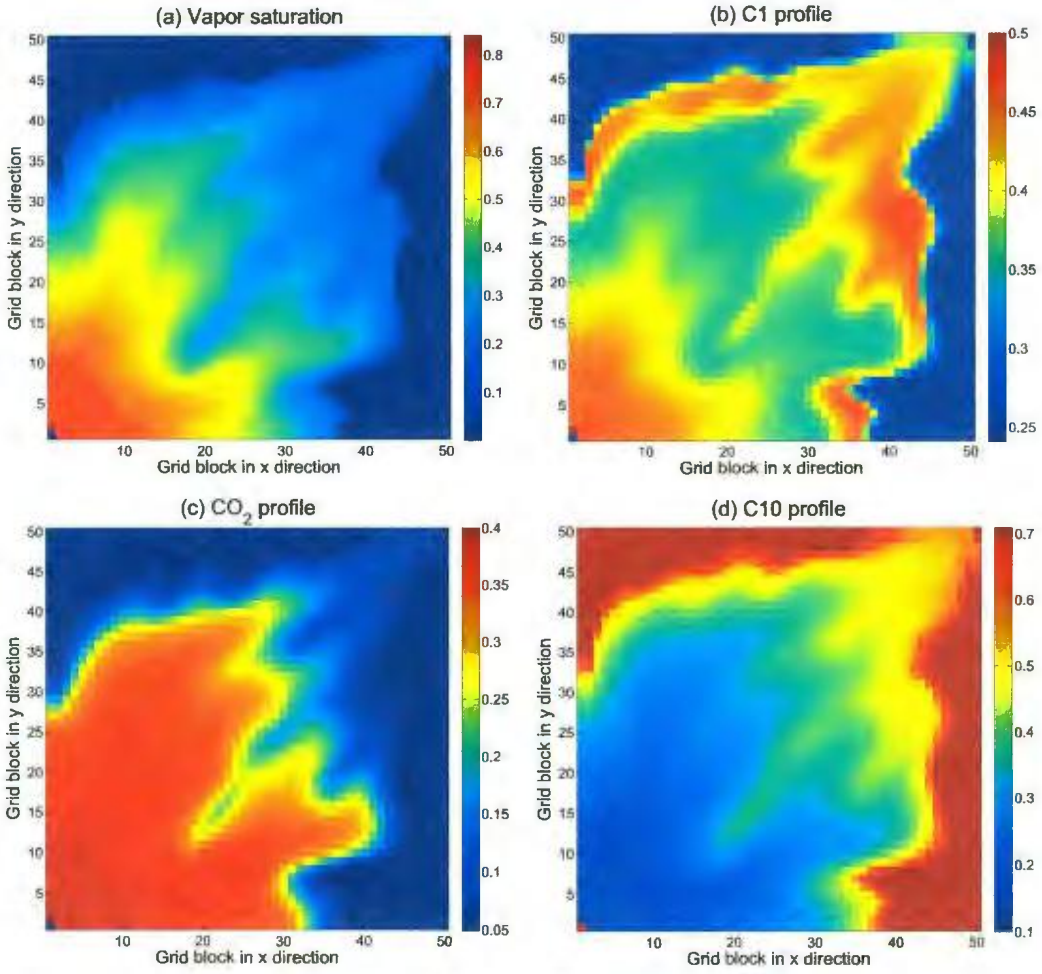

Figure 5.6: Profile solutions (random permeability case)

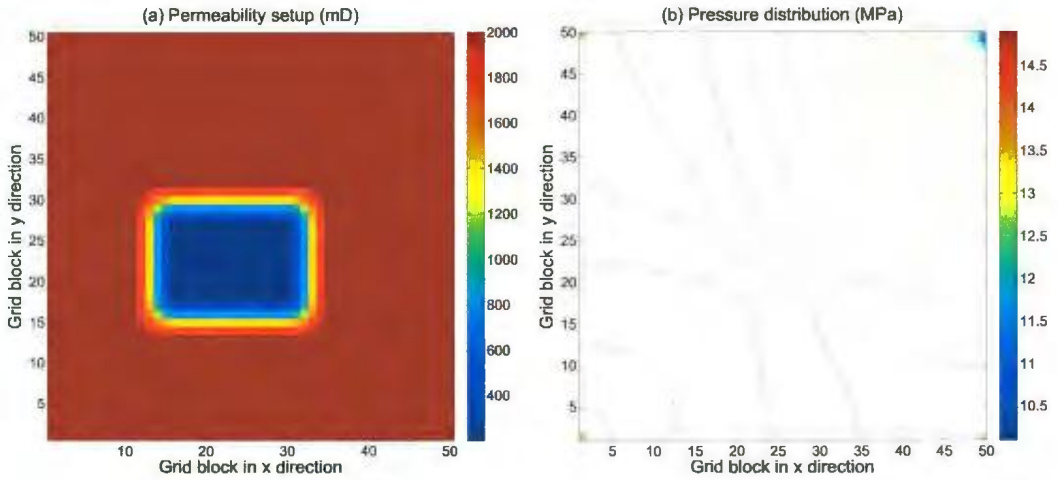

Figure 5.7: Permeability and pressure distribution (rectangular heterogeneity case)

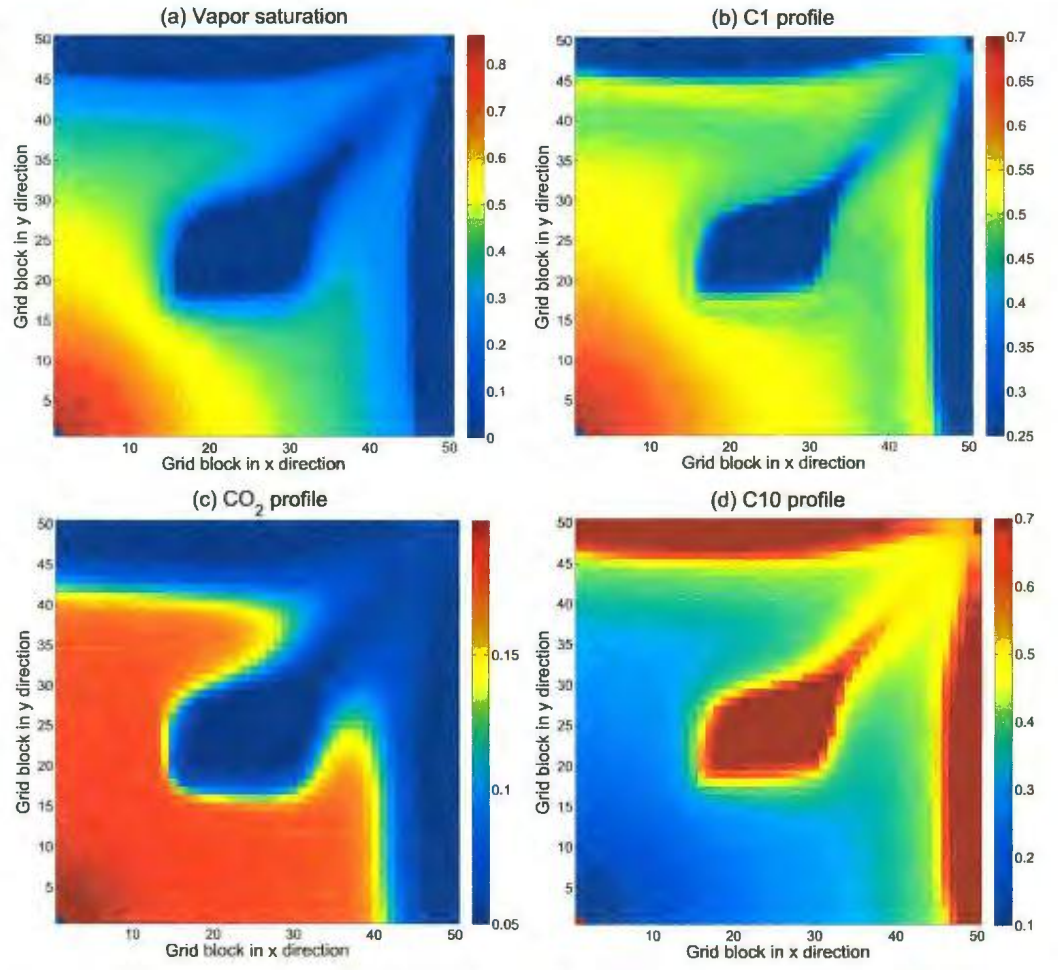

Figure 5.8: Profile solutions (rectangular heterogeneity case)

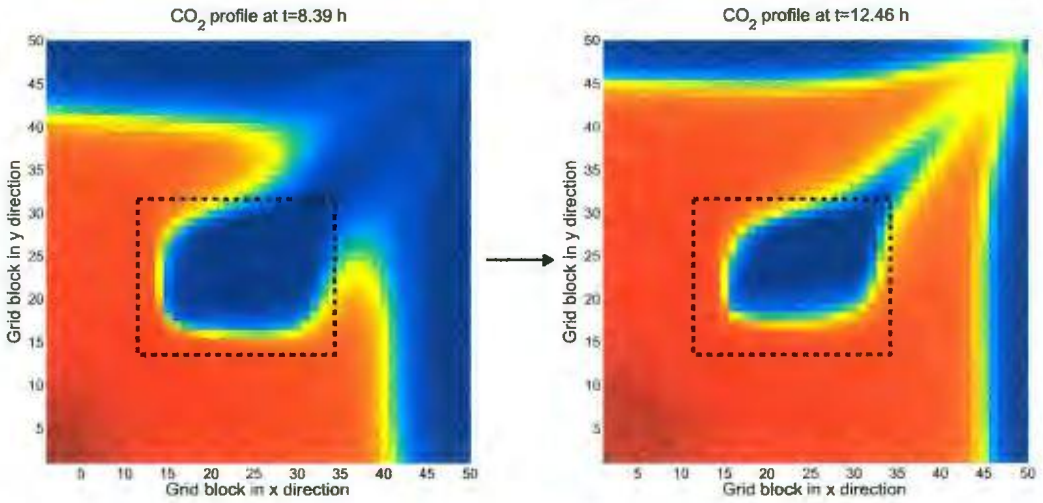

Figure 5.9: Flowing trend of CO_2

Chapter 6

Conclusion and Recommendations

6.1 Conclusion

The application of the calculation method for constant pressure boundaries to a three-component gas injection problem enables the direct calculation of the total volumetric flux, pressure distribution, saturation and concentration distribution at each specified time. The results illustrate that for different period of displacement, the global flux has a unique relationship with time when each elementary wave breaks through and also global flux is a continuous variable.

The results further show that the viscosity of the phases and the fraction of each phase will determine whether the total flux will be continuously increasing or decreasing. Throughout the calculation procedure, it is shown how the eigenvalue, viscosity ratio and other parameters affect the fluid flow rate and displacement performance from a mathematical point of view. Simulating such conditions of constant pressure boundaries is only possible using a numerical method of either an IMPES or a fully explicit formulation, both of which require large computation times. The analytical approach

provides the exact solution to the problem without the issues associated with numerical dispersion of numerical methods.

The development of the numerical compositional model results in a stable solution by using a single point upstream composition scheme. The simulation uses interpolation to determine the effect of viscosity variation and component properties on displacement performance. The results of the 2D case study demonstrate the effect of heterogeneity on the fluid distribution and the resulting fingering flow pattern. This modelling also provides the application of certain existing property correlations into the compositional model in terms of formulation.

A comparison of numerical solution to the analytical solution validates the numerical model. The comparison shows how the numerical solution converges to the analytical solution by refining the grid blocks. The analytical method provides an approach for simple problem calculation and fundamental theory. This can also be applied to the validation of the numerical method. Innovation and development of both analytical and numerical methods plays a important role for reservoir simulation.

6.2 Recommendations

The approach provided developed by Johansen and James (2012) is based on a generalized multi-component Riemann problem. The gas injection process and other EOR processes can be treated as two-, four- or multi-component problems. Based on the elementary wave solution of a four or multi-component problem, the calculation can be conducted in a straight forward way similar to the procedure shown in this thesis. In the aspect of streamline simulation using fixed pressure boundaries, the approach

by Johansen and James (2012) enables the application of fractional flow analysis along each flowing line. This extension in the streamline simulation method will provide a novel approach to analyze streamline behaviour.

This thesis complete the three component gas injection modelling with constant pressure boundaries. For future work, the wave analysis and calculation can be performed for a four- or multi-component problem. With more shocks and rarefactions present, the calculation will capture the flux behaviour for each of the elementary wave.

References

Arya, A.; Hewett, A.; Larson, R. G., and Lake, L. W. Disperson and reservoir heterogeneity. *SPE Reservoir Engineering*, 1988.

Bondor, P. L.; Hite, J. R., and Avasthi, S. M. Planning EOR projects in offshore oil fields. In *SPE Latin American and Caribbean Petroleum Engineering Conference*, 2005.

Brooks, R. H. and Corey, A. T. Hydraulic properties of porous media. *Hydro Paper*, 5, 1964.

Buckley, S. E. and Leverett, M. C. Mechanism of fluid displacement in sands. *Petrol. Trans. AIME*, 146:107, 1941.

Chang, Y.; Coats, B. K., and Nolen, J. S. A compositional model for CO_2 floods including CO_2 solubility in water. *SPE Reservoir Evaluation & Engineering*, 1998.

Chen, Z.; Qin, G., and Ewing, R. E. Analysis of a compositional model for fluid flow in porous media. *Society for Industrial and Applied Mathematics*, 60:747–777, 2000.

Chung, T. H.; Lee, L. L., and Starling, K. E. Application of kinetic gas theories and multiparameter correlation for prediction of dilute gas viscosity and thermal conductivity. *Industrial and Engineering Chemistry Research*, 23:8–13, 1984.

Chung, T. H.; Ajlan, M.; Lee, L. L., and Starling, K. E. Generalized multiparameter correlation for nonpolar and polar fluid transport properties. *Industrial and Engineering Chemistry Research*, 27:671–697, 1988.

Coats, K. H. Computer simulation of three-phase flow in reservoirs. *University of Texas*, 1968.

Danesh, A. *PVT and phase behaviour of petroleum reservoir fluids.* Elsevier Science & technology Books, 1998.

de Nevers, and Noel, . A calculation method for carbonated waterflooding. *Society of Petroleum Engineers*, March 1964:9–20, 1964.

Elsharkawy, A. M.; Hassan, S. A.; Hashim, Y. S. Kh., and Fahim, M. A. New compositional models for calculating viscosity of crude oils. *Canadian international petroleum conference*, 2003.

Firoozabadi, A.; Nutakkl, R.; Wong, T. W., and Aziz, K. EOS predictions of compressbility and phase behavior in systems containing water, hydrocarbons, and CO_2. *SPE Reservpor Engineering*, 1988.

Helfferich, F. and Klein, G. Theory of multicomponent, multiphase displacement in porous mdedia. *Society of Petroleum Engineers*, 21:52–62, February 1981.

Hite, J. R.; Avasthi, S. M., and Bondor, P. L. Planning EOR projects. In *SPE International Petroleum Conference*, 2004.

Hurter, S.; Labregere, D., and Berge, J. Simulation for CO_2 injection projects with compositional simulator. *Offshore Europe*, 2007.

Jensen, J. L.; Hinkley, D. V., and Lake, L. W. A statistical study of reservoir permeability: Distributions, correlations, and averages. *SPE Formation Evaluation*, 1987.

Jessen, K.; Stenby, E. H., and F. M. Orr, Jr. Interplay of phase behavior and numerical dispersion in finite-difference compositional simulation. *Society of Petroleum Engineers*, 2004.

Johansen, T. E. and James, L. A. Solutions of multi-component, two-phase riemann problems with constant pressure boundaires. *Pre-print, Memorial University*, 2012.

Johansen, T. E. and Winther, R. The solutioin of the riemann problem for a hyperbolic system of conservation laws modelling ploymer flooding. *SIAM j. of Math.Anal.*, 19: 219–34, 1988.

Johansen, T. E. and Winther, R. The riemann problem for multi component polymer flooding. *SIAM j. of Math.Anal.*, 20:541–66, 1989.

Johansen, T. E. and Winther, R. The riemann problem for a three component fluid system involving phase transitions. *Research note, institutt for energitiknikk*, 1990.

Lake, L. W. *Enhanced Oil Recovery.* Prentice Hall, 1989.

Lambert, M. E. A statistical study of reservoir heterogeneity. Master's thesis, U. of Texas, 1981.

Law, J. Statistical approach to the interstitial heterogeneity of sand reservoirs. *Trans., AIME*, 155:202–22, 1944.

Li, K. Theoretical development of the Brooks-Corey capillary pressure model from fractal modeling of porous media. *Society of Petroleum Engineers*, 2004.

Nghiem, L. X.; Fong, D. K., and Aziz, K. Compositional modeling with an equation of state. *Society of Petroleum Engineers*, 1981.

Orr, F. M. *Theory of Gas Injection Processes.* Tie-line publications, 2007.

Patton, J. T.; Coats, K. H., and Colegrove, G. T. Prediction of polymer flooding performance. *Society of Petroleum Engineers*, 251, 1971.

Peng, D. Y. and Robinson, D. B. A new two-constant equation of state. *Ind.Eng.Chem.Fundam.*, 15(1):59–64, 1976.

Poling, B. E.; Prausnitz, J. M., and O'Connell, J. P. *The Properties of Gases and Liquids.* McGraw-Hill, 2001.

Pope, G. A. The application of fractional flow theory to enhanced oil recovery. *Society of Petroleum Engineers*, 1980.

Quandalle, P.; Franlab, ; Savary, D., and CFP, . An implicit in pressure and saturations approach to fully compositional simulation. *Society of Petroleum Engineers*, 1989.

Rachford, H. H. and Rice, J. D. Procedure for use of electrical digital computers in calculating flash vaporization hydrocarbon equilibrium. *JPT*, 19, 1952.

Shutler, N. D. and Boberg, T. C. A one-dimensional analytical technique for predicting oil recovery by steamflooding. *Society of Petroleum Engineers*, 489-498, 1972.

Taber, J. J.; Kamath, I. S. K., and Reed, R. L. Mechanism of alcohol displacement of oil from porous media. *Society of Petroleum Engineers*, pages 195–212, 1961.

Thomas, B.; Iliyas, A.; Johansen, T. E.; Hawboldt, K.; Khan, F., and of Newfoundland, Memorial University. Towards sustainable and environmentally friendly enhanced oil recovery in offshore Newfoundland, Canada. In *Offshore Technology Conference*, 2010.

Welge, H. J.; Johnson, E. F.; Erving, S. P., and Brinkman, F. H. The linear displacement of oil from porous media by enriched gas. *J. Pet. Tech.*, 787-796, 1961.

Whitson, C. H. and Brule, M. R. *Phase Behavior.* Society of Petroleum Engineers, 2000.

Wilke, C. R. A viscosity equation for gas mixtures. *Journal of Chemical Physics*, 18: 517, 1950.

Wilson, G. M. A modified Redlich-Kwong equation of state, application to general physical data calculations. *AIChE Natl Meeting*, 1969.

Appendix A

Flash Calculation Package

The inputs for each component to the flash calculation package are: the critical pressure (P_c), the critical temperature (T_c), the acentric factor (ω), the pressure (P), the temperature (T) and the overall mole fraction (z). The flash calculation procedure has the following steps.

(1) Calculate the initial K-values

The initial approximation of the K-value of each component is calculated by using the Wilson (1969) equation:

$$K_i = \frac{exp(5.37(1+\omega_i)(1-T_{ri}^{-1}))}{P_{ri}} \tag{A.1}$$

where T_r is the reduced temperature and P_r is the reduced pressure defined as:

$$T_r = T/T_c;\ P_r = P/P_c \tag{A.2}$$

(2) Calculate the phase mole fraction and phase compositions

The Rachford-Rice (1952) equation is expressed as:

$$\sum_{i=1}^{nc} \frac{z_i(K_i - 1)}{1 + F_v(K_i - 1)} \tag{A.3}$$

where F_v is the vapour phase mole fraction and nc is the number of components. The initial approximated K-values and the overall compositions of the components are used in the Rachford-Rice equation and F_v is solved by using the Newton method. The liquid phase composition (x_i) and vapour phase composition (y_i) can be calculated by substituting F_v into the following equations:

$$x_i = \frac{z_i}{F_v(K_i - 1) + 1} \tag{A.4}$$

$$y_i = K_i x_i \tag{A.5}$$

(3) Solve the compressibility factor

The equation of state proposed by Peng and Robinson (1976) is expressed in terms of the compressibility factor (Z):

$$Z^3 - (1 - B)Z^2 + (A - 3B^2 - 2B)Z - (AB - B^2 - B^3) = 0 \tag{A.6}$$

where

$$A = \frac{aP}{RT^2};\ B = \frac{bP}{RT} \tag{A.7}$$

and

$$a = 0.457235\alpha R^2 T_c^2 / P_c \tag{A.8}$$

$$b = 0.077796 R T_c / P_c \tag{A.9}$$

$$\alpha = (1 + m(1 - \sqrt{T_r}))^2 \tag{A.10}$$

$$m = 0.37464 + 1.54226\omega - 0.26992\omega^2 \tag{A.11}$$

where P is the pressure, T is the temperature, R is the universal gas constant, ω is the acentric factor. The parameter A, B for either the vapour phase or the liquid phase are calculated using the mixing rule as:

$$A_L = \sum_{i=1}^{nc}\sum_{j=1}^{nc} x_i x_j (1 - k_{ij})\sqrt{A_i A_j} \tag{A.12}$$

$$A_V = \sum_{i=1}^{nc}\sum_{j=1}^{nc} y_i y_j (1 - k_{ij})\sqrt{A_i A_j} \tag{A.13}$$

$$B_L = \sum_{i=1}^{nc} x_i B_i \tag{A.14}$$

$$B_V = \sum_{i=1}^{nc} y_i B_i \tag{A.15}$$

where A_L and B_L are the parameters for the liquid phase, A_V and B_V are the parameters for the vapour phase. The binary interaction coefficient k_{ij} is assumed to be zero. The parameter A_i and B_i are calculated for each component using Eq.A.7.

The compressibility equation (Eq.A.6) can be set up for the liquid and vapour phases that the compressibility factor of the liquid phase (Z_L) and for the vapour phase (Z_V) can be solved, respectively.

(4) Calculate the fugacity

The Peng-Robinson equations of state in terms of fugacity and fugacity coefficient is expressed as:

$$\begin{aligned} ln\frac{f_i}{y_i P} = ln\phi_i = \frac{B_i}{B_m}(Z_m - 1) - ln(Z_m - B_m) \\ + \frac{A_m}{2\sqrt{2}B_m}(\frac{B_i}{B_m} - \frac{2}{A_m}\sum_{j=1}^{nc} y_j A_{ij}) ln[\frac{Z_m + (1+\sqrt{2})B_m}{Z_m - (1-\sqrt{2})B_m}] \end{aligned} \tag{A.16}$$

where f_i is the component fugacity, ϕ_i is the component fugacity coefficient, A_m, B_m are parameter for either the vapour or liquid phase and Z_m is the phase compressibility factor. The component fugacity and fugacity coefficient can be solved for both the liquid phase (f_{Li}, ϕ_{Li}) and the vapour phase (f_{Vi}, ϕ_{Vi}).

(5) Check the equal-fugacity constraint, update K-values

The constraint for the two-phase equilibrium condition is that the fugacity of each component of each phase is equal:

$$f_{Li} = f_{Vi}; i = 1, ..., nc \tag{A.17}$$

To check whether the K-values, phase compositions and phase mole fraction satisfy the constraint, the constraint condition can be checked by:

$$\sum_{i=1}^{nc} (\frac{f_{Li}}{f_{Vi}} - 1)^2 < \text{Tol} \tag{A.18}$$

where Tol is the convergence tolerance. We use 1×10^{-8} as the tolerance. If Eq.A.18 is not satisfied, the K-values are updated:

$$K_i^{l+1} = K_i^l (f_{Li}/f_{Vi}) \tag{A.19}$$

where l is the iteration level. The calculation returns to step (2) by using the updated K-values. The procedure [step (2) to step (5)] is repeated until the tolerance is satisfied (Eq.A.18).

(6) Calculation the molar density and the compressibility factor derivative term

The molar density of the liquid phase (ρ_L) and the vapour phase (ρ_V) can be calculated by:

$$\rho_L = \frac{P}{Z_L RT};\ \rho_V = \frac{P}{Z_V RT} \tag{A.20}$$

The derivative of the compressibility factor with respect to pressure in Eq.4.24 can be calculated by using the method provided by Firoozabadi et al. (1988):

$$\frac{\partial Z}{\partial P} = \frac{a}{R^2T^2}(\frac{B-Z}{D}) + \frac{b}{RT}(\frac{N}{D}) \tag{A.21}$$

$$D = 3Z^2 - 2(B+1-2B)Z - (B^2+2B^2+2B-A) \tag{A.22}$$

$$N = -Z^2 + (2B+4B+2)Z - (3B^2+2-A) \tag{A.23}$$

where Eq.A.21 to Eq.A.23 are set up bot the the liquid and the vapour phases.

(7) Calculate the saturation

The saturation of the liquid phase (S_o) and the vapour phase (S_g) are calculated by:

$$S_o = \frac{\rho_L(F_V - 1)}{F_V\rho_V - F_V\rho_L - \rho_V} \tag{A.24}$$

$$S_g = 1 - S_o \tag{A.25}$$

Appendix B

Source Code: 2D Compositional Simulator

B.1 Main Code

```
1  % #################    2D Compositional Simulator     ##################
2  %
3  %    - Modeling immeascible displacement process
4  %
5  %    - Ingoring capillary pressure, gravity term
6  %
7  %    - IMPES formulation for fixed inlet and outlet pressures
8  %
9  %    - Set for rectangle heterogenous region
10 %
11 %    - Single point upstream concentration scheme
12 %
13 %    - Code is set for corner five-spot injection configeration
```

```
%
%    - Due to flahs calculation limilation, pressure, temperature and
%      composition is prefered to be away from critical region
%
%    - Except for come coefficient, main variables are in SI units
%
%      >Developed by Xiaolong Liu for Mater thesis, MUN EOR group<
%-------------------------------------------------------------------------
%*************************************************************************
% Varialbe initialization
%*************************************************************************
%----------------------------------Input----------------------------------
length_x=input('Displacement length in x direction (m):');
length_y=input('Displacement length in y direction (m):');
grid_x=input('Grid number in x direction:');
grid_y=input('Grid number in x direction:');
nc=input('Number of component:');
K=input('Permeability:');
K_hetro=input('Permeability for heterogeneity:');
p_inj=input('Inlet pressure (MPa):');
p_init=input('Initial pressure (MPa):');
p_prod=input('Outlet pressure (MPa):');
z_inj=input('Injection composition [C1,C2,C3]:');
z_init=input('Initial composition [C1,C2,C3]:');
Sor=input('Residual oil saturation:');
Scg=input('Connate water saturation:');
Swc=input('Critical gas saturation:');
%Set grid block size and time step
dx=length_x/(grid_x+2);
dy=length_y/(grid_y+2);
dt=50*dx;
```

```
45 %-----------------------------Sample PVT constants-----------------------
46 %Fluid PVT properties, C1, CO2, C10 system
47 Pc=[4.599*10^6 7.38*10^6  2.11*10^6];%Critical pressure (Pa)
48 Tc=[190.56 304.19 617.7];%Critical temperature (K)
49 w=[0.0115 0.2276 0.4923];%Acentric factor
50 Vc=[0.0986 0.0940 0.6]*1000;%Critical molar volume
51 M=[16.043 44 142.285];%Molecular weight
52 dipole=[0 0 0];%Viscosity correlation parameter
53 T=400;% Reservoir temperature (K)
54 p_ref=20992230;%Reference pressure for porosity correlation (psi)
55 R=8.314;%Universal gas constant
56 speci_gravity_c7=0.7;%Specific gravity of of C7+ group
57 %-----------------------------Reservoir properties-----------------------
58 porosity_ref=0.18;%Porosity at reference pressure%
59 cp=0.91*10^(-8);%Rock compressibility%(psi-1)
60 %Set heterogenous region dimension hetero_l: legnth, heter_h: height
61 hetero_l=13;
62 hetero_h=18;
63 %Set heterogenous dimension 16 x 14 grids
64 hetero_dim=[16 14];
65 %Initialize permeability
66 K=ones(grid_y+2,grid_x+2)*K;%D
67 K(hetro_dim(1):hetro_dim(1)+hetero_l,...
68     hetero_dim(2):hetero_dim(2)+hetero_h)=K_hetero;
69 K_temp(1,:,:)=K;
70 K_temp=smooth3(smooth3(K_temp));
71 for i=1:grid_y+2
72     for j=1:grid_x+2
73         K(i,j)=K_temp(1,i,j);
74     end
75 end
```

```
%----------Declare variables----------
p=ones(grid_y+2,grid_x+2);%pressure
z=ones(grid_y+2,grid_x+2,nc);%overall molar concentration
sg=zeros(grid_y+2,grid_x+2);%vapor phase saturation
so=zeros(grid_y+2,grid_x+2);%oil phase saturation
density_o=zeros(grid_y+2,grid_x+2);%molar density of oil phase
density_g=zeros(grid_y+2,grid_x+2);%molar density of vapor phase
ddensity_g=zeros(grid_y+2,grid_x+2);%deriative of vapor density
ddensity_o=zeros(grid_y+2,grid_x+2);%deriative of oil density
x=zeros(grid_y+2,grid_x+2,nc);%flashed oil phase composition
y=zeros(grid_y+2,grid_x+2,nc);%flahsed vapor phase composition
X=zeros(grid_y+2,grid_x+2,nc);%true oil phasae composition
Y=zeros(grid_y+2,grid_x+2,nc);%true vapor phase composition
vo=zeros(grid_y+2,grid_x+2);%oil viscosity
vg=zeros(grid_y+2,grid_x+2);%vapor viscosity
%solver coefficients
alpha=zeros(grid_y+2,grid_x+2);
delta=zeros(grid_y+2,grid_x+2);
a=zeros(1,grid_x*grid_y);
b=zeros(1,grid_x*grid_y);
c=zeros(1,grid_x*grid_y);
d=zeros(1,grid_x*grid_y);
e=zeros(1,grid_x*grid_y);
F=zeros(1,grid_x*grid_y);
%----------Initialize variables----------
%Initialize pressure and composition
p(1:grid_y+2,1:grid_x+2)=p_init;
z(:,:,1)=z_init(1);
z(:,:,2)=z_init(2);
z(:,:,3)=z_init(3);
p(2,1)=p_inj;
```

```
107 z(2,1,1)=z_inj(1);
108 z(2,1,2)=z_inj(2);
109 z(2,1,3)=z_inj(3);
110 p(grid_y+1,grid_x+2)=p_prod;
111 %Initialization flash
112 for i=1:grid_y+2
113     for j=1:grid_x+2
114         [ddensity_o(i,j) ddensity_g(i,j) density_g(i,j)...
115             density_o(i,j) so(i,j) sg(i,j) x(i,j,:) y(i,j,:)]=...
116             function_flash(nc,p(i,j),T,z(i,j,:),Pc,Tc,w,Swc);
117     end
118 end
119 %Initialize viscosities
120 for i=1:grid_x+2
121     for j=1:grid_y+2
122         vg(i,j)=...
123             function_gasviscosity(Tc,w,M,Vc,dipole,Y(i,j,:),T,nc);
124         vo(i,j)=...
125             function_oilviscosity(T,p(i,j),X(i,j,:),speci_gravity_c7);
126     end
127 end
128 %Initialize porosity
129 porosity=porosity_ref*(1+cp*(p-p_ref));
130 %Initialize relative permeability
131 kro=((1-sg-Sor)/(1-Scg-Sor)).^2;
132 krg=((sg-Scg)/(1-Scg-Sor)).^2;
133 %Initialize directional permeability
134 Kx=(dx)./(dx./K(2:grid_y+1,1:grid_x+1)+dx./K(2:grid_y+1,2:grid_x+2));
135 Ky=(dy)./(dy./K(1:grid_y+1,2:grid_x+1)+dy./K(2:grid_y+2,2:grid_x+1));
136 %Initialize directional phase mobility
137 Tox=Kx.*(kro(2:grid_y+1,1:grid_x+1))./vo;
```

```
Tgx=Kx.*(krg(2:grid_y+1,1:grid_x+1))./vg;
Toy=Ky.*(kro(1:grid_y+1,2:grid_x+1))./vo;
Tgy=Ky.*(krg(1:grid_y+1,2:grid_x+1))./vg;
%**************************************************************************
% Main loop
%**************************************************************************
%Set counter
counter=0;
%Main loop
while sg(49,49)≤0.45
    %Calculate matrix coefficient
    for i=1:grid_y
        for j=1:grid_x
            alpha(i+1,j+1)=density_o(i+1,j+1)*so(i+1,j+1)+...
                density_g(i+1,j+1)*sg(i+1,j+1);
            dporosity=porosity_ref*cp;%d(porosity)/dp
            delta(i+1,j+1)=(alpha(i+1,j+1)*...
                dporosity+porosity(i+1,j+1)*(so(i+1,j+1)*...
                ddensity_o(i+1,j+1)+sg(i+1,j+1)*...
                ddensity_g(i+1,j+1)))/dt; %d(alpha*phi)/dt
        end
    end
    for i=1:grid_y
        for j=1:grid_x

            a(grid_x*(i-1)+j)= (Tgy(i,j)  +Toy(i,j))/dy^2;
            b(grid_x*(i-1)+j)= (Tgx(i,j)  +Tox(i,j))/dx^2;
            c(grid_x*(i-1)+j)=(-Tgx(i,j+1)-Tgx(i,j))/dx^2+...
                (-Tgy(i+1,j)-Tgy(i,j))/dy^2+(-Tox(i,j+1)-...
                Tox(i,j))/dx^2+(-Toy(i+1,j)-Toy(i,j))/dy^2-...
                delta(i+1,j+1);
```

```
169             d(grid_x*(i-1)+j)= (Tgx(i,j+1)+Tox(i,j+1))/dx^2;
170             e(grid_x*(i-1)+j)= (Tgy(i+1,j)+Toy(i+1,j))/dy^2;
171
172             F(grid_x*(i-1)+j)=-delta(i+1,j+1)*p(i+1,j+1);
173
174         end
175     end
176     %build ceof matrix
177     mn=grid_x*grid_y;
178     c(1:grid_x)=c(1:grid_x)+a(1:grid_x);
179     c(mn-grid_x+1:mn)=c(mn-grid_x+1:mn)+e(mn-grid_x+1:mn);
180     c(grid_x+1:grid_x:grid_x*grid_y-grid_x+1)=...
181         c(grid_x+1:grid_x:grid_x*grid_y-grid_x+1)+...
182         b(grid_x+1:grid_x:grid_x*grid_y-grid_x+1);
183     c(grid_x:grid_x:grid_x*grid_y-grid_x)=...
184         c(grid_x:grid_x:grid_x*grid_y-grid_x)+...
185         d(grid_x:grid_x:grid_x*grid_y-grid_x);
186     aa=sparse(1:mn,1:mn,c(1:mn),mn,mn);
187     bb=sparse(1:mn-grid_x,grid_x+1:mn,e(1:mn-grid_x),mn,mn);
188     cc=sparse(grid_x+1:mn,1:mn-grid_x,a(grid_x+1:mn),mn,mn);
189     dd=sparse(1:mn-1,2:mn,d(1:mn-1),mn,mn);
190     ee=sparse(2:mn,1:mn-1,b(2:mn),mn,mn);
191     A=aa+bb+cc+dd+ee;
192     A(grid_x:grid_x:mn-grid_x,grid_x+1:grid_x:mn-grid_x+1)=0;
193     A(grid_x+1:grid_x:mn-grid_x+1,grid_x:grid_x:mn-grid_x)=0;
194     F(1)=F(1)-b(1)*p_inj;
195     F(grid_x*grid_y)=F(grid_x*grid_y)-d(grid_x*grid_y)*p_prod;
196     %Solve
197     u=A\F';
198     for i=1:grid_y
199         for j=1:grid_x
```

```
200             p(i+1,j+1)=u(grid_x*(i-1)+j);
201         end
202     end
203     %update pressure
204     p(1,2:grid_x+1)=p(2,2:grid_x+1);
205     p(grid_y+2,2:grid_x+1)=p(grid_y+1,2:grid_x+1);
206     p(3:grid_y+1,1)=p(3:grid_y+1,2);
207     p(2:grid_y,grid_x+2)=p(2:grid_y,grid_x+1);
208     po=p;
209     %Get true phase composition
210     for i=1:grid_y+2
211         for j=1:grid_x+2
212             X(i,j,:)=x(i,j,:);
213             Y(i,j,:)=y(i,j,:);
214             if so(i,j)==1
215                 X(i,j,:)=z(i,j,:);
216             end
217             if sg(i,j)==1
218                 Y(i,j,:)=z(i,j,:);
219             end
220         end
221     end
222     %Calculate composition
223     for i=1:grid_y
224         for j=1:grid_x
225             phase_flux=(Tgx(i,j+1)*((p(i+1,j+1+1)-p(i+1,j+1))/dx)-...
226                 Tgx(i,j)*((p(i+1,j+1)-p(i+1,j))/dx)+
227                 Tox(i,j+1)*((po(i+1,j+1+1)-po(i+1,j+1))/dx)-...
228                 Tox(i,j)*((po(i+1,j+1)-po(i+1,j))/dx))/dx+
229                 (Tgy(i+1,j)*((p(i+1+1,j+1)-p(i+1,j+1))/dy)-...
230                 Tgy(i,j)*((p(i+1,j+1)-p(i,j+1))/dy)+
```

```
231                 Toy(i+1,j)*((po(i+1+1,j+1)-po(i+1,j+1))/dy)-...
232                 Toy(i,j)*((po(i+1,j+1)-po(i,j+1))/dy))/dy;
233             component_flux(i,j,1:nc)=(Y(i+1,j+1,1:nc)*Tgx(i,j+1)*...
234                 ((p(i+1,j+1+1)-p(i+1,j+1))/dx)-...
235                 Y(i+1,j,1:nc)*Tgx(i,j)*((p(i+1,j+1)-p(i+1,j))/dx)+...
236                 X(i+1,j+1,1:nc)*Tox(i,j+1)*...
237                 ((po(i+1,j+1+1)-po(i+1,j+1))/dx)-...
238                 X(i+1,j,1:nc)*Tox(i,j)*((po(i+1,j+1)-...
239                 po(i+1,j))/dx))/dx+...
240                 (Y(i+1,j+1,1:nc)*Tgy(i+1,j)*...
241                 ((p(i+1+1,j+1)-p(i+1,j+1))/dy)-...
242                 Y(i,j+1,1:nc)*Tgy(i,j)*((p(i+1,j+1)-p(i,j+1))/dy)+ ...
243                 X(i+1,j+1,1:nc)*Toy(i+1,j)*...
244                 ((po(i+1+1,j+1)-po(i+1,j+1))/dy)-...
245                 X(i,j+1,1:nc)*Toy(i,j)*...
246                 ((po(i+1,j+1)-po(i,j+1))/dy))/dy;
247             for ic=1:nc
248                 z(i+1,j+1,ic)=(component_flux(i,j,ic)*...
249                 dt+porosity(i+1,j+1)*alpha(i+1,j+1)*z(i+1,j+1,ic))/...
250                 (porosity(i+1,j+1)*alpha(i+1,j+1)+phase_flux*dt)  ;
251             end
252
253         end
254     end
255     %Normalize composition
256     for i=1:grid_y+2
257         for j=1:grid_x+2
258             sumz=sum(z(i,j,1:nc));
259             z(i,j,1:nc)=z(i,j,1:nc)/sumz;
260         end
261     end
```

```
262     %Reset no flow boundaries
263     for ic=1:nc
264         z(1,2:grid_x+1,ic)=z(2,2:grid_x+1,ic);
265         z(grid_y+2,2:grid_x+1,ic)=z(grid_y+1,2:grid_x+1,ic);
266         z(3:grid_y+1,1,ic)=z(3:grid_y+1,2,ic);
267         z(2:grid_y,grid_x+2,ic)=z(2:grid_y,grid_x+1,ic);
268     end
269     %Flash procedure using new pressure and composition
270     for i=1:grid_y+2
271         for j=1:grid_x+2
272             [ddensity_o(i,j) ddensity_g(i,j) density_g(i,j) ...
273             density_o(i,j) so(i,j) sg(i,j) x(i,j,:) y(i,j,:)]...
274             =function_flash(nc,p(i,j),T,z(i,j,:),Pc,Tc,w,Swc);
275         end
276     end
277     %Update variables
278     porosity=porosity_ref*(1+cp*(p-p_ref));
279     kro=((1-sg-Sor)/(1-Scg-Sor)).^2;
280     krg=((sg-Scg)/(1-Scg-Sor)).^2;
281     for i=1:grid_x+2
282         for j=1:grid_y+2
283             vg(i,j)=...
284                 function_gasviscosity(Tc,w,M,Vc,dipole,Y(i,j,:),T,nc);
285             vo(i,j)=...
286                 function_oilviscosity(T,p(i,j),X(i,j,:),...
287                 speci_gravity_c7);
288         end
289     end
290     for i=1:grid_y+1
291         for j=1:grid_x
292             %Determine upstream block
```

```
293             if p(i,j+1)≥p(i+1,j+1)
294                 Toy(i,j)=Ky(i,j)*kro(i,j+1)./vo;
295                 Tgy(i,j)=Ky(i,j)*krg(i,j+1)./vg;
296             end
297             if p(i,j+1)<p(i+1,j+1)
298                 Toy(i,j)=Ky(i,j)*kro(i+1,j+1)./vo;
299                 Tgy(i,j)=Ky(i,j)*krg(i+1,j+1)./vg;
300             end
301         end
302     end
303     for i=1:grid_y
304         for j=1:grid_x+1
305             if p(i+1,j)≥p(i+1,j+1)
306                 Tox(i,j)=Kx(i,j)*kro(i+1,j)./vo;
307                 Tgx(i,j)=Kx(i,j)*krg(i+1,j)./vg;
308             end
309             if p(i+1,j)<p(i+1,j+1)
310                 Tox(i,j)=Kx(i,j)*kro(i+1,j+1)./vo;
311                 Tgx(i,j)=Kx(i,j)*krg(i+1,j+1)./vg;
312             end
313         end
314     end
315     %Set counter
316     counter=counter+1;
317 end
318 %-------------------------------End of main loop-------------------------
319 %Get simulation time
320 time_elapsed=counter*dt;
321 %*****************************************************************************
322 %End of main code
323 %*****************************************************************************
```

B.2 Flash Calculation Package

```
%########################## Function flash ##############################
%  -Function input:
%        nc- number of component
%        P - pressure
%        T - temperature
%        z - overall composition
%        Pc - critical pressure
%        Tc - critical temperature
%        w - acentric factor
%        Swc - connate water saturation
%  -Function output
%        density derivative terms
%        phase compositions
%        saturations
%-------------------------------------------------------------------------
function [ddensityo ddensityg densityg densityo so sg x y]=...
    function_flash(nc,P,T,z,Pc,Tc,w,Swc)
%Set error
error=1;
%Set tolorence
Tol=1*10^(-8);
%Initialize PR EOS parameters
for i=1:nc
    Tr(i)=T/Tc(i);
    ac(i)=0.4574*R^2*Tc(i)^2/Pc(i);
    m(i)=0.37464+1.54226*w(i)-0.26992*w(i)^2;
    if w(i)>0.4;
        m(i)=0.3796+1.485*w(i)-0.1644*w(i)^2+0.01667*w(i)^3;
```

```
29      end
30      alpha(i)=(1+m(i)*(1-Tr(i)^0.5))^2;
31      a(i)=ac(i)*alpha(i);
32      b(i)=0.0778*R*Tc(i)/Pc(i);
33      A(i)=a(i)*P/(R*T)^2;
34      B(i)=b(i)*P/(R*T);
35  end
36  %Initial approximation of K-values
37  for i=1:nc
38      K(i)=(Pc(i)/P)*exp(5.37*(1+w(i))*(1-Tc(i)/T));
39  end
40  % flash starts
41  while (error≥Tol)
42      %Fist guess of vapor volume fraction
43      Fv=0.9;
44      Fvold=0;
45      while (abs(Fv-Fvold)≥Tol)
46          Fvold=Fv;
47          h=0;
48          dh=0;
49          for i=1:nc
50              h=h+z(i)*(K(i)-1)/(Fv*(K(i)-1)+1);
51              dh=dh-z(i)*(K(i)-1)^2/(Fv*(K(i)-1)+1)^2;
52          end
53          Fv=Fvold-h/dh;
54      end
55      %calculate PR EOS component parameters
56      for i=1:nc
57          x(i)=z(i)/(Fv*(K(i)-1)+1);
58          y(i)=K(i)*x(i);
59      end
```

```
60      BL=0;
61      BV=0;
62      AL=0;
63      AV=0;
64      %calculate mixture EOS parameters
65      for i=1:nc
66          for k=1:nc
67              Aij(i,k)=(1-bina(i,k))*(A(i)*A(k))^0.5;
68              AL=AL+x(i)*x(k)*Aij(i,k);
69              AV=AV+y(i)*y(k)*Aij(i,k);
70          end
71      end
72      for i=1:nc
73          BL=BL+x(i)*B(i);
74          BV=BV+y(i)*B(i);
75      end
76      %cubic equation parameters
77      a1L=-(1-BL); a2L=(AL-2*BL-3*BL^2); a3L=-(AL*BL-BL^2-BL^3);
78      a1V=-(1-BV); a2V=(AV-2*BV-3*BV^2); a3V=-(AV*BV-BV^2-BV^3);
79      rL=roots([1 a1L a2L a3L]);
80      rV=roots([1 a1V a2V a3V]);
81      %choose real roots
82      ZL=min(rL);
83      ZV=max(rV);
84      xA=zeros(1,nc);
85      yA=zeros(1,nc);
86      for i=1:nc
87          for j=1:nc
88              xA(i)=xA(i)+x(j)*Aij(i,j);
89              yA(i)=yA(i)+y(j)*Aij(i,j);
90          end
```

```
91      end
92      %calculate partial fugacity for each component in each phase
93      for i=1:nc
94          PhiL(i)=exp((B(i)/BL)*(ZL-1)-log(ZL-BL)-...
95              (AL/(2*sqrt(2)*BL))*(-B(i)/BL+(2/AL)*xA(i))*...
96              log((ZL+(1+sqrt(2))*BL)/(ZL+(1-sqrt(2))*BL)));
97          fL(i)=x(i)*P*PhiL(i);
98          PhiV(i)=exp((B(i)/BV)*(ZV-1)-log(ZV-BV)-...
99              (AV/(2*sqrt(2)*BV))*(-B(i)/BV+(2/AV)*yA(i))*...
100             log((ZV+(1+sqrt(2))*BV)/(ZV+(1-sqrt(2))*BV)));
101         fV(i)=y(i)*P*PhiV(i);
102     end
103     %check wheather equilibrium achieved and update K values
104     temp=0;
105     for i=1:nc
106         temp=temp+(fL(i)/fV(i)-1)^2;
107         K(i)=K(i)*(fL(i)/fV(i));
108     end
109     error=temp;
110 end
111 %end of flash calculation
112 %-----------------molar density calculation-----------------------------
113 vL=ZL*R*T/P;
114 vV=ZV*R*T/P;
115 DL=3*ZL^2-2*(BL+1-U*BL)*ZL+(W*BL^2-U*BL^2-U*BL+AL);
116 NL=(1-U)*ZL^2+(-2*W*BL+2*U*BL+U)*ZL+(3*W*BL^2+2*W*BL+AL);
117 DV=3*ZV^2-2*(BV+1-U*BV)*ZV+(W*BV^2-U*BV^2-U*BV+AV);
118 NV=(1-U)*ZV^2+(-2*W*BV+2*U*BV+U)*ZV+(3*W*BV^2+2*W*BV+AV);
119 dZL=(AL/P)*((BL-ZL)/DL)+(BL/P)*(NL/DL);
120 dZV=(AV/P)*((BV-ZV)/DV)+(BV/P)*(NV/DV);
121 ddensityo=(1/(R*T*ZL))*(1-(P/ZL)*dZL);
```

```
122 ddensityg=(1/(R*T*ZV))*(1-(P/ZV)*dZV);
123 densityo=1/vL;
124 densityg=1/vV;
125 %-------------------------saturation-------------------------
126 %if vapor liquid phase only
127 if Fv<0
128     so=1-Swc;
129 end
130 %if vapor phase only
131 if Fv>0
132     so=0;
133 end
134 %if two phases, get density and saturation respectively
135 if Fv>0 && Fv<1
136     so=densityg*(Fv-1)/(Fv*densityg-Fv*densityo-densityg);
137 end
138 sg=1-so-Swc;
139 %-------------------------End of function flash-------------------------
```

Appendix C

Pre-print: Solutions of Multi-Component, Two-Phase Riemann Problems with Constant Pressure Boundares

Solutions of Multi-Component, Two- Phase Riemann Problems with Constant Pressure Boundaries

Thormod E. Johansen[1] and Lesley A. James[2]

Faculty of Engineering & Applied Science
Memorial University of Newfoundland
St. John's, Newfoundland A1B 3X5
Canada

001-709-864-3431[1]; 001-709-864-2485[2]
001-709-864-4042
thormodj@mun.ca[1]; ljames@mun.ca[2]

Abstract

Solutions of Riemann problems have been used to describe the linear, incompressible, fluid displacement in a porous medium under constant total volumetric flux conditions without dispersion. These solutions of the governing hyperbolic system of conservation laws are composed of a series of shock waves and smooth rarefaction waves. Realistically, reservoirs are often produced under constant pressure boundaries with constant injection well pressures and constant production well pressures. In this paper we extend solutions of Riemann problems for constant flux conditions to solutions of the associated Riemann problem for constant pressure boundaries. This is done by deriving explicit closed form expressions for the volumetric flux as a function of time. The construction is carried out in an algorithmic fashion by considering each wave before and after the wave breaks through at the outlet end. Expressions for the time of breakthrough for each wave are also derived, together with the pressure distribution between inlet and outlet at any time. Generalized formulas for time dependent boundary conditions are also shown to follow easily from the constant pressure boundary case. Finally in this paper, we present two waterflooding cases and one polymer flooding case for constant pressure boundaries to demonstrate and exemplify the main results of the paper. In particular, it is demonstrated that the constant flux solution cannot be used as approximations for constant pressure boundaries cases, as the change in volumetric flux over time in such cases is very significant.

Key words: Riemann problems; constant pressure boundaries; analytical solutions

EOR: Enhanced Oil Recovery

1. Introduction

Consider a hyperbolic system of conservation laws such as an n-component, two phase model for one dimensional flow in porous media subject to standard fractional flow assumptions (incompressible flow with negligible dispersion and no volume change upon mixing). If $F_i = F_i(u_1,...,u_{n-1})$ is the fractional flux function for component i, and $\boldsymbol{u} = [u_1,....,u_{n-1}]$ represents the overall volume fractions of the fluid components $(\sum_1^n u_i = 1)$, the conservation of mass model under consideration may be written as

$$\phi \frac{\partial}{\partial t}[u_i + a_i(\boldsymbol{u})] + U_T \frac{\partial F_i}{\partial x} = 0 \; ; i = 1,...,n-1 \quad , \tag{1.1}$$

where $a(\boldsymbol{u})$ is volume fraction of the stagnant part of component i, e.g. caused by adsorption on the rock surface. Furthermore, ϕ is porosity and U_T is the total volumetric flux. If we have two phases, $F_i = fu_{i1} + (1-f)u_{i2}$ and $u_i = su_{i1} + (1-s)u_{i2}$ where u_{ij} is volume fraction of component i in phase j, s is saturation of phase 1 and $f = U_1 / U_T$ is the fractional flow function of phase 1. The model can be reformulated as

$$\frac{\partial \boldsymbol{u}}{\partial t} + \frac{U_T}{\phi} \boldsymbol{A}(\boldsymbol{u}) \frac{\partial \boldsymbol{u}}{\partial x} = 0 \quad , \tag{1.2}$$

where $\boldsymbol{A}(\boldsymbol{u})$ is the $(n-1)\times(n-1)$ Jacobian of $\boldsymbol{F} = [F_1(\boldsymbol{u}),..., F_{n-1}(\boldsymbol{u})]$ with *real* eigenvalues $\lambda_1,....,\lambda_{n-1}$ (since we assume the system in equation (1.2) is hyperbolic).

A Riemann problem for (1.2) is an initial/boundary value problem with constant states

$$\begin{aligned} \boldsymbol{u}(0,t) &= \boldsymbol{u}^L \; ; t \geq 0 \\ \boldsymbol{u}(x,0) &= \boldsymbol{u}^R \; ; 0 \leq x \leq L \end{aligned} \tag{1.3}$$

where L is the length of the 1D medium. For the cases when the total volumetric flux U_T is constant in *both* t *and* x, some Riemann problems of the form (1.2), (1.3) have known solutions, as reviewed below. However, if the pressures at the boundaries $p_{in} = p(0,t)$; $p_{out} = p(L,t)$ are kept constant, U_T will *no longer be constant as a function of* t. Therefore, the known Riemann problem solutions no longer hold true.

The main result of this paper is to prove the following

Theorem

If the solution of a Riemann problem of the form, (1.2), (1.3) *is known in the case of* U_T *being a given constant in both* x *and* t, *the associated Riemann problem with initial/boundary conditions*

$$\begin{aligned} &\boldsymbol{u}(0,t) = \boldsymbol{u}^L \quad ; t \geq 0 \\ &\boldsymbol{u}(x,0) = \boldsymbol{u}^R \quad ; 0 \leq x \leq L \\ &p(0,t) = p_{in} \quad ; t \geq 0 \\ &p(L,t) = p_{out} \quad ; t \geq 0 \end{aligned} \tag{1.4}$$

also has a solution which can be determined directly from the existing solution for constant U_T.

For constant pressure boundaries, the volumetric flux will be constant as a function of x because of the incompressibility assumption, however $U_T = U_T(t)$ will be time dependent.

The proof of the above Theorem is constructive through the design of an analytical algorithm for construction of the function $U_T = U_T(t)$. The proof is given in Section 2.

The constant volumetric flux solution consists of a sequence of self -similar waves (i.e. waves that can be described as a function of $\xi = x/t$) connecting the two states $\boldsymbol{u}^L, \boldsymbol{u}^R$, in such a way that the overall wave velocity increases from $\boldsymbol{u}^L$ to $\boldsymbol{u}^R$. Each of these elementary waves belongs to one of the eigenvalues $\lambda_1, ..., \lambda_{n-1} = x/t$ either as a Rarefaction wave (smooth) or a Shock wave

(including contact discontinuity). Any two adjacent waves are separated by a constant state. The solution of the associated problem with constant pressure boundaries and the constant flow rate solution are congruent in the sense that either solution at a given time can be obtained from the other. However, self-similarity of the solution holds true only for the constant volumetric flux case. The sequence of elementary waves is illustrated in Figure 1, where also the nomenclature used in this paper is defined.

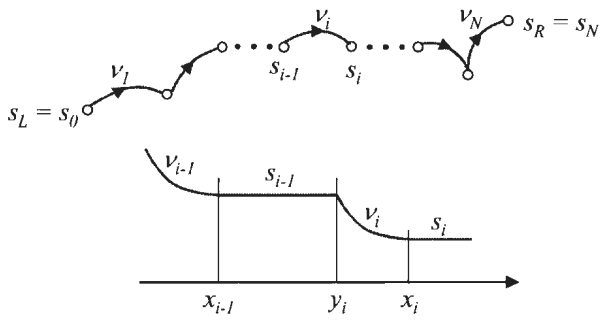

Fig. 1 Elementary Waves

We assume that each wave can be defined by the parameter s (e.g. phase 1 saturation). The leading edge of the wave v_i is x_i and the trailing edge is y_i. For shocks, $x_i = y_i$. Also, it is possible to have $x_{i-1} = y_i$, such as in the Buckley Leverett solution for waterflooding, where a shock has the same velocity as the leading edge of the trailing rarefaction wave.

Any two waves v_{i-1}, v_i are separated by a constant state s_{i-1}. Consider the case where v_i is a rarefaction wave, parameterized by s. We do not assume that the system is strictly hyperbolic, hence $\lambda_i - \lambda_k$ may change sign for any pair of eigenvalues. Hence, we cannot assume that the elementary waves correspond one by one to a sequence of increasing eigenvalues. Instead, for rarefaction waves, $v_i(s) = \lambda_k(s)$ for some k. If v_i is a shock, it must satisfy the Rankine-Hugoniot condition (shock mass conservation) for each component, which in particular means it will satisfy

$$v_i = \frac{[F_k]}{[u_k]}; k = 1,....,n-1 \quad , \tag{1.5}$$

where [-] represents a jump from one side of the shock to the other. In our notation, the actual propagation velocity of a wave ν_i is $V_i = \frac{U_T}{\phi}\nu_i$. If $\frac{U_T}{\phi}\nu_i ; i = 1,....,N$ represents the solution of the constant flux Riemann problem connecting $\boldsymbol{u}^L, \boldsymbol{u}^R$, the solution of the constant pressure boundary solution is represented by $\frac{U_T(t)}{\phi}\nu_i ; i = 1,....,N$.

In brief, this paper assumes we know the solution (unique or not) of a multi-component Riemann problem subject to the assumption of constant volumetric flux U_T. The main result of the paper is to determine the function $U_T(t)$ for the case of constant pressure boundaries for the same Riemann problem.

Following the construction of $U_T(t)$ *we also obtain closed form expressions for the time when a particular wave breaks through at the outlet end. Furthermore, we determine the pressure distribution* $p(x,t)$ *at any time t in* $0 \le x \le L$.

In addition to being useful in interpretation of core flood experiments with constant pressure boundaries, the generalization in this paper also offers new applications in numerical simulation. For example, streamline simulation is frequently used by the oil industry to compute fluid flow in reservoirs between injectors and producers (Bratvedt et al., 1996; Thiele et al., 2010). In such simulations, the pressure distribution is first solved from an elliptic equation subject to simplifying assumptions. Subsequently, streamlines are generated from the pressures and finally, the fluid flow between injectors and producers can be calculated analytically along streamlines, provided that the Riemann problem at hand has a known solution. The popularity of this approach is primarily because of considerable time savings compared to conventional simulations. Previously, streamline simulations using solutions of Riemann problems along streamlines could only be performed for cases of constant flow rates. A more common way to operate wells is by keeping flowing wellbore pressures constant. The solutions derived in this paper therefore widen the applicability of streamline simulation.

Riemann problem solutions can also be used as building blocks for the construction of numerical methods which can be used with general boundary conditions. Examples of this are the Random Choice Method, Chorin (1976), Concus, Proskurowski (1979), Glimm (1965) and Godunov's Method, Godunov (1959).

Global solutions for many hyperbolic Riemann problems have yet to be found. A general theory for local existence and uniqueness of solutions of Riemann problems is described in Glimm, (1959), Lax (1957) and Smoller (1982) under the condition of strict hyperbolicity (distinct eigenvalues of the Jacobian A). However, flow phenomena in porous media are typically not strictly hyperbolic. The most well-known Riemann problem pertinent to the oil industry is the Buckley-Leverett theory for water injection in an oil reservoir, Buckley, Leverett (1941), and also Welge (1952). It is a single hyperbolic equation modeling conservation of water, the conservation of the oil being taken care of through the assumption of constant volumetric flux U_T both in space and time. The generalization of this theory to constant pressure boundaries is described in Section 2 of this paper.

The first non-strictly hyperbolic multi component problem appearing in the literature with a complete global solution seems to be for single phase (water) flow with dissolved components that adsorb on the rock in a non-linear and coupled fashion, Rhee et al. (1970). The adsorption causes a chromatographic separation of the individual components.

A global solution of a non-strictly hyperbolic system modeling polymer flooding with non-linear adsorption was presented in Johansen and Winther (1988). Here, the water phase contains dissolved polymer for the purpose of increasing the water viscosity to enhance sweep efficiency. Again, this was for constant volumetric flux in space and time. An example using this solution with constant pressure boundaries is presented in Section 3 of this paper.

A system with multiple adsorbing polymer components with decoupled adsorption was presented in Johansen and Winther (1989). This was generalized to a coupled adsorption model in Dahl et al. (1992). A system describing four

component, two phase flow with components partitioning between the two phases was analyzed in Johansen et al. (2005) and Wang et al. (2005). A comprehensive discussion and analysis of this is also presented in Orr (2007).

In all of the above citations, the assumption of constant U_T in space and time is essential. The theory presented in this paper therefore generalizes the results of the above citations.

Three cases are used in Section 3 to demonstrate the constant pressure boundary multicomponent extension of Riemann problem solutions; case 1a) waterflooding with viscosity ratio $\mu_o/\mu_w = 0.2$, case 1b) waterflooding with $\mu_o/\mu_w = 20$ and case 2) polymer flooding with a single polymer component residing in the aqueous phase. This constant pressure multicomponent extension is particularly important as many actual oil fields are operated under constant wellbore pressures, and being a generalised analytical solution, it can be readily adapted and used for better predicting production rates.

2. The Algorithm for determination of the volumetric flux $U_T(t)$ for constant pressure boundaries

We will without ambiguity, since eigenvalues (λ) do not appear directly in this section, let $\lambda_T = K\sum_{j=1}^{2}(k_{rj}/\mu_j)$ denote total mobility, where K is permeability, k_{rj} phase relative permeability and μ_j phase viscosity. We assume, in this section, constant pressure boundaries; $p_{in} = p(0,t)$; $p_{out} = p(L,t)$. Satisfying mass conservation and the assumption of constant flow rate, U_T is constant as a function of x but not t. We obtain using Darcy's law

$$U_T = -\lambda_T \frac{\partial p}{\partial x} \Rightarrow \Delta p = U_T \int_0^L \frac{dx}{\lambda_T} \quad ; \Delta p = p_{in} - p_{out} \quad . \tag{2.1}$$

Let $t_{BT,i}$ be the time when the leading edge of a wave ν_i is breaking through at the outlet end $x = L$.

2.1. The Case $t \le t_{BT,N}$

We first derive explicit expressions for the velocity, $U_T(t)$, before the fastest wave breaks through at the outlet end, and the time when this breakthrough occurs, $t_{BT,N}$. Letting $\Psi(t) = \int_0^t U_T(\tau)d\tau$ and using $x = \int_0^t V_i(t)dt = \int_0^t \frac{U_T}{\phi}\nu_i dt$, we first consider the pressure drop over a rarefaction wave ν_i and change integration variable using $dx(s) = \frac{\Psi(t)}{\phi}\frac{\nu'(s)}{\lambda_T(s)}ds$:

$$U_T \int_{y_i}^{x_i} \frac{dx}{\lambda_T} = U_T \frac{\Psi(t)}{\phi} \int_{s_{i-1}}^{s_i} \frac{\nu'}{\lambda_T} ds \quad . \tag{2.2}$$

Obviously, if the wave is a shock, this integral is zero since. We, therefore, define

$$\int_{s_{i-1}}^{s_i} \frac{\nu_i'}{\lambda_T} ds \begin{cases} 0 & \text{if wave } i \text{ is a shock} \\ \int_{s_{i-1}}^{s_i} \frac{\nu_i'}{\lambda_T} ds & \text{if wave } i \text{ is a rarefaction} \end{cases} . \tag{2.3}$$

We can now write equation (2.1) as

$$\Delta p = U_T \left[\sum_{i=1}^{N} \left[\frac{y_i - x_{i-1}}{\lambda_T(s_{i-1})} + \frac{\Psi(t)}{\phi} \right]_i + \frac{L - x_N}{\lambda_T(s^R)} \right] \tag{2.4}$$

where the first term on the right hand side covers integration over the constant states, except the part corresponding to the constant initial state (s^R), which is covered by the third term. Given the leading edge of the wave, x_i and the trailing edge, y_i, we can relate the velocity of the leading edge (dx/dt) and the velocity of the trailing edge of the shock (dy/dt) to the propagation velocity of the wave, $V(s)$:

$$\frac{dy_i}{dt} = V_i(s_{i-1}) \quad ; \frac{dx_{i-1}}{dt} = V_{i-1}(s_{i-1}) \quad ; i = 1,....N-1 \quad . \tag{2.5}$$

If we define constants, $\beta_i = \frac{\nu_i(s_{i-1})}{\nu_N(s^R)}$; $\alpha_i = \frac{\nu_i(s_i)}{\nu_N(s^R)}$, equation (2.5) implies that

$$\frac{dy_i}{dx_N} = \beta_i \quad ; \frac{dx_{i-1}}{dx_N} = \alpha_{i-1} \quad ; i = 1,...., N-1 \quad ; \quad \alpha_0 = 0 \quad . \tag{2.6}$$

Since $x_N = y_i = x_i = 0$ at $t = 0$,

$$y_i = \beta_i x_N \quad ; \quad x_{i-1} = \alpha_{i-1} x_N \quad . \tag{2.7}$$

Hence,

$$\frac{y_i - x_{i-1}}{\lambda_T(s_{i-1})} = r_i x_N \; ; \; r_i = \frac{\beta_i - \alpha_{i-1}}{\lambda_T(s_{i-1})} \quad . \tag{2.8}$$

Substituting this into equation (2.4), we obtain

$$\Delta p = U_T \left[\sum_{i=1}^{N} r_i \cdot x_N + \frac{\Psi(t)}{\phi} \sum_{i=1}^{N} \boldsymbol{\vartheta}_i + \frac{L - x_N}{\lambda_T(s^R)} \right] \quad . \tag{2.9}$$

The position of the leading edge of the wave is given by $x_N = \frac{\Psi(t)}{\phi} \nu_N(s^R)$. The pressure difference is therefore

$$\Delta p = U_T \left[A x_N + B \right] \quad , \tag{2.10}$$

where

$$A = \sum_{i=1}^{N} r_i + \frac{1}{\nu_N(s^R)} \sum_{i=1}^{N} \boldsymbol{\vartheta}_i - \frac{1}{\lambda_T(s^R)} \quad ; \quad B = \frac{L}{\lambda_T(s^R)} \quad . \tag{2.11}$$

Using equation (2.10), the velocity of the leading edge of the wave becomes

$$\frac{dx_N}{dt} = \frac{U_T}{\phi} \nu_N(s^R) = \frac{\Delta p \nu_N(s^R)}{\phi(A x_N + B)} \quad . \tag{2.12}$$

Integration of the separable ordinary differential equation (2.12) gives

$$Ax_N^2 + 2Bx_N = Ct \quad , \tag{2.13}$$

where

$$C = 2\Delta p \nu_N(s^R)/\phi \quad . \tag{2.14}$$

Accepting only the positive root in equation (2.13), the location of the leading edge of the fastest wave is given by

$$x_N(t) = \frac{-B + \sqrt{B^2 + 4ACt}}{A} \quad . \tag{2.15}$$

We can now determine $U_T(t)$ *explicitly from* (2.10):

$$U_T(t) = \frac{\Delta p}{\sqrt{B^2 + 4ACt}} \quad . \tag{2.16}$$

By substituting $x_N = L$ in equation (2.13) *we find an explicit expression for the break through time of wave* ν_N :

$$t_{BT,N} = \frac{AL^2 + 2BL}{C} \quad . \tag{2.17}$$

Finally, the pressure at the leading edge of the fastest wave, before this wave breaks through at time $t_{BT,N}$ is calculated as

$$p_N(t) = p_{out} + U_T \int_{s_{N-1}}^{s^R} \frac{ds}{\lambda_T(s)} = p_{out} + \frac{U_T}{\lambda_T(s^R)}(L - x_N(t)) \quad . \tag{2.18}$$

The pressure at any location can then be calculated backwards (from outlet *towards the inlet*) *using equation* (2.9).

The above applies to $t \le t_{BT,N}$ i.e. before the break through of the leading wave. We next describe how $U_T(t)$ is calculated for $t_{BT,N} < t \le t_{BT,N-1}$, i.e. after the break through of the leading wave.

2.2. The Case $t_{BT,N} \le t \le t_{BT,N-1}$

If the fastest wave is a shock ν_N with a constant saturation state, s_{N-1}, separating ν_{N-1} from ν_N, the velocity, $U_T(t)$, for $t_{BT,N} < t \le t_{BT,N-1}$ is calculated exactly as in section 2.1, simply by removing ν_N and putting $s^R = s_{N-1}$. This is because we already know $\Psi(t)$ for $t \le t_{BT,N}$. If the first wave is a rarefaction, the calculation of $U_T(t)$ is as described below.

Let s between $s_N = s^R$ and s_{N-1} be arbitrary but fixed. Let $x(s, t_{BT,N})$ be the location of s at time $t_{BT,N}$, i.e. the time when ν_N breaks through with its leading edge at $x = L$. Also, let t_s be the time when s arrives at $x = L$. This is illustrated in Figure 2.

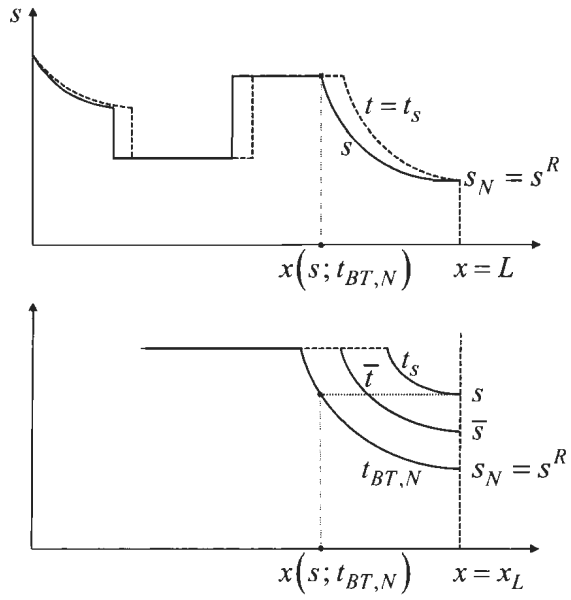

Fig. 2 Example of a Rarefaction Wave at Breakthrough

Let $\bar{t}$ be a time between $t_{BT,N}$ and t_s, and let $\bar{s}$ be the value of s at $x = L$ at $t = \bar{t}$. For $t \le \bar{t}$,

$$x(s;\bar{t}) = \frac{\nu_N(s)}{\phi}\Psi(\bar{t}) \tag{2.19}$$

and

$$\Delta p = U_T(\bar{t})\left[\sum_{i=1}^{N}\frac{y_i - x_{i-1}}{\lambda_T(s_{i-1})} + \frac{\Psi(\bar{t})}{\phi}\sum_{i=1}^{N-1}\frac{\Psi(\bar{t})}{\phi}\int_{s_{N-1}}^{\bar{s}}\frac{\nu'_N(s)ds}{\lambda_T(s)}\right] \tag{2.20}$$

giving

$$U_T(\bar{t}) = \frac{\Delta p}{\sum_{i=1}^{N}\frac{y_i - x_{i-1}}{\lambda_T(s_{i-1})} + \frac{x(s,\bar{t})}{\nu_N(s)}\left[\sum_{i=1}^{N-1}\frac{\Psi(\bar{t})}{\phi}\int_{s_{N-1}}^{\bar{s}}\frac{\nu'_{N-1}(s)ds}{\lambda_T(s)}\right]} \tag{2.21}$$

or

$$U_T(\bar{t}) = \frac{\Delta p}{x(s,\bar{t})\left\{\sum_{i=1}^{N} r_i + \frac{1}{\nu_N(s)}\left[\sum_{i=1}^{N-1}\frac{\Psi(\bar{t})}{\phi}\int_{s_{N-1}}^{\bar{s}}\frac{\nu'_N(s)ds}{\lambda_T(s)}\right]\right\}}, \tag{2.22}$$

where r_i is given by equation (2.8). We also have

$$\frac{dx(\bar{s},\bar{t})}{dt} = U_T(\bar{t})\frac{\nu_N(s)}{\phi} \quad . \tag{2.23}$$

Combining equation (2.22) with equation (2.23), we get

$$x(s,\bar{t})\frac{dx}{dt} = \frac{\Delta p \nu_N(s)}{\phi\left\{\sum_{i=1}^{N} r_i + \frac{1}{\nu_N(s)}\left[\sum_{i=1}^{N-1}\frac{\Psi(\bar{t})}{\phi}\int_{s_{N-1}}^{\hat{s}}\frac{\nu'_N(s)ds}{\lambda_T(s)}\right]\right\}} \tag{2.24}$$

which, when integrated between $t_{BT,N}$ and $\bar{t}$ letting $\bar{t} \to t_s$ can be written as

$$\phi\left[x(s,t_{BT,N})^2 - L^2\right] = \frac{2\Delta p \nu_N(s)^2\left[t_S - t_{BT,N}\right]}{\sum_{i=1}^{N} r_i \cdot \nu_N(s) + \sum_{i=1}^{N-1}\frac{\Psi(\bar{t})}{\phi}\int_{s_{N-1}}^{\hat{s}}\frac{\nu'_N(s)ds}{\lambda_T(s)}} \quad . \tag{2.25}$$

Here, $t_{BT,N}$ is known from equation (2.17) and

$$x(s,t_{BT,N}) = \frac{v_N(s)}{\phi}\Psi(t_{BT,N}) \quad . \tag{2.26}$$

Hence, t_s can be calculated from

$$t_s = t_{BT,N} + \frac{\phi\left[x(s,t_{BT,N})^2 - L^2\right]}{2\Delta p v_N(s)^2}\left\{\sum_{i=1}^{N} r_i \cdot v_N(s) + \sum_{i=1}^{N-1} \mathcal{I}_i + \int_{s_{N-1}}^{s} \frac{v_N'(s)ds}{\lambda_T(s)}\right\} \quad . \tag{2.27}$$

The corresponding value for $U_T(t_S)$ *is given by*

$$U_T(t_s) = \frac{\phi[x(s,t_{BT,N})^2 - L^2]}{2Lv_N(s)(t_s - t_{BT,N})} \tag{2.28}$$

for $t_s > t_{BT,N}$. For $t = t_{BT,N}$ it is easy to see that U_T in equation (2.28) approaches the value of U_T given by equation (2.9), i.e. U_T is continuous , however, not differentiable at $t = t_{BT,N}$.

The procedure then can be summarized as follows: *We can calculate the time* t_S *when* s *breaks through at* $x = L$ *from equation* (2.27) *for any* s *on the rarefaction wave* v_N. *Once this time is known, the corresponding value of* $U_T(t_s)$ *is given by equation* (2.28).

2.3. The Case $t > t_{BT,N-1}$

When the entire leading wave v_N has passed $x = L$, as described in sections 2.1 and 2.2, the procedure can be repeated by removing v_N from the wave train and starting over again with $s_R = s_{N-1}$. The computational procedure is, therefore, complete for the case when Δp is fixed.

The special case when U_T is constant in both x and t (as the solution for constant flux in both x and t) can be treated by using

$$x_N = \frac{U_T}{\phi} \nu_N(s^R) t \tag{2.29}$$

in equation (2.10), i.e.

$$\Delta p(t) = U_T[A^* t + B]; A^* = A\frac{U_T}{\phi}\nu_N(s^R) \quad . \tag{2.30}$$

Equation (2.16) reduces to

$$U_T = \lambda_T \frac{\Delta p(0)}{L} \quad . \tag{2.31}$$

The procedure for calculating $\Delta p(t)$ for the other cases is straightforward.

2.4. Generalisation

The above derivation for a fixed Δp can easily be generalized to the situation where $\Delta p(t)$ is given as a function of time. Denoting

$$D(t) = \int_0^t \Delta p(\tau) d\tau \quad , \tag{2.32}$$

it is easily seen that (as in section 2.2)

$$x_N(t) = \frac{-B + \sqrt{B^2 + 4ACD(t)}}{A} \tag{2.33}$$

and

$$U_T(t) = \frac{\Delta p(t)}{Ax_N(t) + B} \quad . \tag{2.34}$$

The time to break through of $\nu_N(S_R)$ is then found from

$$D(t_{BT,N}) = \frac{AL^2 + 2BL}{C} \tag{2.35}$$

and similarly for the other cases.

3. Constant Pressure Boundary Case Studies

In the oil industry, The Buckley-Leverett solution (1941) is synonymous with fractional flow theory where an immiscible fluid displaces another in one-dimensional flow in a porous medium. Physically, fractional flow theory describes the linear displacement of one phase by another immiscible phase where there is a front described by a shock or sudden change in concentration. In its simplest form it describes one component displacing another immiscible component in one dimension in the absence of diffusive and compressible flow, i.e. water displacing oil (Buckley and Leverett, (1941), Welge (1952)). Mathematically, the Buckley-Leverett equation is a first order hyperbolic partial differential conservation equation in time and space. The solution is composed of a leading shock and a trailing rarefaction wave.

Two case studies are developed in this section illustrating the use and effectiveness of the generalized constant pressure fixed boundary Riemann problem. The first illustration is a simple waterflooding case where in a) the viscosity of the water is greater than that of oil, with $\mu_o/\mu_w = 0.2$ and in b) the oil viscosity is greater than the water viscosity with $\mu_o/\mu_w = 20$. The second case is a polymer flooding case where the viscosity of the water phase is linearly dependent on the concentration of polymer added. The parameters used in the case studies are outlined in the Table 1. The core is one meter long with 18% porosity and a permeability of one Darcy. There is a $\Delta p =$ 500 *psi* (34.1 *MPa*) pressure drop across the core that is initially at 25% water saturation as connate water $s^R = s_{wc} = 0.25$ and 75% oil saturation. The displacing water saturates to 70%

leaving 30% residual oil saturation ($s^L = 1 - s_{or} = 0.7$). We use normalized saturations, i.e.

$$s = \frac{s_w - s_{wc}}{1 - s_{or} - s_{wc}} \quad . \tag{3.1}$$

Table 1 Parameters Used in the Constant Pressure Boundary Cases

Parameter	Waterflooding		Polymer Flooding
	Case 1a	Case 1b	Case 2
	$\mu_w >> \mu_o$	$\mu_w << \mu_o$	$\mu_w^0 = 1$
μ_w (cP)	10	1	$\mu_w(c) = \mu_w^o + 200c$
μ_o (cP)	2	20	8
μ_o/μ_w	0.2	20	
ϕ	0.18		
L (m)	1		
p_{in} (MPa)	21.0		
p_{out} (MPa)	17.0		
s_{or}	0.30		
s_{wc}	0.25		
K (m^2)	1 x 10^{-12}		
k_{ro}	$k_{ro} = 0.8\left(\frac{1 - s_w - s_{or}}{1 - s_{wc} - s_{or}}\right)^2 = a_o(1-s)^2$		
k_{rw}	$k_{rw} = 0.2\left(\frac{s_w - s_{wc}}{1 - s_{wc} - s_{or}}\right)^2 = a_w s^2$		

3.1. Waterflooding

In case 1a) a more viscous water displaces a less viscous oil. In case 1b) a less viscous water displaces a more viscous oil. The viscosity ratio of oil to water varies a factor 100 between the two cases.

The Riemann problem is

$$\frac{\partial s}{\partial t} + \frac{U_T}{\phi}\frac{\partial f(s)}{\partial x} = 0 \tag{3.2}$$

$$s^L = 1 - s_{or} = 0.7 \tag{3.3}$$

$$s^R = s_{wc} = 0.25 \quad . \tag{3.4}$$

The fractional flow of a phase is defined from the mobility of the phase (λ) with respect to the total mobility as:

$$f(s) = \frac{\lambda_w}{\lambda_o + \lambda_w} \tag{3.5}$$

where phase mobility is

$$\lambda = \frac{Kk_r}{\mu} \quad , \tag{3.6}$$

where k_r is relative permeability (see Table 1). We use the illustration in Figure 3 to depict the two waves (N=2) constituting the solution, in accordance with Figure 1. Here, ν_1 is a rarefaction wave and ν_2 is a shock wave.

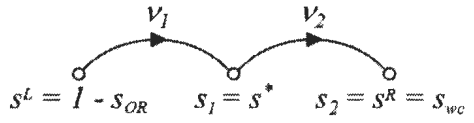

Fig. 3 Depiction of a Two Wave Riemann Problem

The intermediate state $s^* = 0.69$ is calculated by constructing the tangent from the point $(s^R, 0)$ to the graph of f, Figure a). The propagation velocities are denoted V_1 and V_2, respectively. The rarefaction wave is from $(s^L, 1)$ to $(s^*, f(s^*))$. The shock wave is a jump from $(s^*, f(s^*))$ to $(s^R, 0)$.

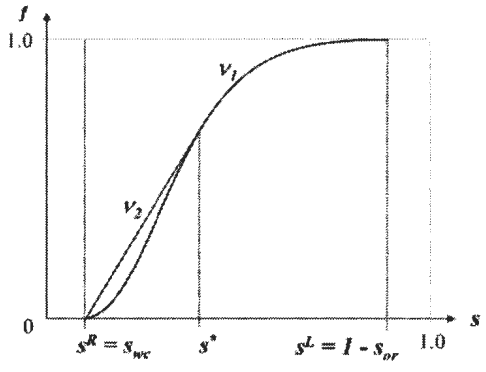

Fig. 4 The Intermediate Saturation (s^*) is determined from the tangent of the fractional flow curve

Table 2 Wave Descriptions

Wave			Propagation Velocity	
Rarefaction	$v_1 = f'(s)$	(3.7)	$V_1 = \frac{U_T}{\phi} v_1$	(3.8)
Shock	$v_2 = \frac{f(s^*) - f(s^R)}{s^* - s^R}$	(3.9)	$V_2 = \frac{U_T}{\phi} v_2$	(3.10)

The function $F = U_T(t) f / \phi$ is shown in Figure 5.

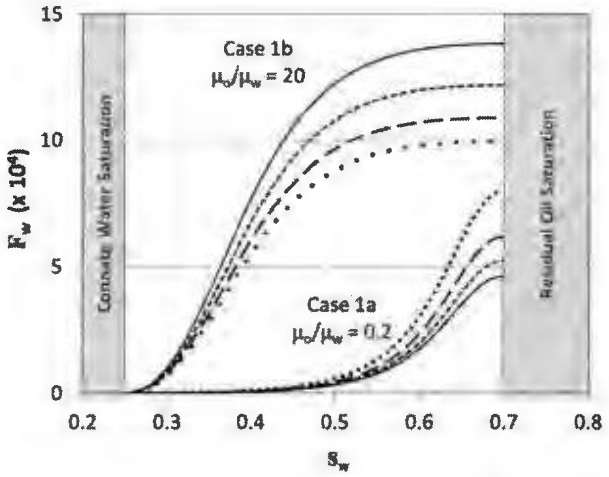

Fig. 5 Fractional Flow Functions for the Waterflooding Cases 1a) $\mu_o/\mu_w = 0.2$ and 1b) $\mu_o/\mu_w = 20$ at 0.3 (·····), 0.5 (— —), 0.7 (- - - - -), and 0.9 (——) of the breakthrough time

Using the data given above, we get from (2.3)

$$1 = \int_{s_o}^{s^*} \frac{f''(s)}{\lambda_T(s)} ds = 1.1760 \times 10^{11} \; Pa \cdot s/m^2, \tag{3.11}$$

$$_2 = 0 \; , \tag{3.12}$$

and from (2.8)

$$r_1 + r_2 = \frac{\beta_1 - \alpha_o}{\lambda_T(s_o)} + \frac{\beta_1 - \alpha_1}{\lambda_T(s_1)} = \frac{v_1(s_o)}{\lambda_T(s_o)} + \frac{v_2 - v_2}{\lambda_T(s_o)} = 0 \quad . \tag{3.13}$$

Therefore,

$$C = \frac{2\Delta p}{\phi} v_2 = 1.02 x 10^8 \; Pa \quad ; \quad \Delta p = 34.1 \; MPa \tag{3.14}$$

$$B = \frac{L}{\lambda_T(s_R)} = 2.50x10^9\, Pa \cdot s / m \tag{3.15}$$

$$A = \frac{1}{v_2}\mathbf{\mathcal{J}}_1 - \frac{1}{\lambda_T(s^R)} = 4.86x10^{10}\, Pa \cdot s / m^2 \quad . \tag{3.16}$$

The corresponding water saturation profiles are shown in Figure 6. The high water saturation s^* for case 1a is physically realistic where a much lower mobility ratio (dominated by μ_o/μ_w) will result in better sweep efficiency, i.e. higher water saturation behind the flood front.

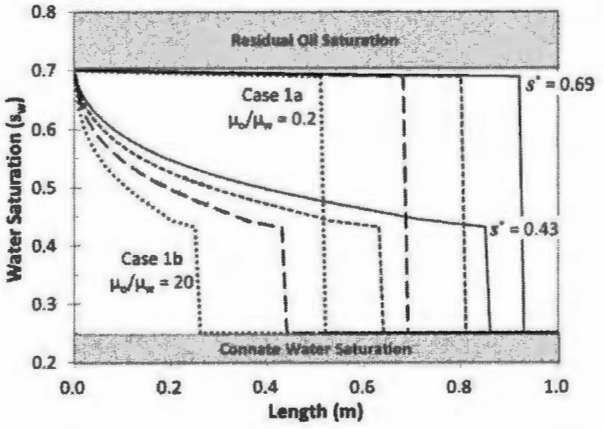

Fig. 6 Saturation Profiles for the Waterflooding Cases 1a) $\mu_o/\mu_w = 0.2$ and 1b) $\mu_o/\mu_w = 20$ at 0.3 (·····), 0.5 (— —), 0.7 (- - - - -), and 0.9 (——) of the Breakthrough Time

The time to breakthrough of the shock is determined from equation (2.17). In the mobility controlled case 1a, the break through time is 523 s whereas it is only 228 s for the mobility unstable case 1b where the water (displacing) viscosity is much less than the oil viscosity (displaced).

For any given $s > s^*, t > t_{BT}$ (rarefaction wave, post shock breakthrough), $U_T(t)$ is calculated from (2.27), (2.28) which become, respectively,

$$t_s - t_{BT} = \frac{\phi\left[x(s,t_{BT})^2 - L^2\right]}{2\Delta p v_2^2} \int_{s^*}^{s} \frac{f''(s)ds}{\lambda_T(s)} \quad , \tag{3.17}$$

$$U_T(t_s) = \frac{\phi\left[x(s,t_{BT})^2 - L^2\right]}{2f'(s)(t_s - t_{BT})} \quad . \tag{3.18}$$

The total volumetric flux as functions of time are shown for both waterflooding cases in Figure 7. The following explanation also makes reference to the water saturation profiles depicted in Figure 6. The total velocity decreases non-linearly for case 1a as expected due to the increasing amount of water with high viscosity in the porous medium. After breakthrough, the total velocity is almost constant owing to the uniform 70% water saturation. The opposite is observed for case 1b where the much lower viscosity displacing water saturates less pore volume at breakthrough. As the amount of low viscosity water continues to increase after breakthrough so does the total velocity.

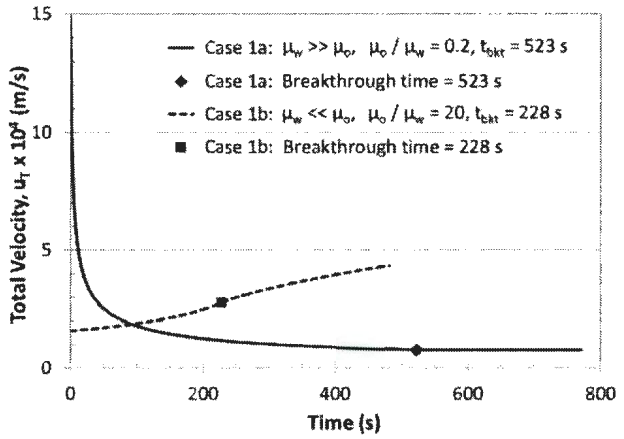

Fig. 7 Total Velocities for Waterflooding Cases 1a) $\mu_o/\mu_w = 0.2$ (——) & 1b) $\mu_o/\mu_w = 20$ (- - -)

Figure 7 also shows that the variation in velocity is very significant and nonlinear, thereby completely ruling out the use of classical fractional flow theory for constant pressure boundaries.

The front position at any given $t < t_{BT}$ is calculated from (2.15) and shown as a function of time in Figure 8 for both waterflooding cases.

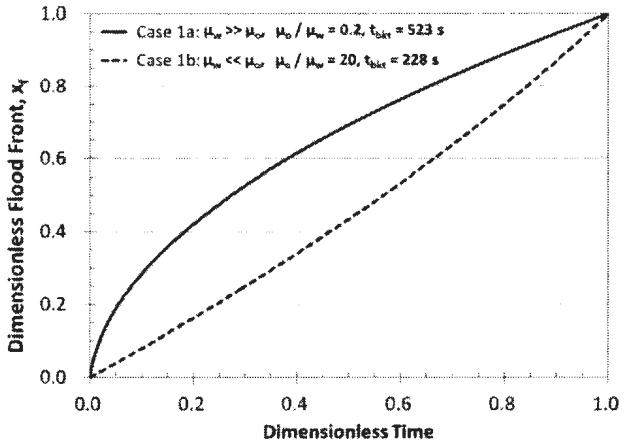

Fig. 8 Position of the Flood Front (Shock Wave) Before Breakthrough for Waterflooding Cases 1a) $\mu_o/\mu_w = 0.2$ (——) and 1b) $\mu_o/\mu_w = 20$ (- - - - -)

3.2. Polymer Flooding

The polymer flooding case demonstrates the constant pressure boundary solution for multi-component systems. Physically, polymer may be added to the water to increase its viscosity to overcome an adverse mobility ratio. The parameters used for the polymer case are shown in Table 1.

If c is polymer concentration in the aqueous phase, we use a linear dependence of aqueous phase viscosity on polymer concentration,

$$\mu_w(c) = \mu_w^o + 200c \tag{3.19}$$

which, with the data in Table 1, gives

$$f(s,c) = \frac{s^2}{s^2 + (0.5+100c)(1-s)^2} \quad . \tag{3.20}$$

An adsorption isotherm of the form shown in Figure 9 and given by eqtn. (3.21) is used,

$$a(c) = \frac{0.2c}{1+100c} \quad . \tag{3.21}$$

The Riemann problem is

$$\phi \frac{\partial s}{\partial t} + U_T(t) \frac{\partial f(s,c)}{\partial x} = 0 \quad , \tag{3.22}$$

$$\phi \frac{\partial}{\partial t}[sc + a(c)] + U_T(t) \frac{\partial [f(s,c)c]}{\partial x} = 0 \quad , \tag{3.23}$$

$$\begin{aligned} s^L &= s_0 = 0.7 \quad ; \quad s^R = 0.25 \\ c^L &= 0.01 \quad ; \quad c^R = 0.0 \quad . \end{aligned} \tag{3.24}$$

This Riemann problem was analysed by Johansen and Winther (1988). The solution is composed of three waves. The slowest wave is a rarefaction (ν_1) corresponding to the eigenvalue $\partial f / \partial s$. The middle wave (ν_2) is a shock corresponding to the eigenvalue $f/(s + a'(c))$ and the fastest wave is a shock (ν_3) corresponding to the eigenvalue $\partial f / \partial s$. This wave train is shown in Figure 9.

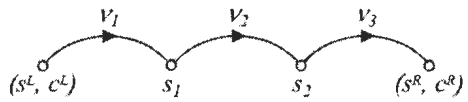

Fig. 9 Wave Train of Three Waves of Varying Velocity

The waves are separated by two constant states $s_1 = 0.693$ and $s_2 = 0.514$. Denoting

$$h_{LR} = \frac{a(c_R) - a(c_L)}{c_R - c_L} = 0.1 \quad , \tag{3.25}$$

the wave descriptions are summarized in Table 3 and refer to Figure10.

Table 3 Wave Descriptions, Polymer Case.

Wave		Propagation Velocity
Rarefaction	$\nu_1 = \partial f(s,c)/\partial s$	$V_1 = \frac{U_T}{\phi}\nu_1$
Shock	$\nu_2 = \frac{f(s_1,c^L)}{s_1 + h_{LR}} = 1.01$	$V_2 = \frac{U_T}{\phi}\nu_2$
Shock	$\nu_3 = \frac{f(s_2,c^R) - f(s^R,c^R)}{s_2 - s^R} = 1.37$	$V_3 = \frac{U_T}{\phi}\nu_3$

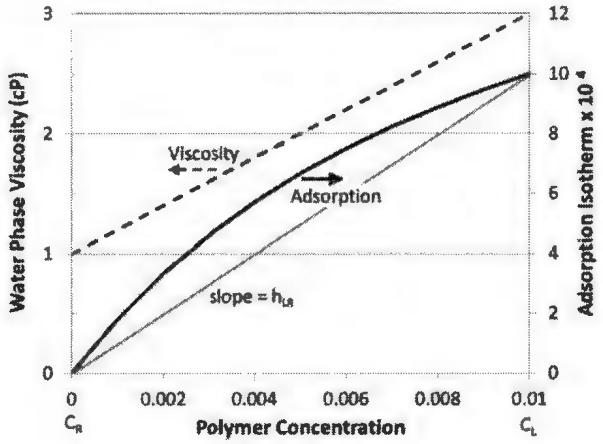

Fig. 10 Water Phase Viscosity (---) and Adsorption Isotherm (——) as a Function of Polymer Concentration

The construction of the solution is shown in Figure 11: Starting at $(s^L,1)$, the rarefaction wave ends where the tangent to the graph of $f(\bullet,c^L)$ passes through the point $(-h_{LR},0)$. This point of tangency defines s_1. From this point, the shock ν_2 jumps to the graph of $f(\bullet,c^R)$ with a velocity equal to the tangent slope. This point on $f(\bullet,c^R)$ defines s_2. The shock ν_3 is similar to the shock in the Buckley-Leverett case, joining the two points $(s_2,f(s_2,c^R))$ and $(s_R,f(s_R,c^R))$.

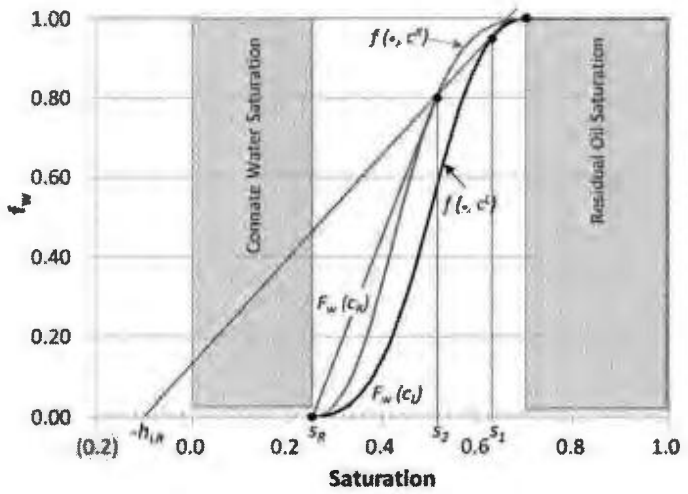

Fig. 11 Fractional Flow Function for the Polymer Case

The saturation profiles composed of the three waves are shown in Figure 12.

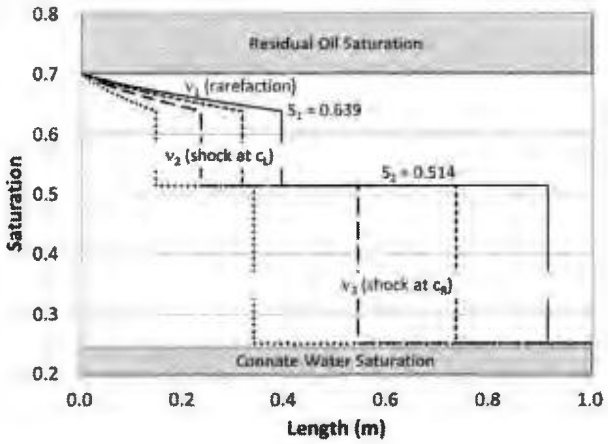

Fig. 12 Saturation Profiles for the Polymer Case 2) at 0.3 (·····), 0.5 (— —), 0.7 (- - - - -), and 0.9 (——) of the Breakthrough Time

Comparing the right and left fractional flow curves and the slope of the tangents in Figure 11, we see that the right shock is travelling more quickly than the left shock, i.e. the pure water-oil shock is advancing through the porous media faster than the increased viscosity polymer water. This is confirmed when compared to the initial higher total flux shown in Figure 13 that decreases as the water-oil interface advances through the porous media. Both, shock wave v_3 and shock wave v_2 decelerate as they move through the porous medium (Figure 11) as does the total flux (Figure 13).

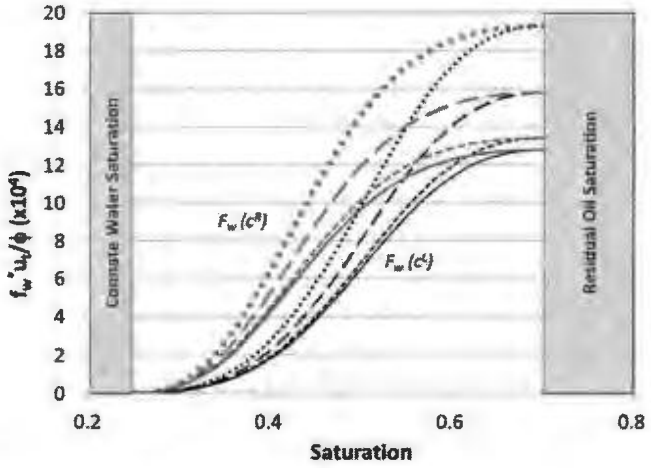

Fig. 13 Fractional Flow Functions for the Polymer Case 2) at Saturation Profiles for the Polymer Case 2) at 0.3 (·····), 0.5 (— —), 0.7 (- - - - -), and 0.9 (——) of the Breakthrough Time for $c^L = 0.01$ (black) and $c^R = 0$ (grey)

The integrals in (2.3) are $\mathcal{I}_2 = \mathcal{I}_3 = 0$ since waves 2 and 3 are shocks, and

$$\mathcal{I}_1 = \int_{s^L}^{s_1} \frac{\partial^2 f(s,c^L)/\partial s^2}{\lambda_T(s,c^L)} ds = 2.27 \times 10^{10}\, Pa \cdot s/m^2 \quad .$$

For the coefficients A, B, C in (2.11), (2.14) we find

$$\begin{aligned} A &= (1-\frac{\nu_3}{\nu_2})\frac{1}{\lambda_T(s_2,c^L)} + \frac{1}{\nu_3}\mathcal{I}_1 - \frac{1}{\lambda_T(s^R,c^R)} \\ B &= \frac{L}{\lambda_T(s^R,c^R)} \\ C &= 2\Delta p \nu_3/\phi \quad , \end{aligned} \tag{3.26}$$

where the values for the two shock after their respective breakthrough are shown in Table 4.

Table 4 Integration Coefficients for the Two Polymer Cases

Integration Coefficient	After First Shock Breakthrough	After Second Shock Breakthrough
A	4.11 x 10^9	5.75 x 10^9
B	1.0 x 10^{10}	1.16 x 10^{10}
C	1.35 x 10^8	5.80 x 10^7

The time to breakthrough of the first shock is then determined by (2.17). It is found to be 179 s and the position of the front as a function of time is shown in Figure 14. The shock position at any time before breakthrough of the first shock is given by (2.15), and we then determine $U_T(t)$ before breakthrough by (2.16).

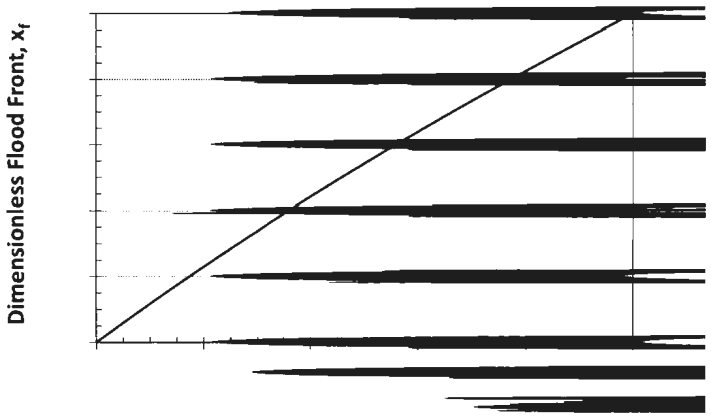

Fig. 14 Position of the Flood Front (Shock Wave ν_3) before Breakthrough for the Polymer Case 2

After v_3 has broken through at $x = L$ the procedure is identical to the waterflood cases with $c = const. = c^L$ (since v_3 then is gone) and therefore a description here is redundant.

A numerical simulation of the polymer case was also carried out using a first order upstream method with implicit treatment of pressure and explicit treatment of saturation. Figure 15 shows the variation in numerical versus analytically computed total volumetric flux results. The simulations were performed with 20, 50, and 200 grid blocks As Fig. 15 indicates, a reasonable resolution of U_T (t) is obtained using 200 grid blocks but it requires 4x the calculation time. Of course, the difference being that the numerical method needed to calculate the pressure and saturation at every time step up to breakthrough unlike the analytical solution which can calculate the time to breakthrough directly.

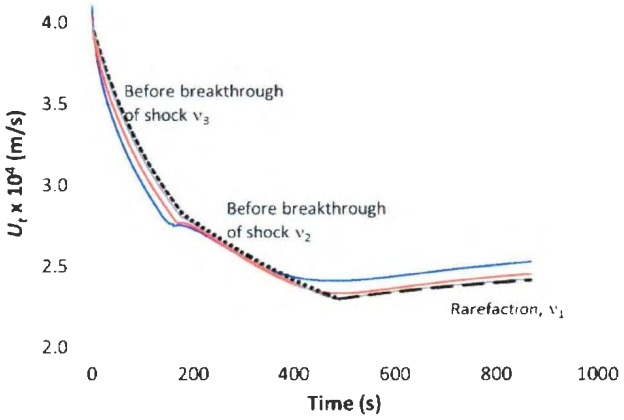

Fig. 15 Total Volumetric Flux: Before v_3 the Pure Water-Oil Shock (- - -); Before v_2 the Polymer-Oil Shock (• • • •); and After v_2 the Polymer-Water Rarefaction (— —) including the Numerical Solutions for 20 (blue: ——), 50 (red: ——), and 200 (grey:) Grid Blocks

The pressure profile from injection to production end at any time before v_3 has broken through was also calculated analytically using (2.18). Figure 16 shows the pressure profile for 0.3, 0.5 and 0.9 of the breakthrough time for wave v_3. As expected, the pressure profile changes at the shock front as it progresses through the porous medium. This type of calculation can be of great importance in miscible tending gas injection processes, since the phase behaviour at the

displacement front controls the residual oil saturation. Such gas injection processes can also be modeled at constant pressure boundaries through the results presented in this paper.

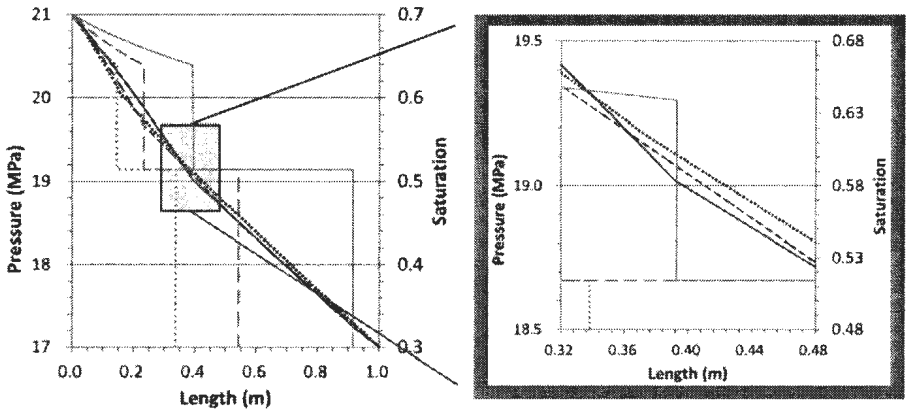

Fig. 16 Pressure Profiles for the Polymer Case 2 (including Saturation Profiles for Reference) at 0.3 (·····), 0.5 (— —), and 0.9 (——) of the Breakthrough Times of Wave v_3

4. Conclusions

Existing solutions to global Riemann problems with constant volumetric flux have been extended to constant pressure boundaries with variable flux. The derivation mathematically describes the explicit behaviour before the first wave breaks through, between waves and post breakthrough of the trailing rarefaction waves. Expressions for the position of any state in any wave, the overall flux and time for that specific wave to break through are also derived. The pressure distribution between inlet and outlet ends at any time is also calculated analytically. The application of the constant pressure boundary solution is illustrated with three examples to fully explore the fact that results can be obtained for a non-constant flux condition. This is especially significant for describing behaviour under constant injection and well flowing conditions as more often used in industry.

Acknowledgements

We would like to acknowledge NSERC for the financial support. We gratefully appreciate the computational contributions of Mr. Xiaolong Liu and Ms. Huan Yang.

References

Bratvedt, F., Gimse, T., Tegnander, C. 1996. Streamline Computations for Porous Media Flow Including Gravity. Transport in Porous Media, pp. 63-78.

Thiele, M., Batycky, R.P. and Fenwick, D.H. 2010, Streamline Simulation for Modern Reservoir – Engineering Workflows, J. Petr. Tech.-Distinguished Author Series, pp. 64-70.

Chorin, A.I., Random Choice Solutions to Hyperbolic Systems. 1976. J. Comput. Phys., 22, pp. 517-533.

Concus, P., Proskurowski. 1979. Numerical Solutions of a Nonlinear Hyperbolic Equation by the Random Choice Method, J. Comput. Phys., 30, pp. 153-166.

Glimm, J., Solutions in the Large for Nonlinear Hyperbolic Systems. 1965. Comm. Pure Appl. Math., 18, pp. 697-715.

Godunov, S.K. 1959. A Finite Difference Method for the Numerical Computation of Discontinuous Solutions of the Equations of Fluid Dynamics, Math. USSR Sb., 47, pp. 271-290.

Lax, P.D., Hyperbolic Systems of Conservation Laws II. 1957. Comm. Pure Appl. Math., 10, pp. 537-566.

Smoller, J. 1982. Shock Waves and Reaction-Diffusion Equations, Springer-Verlag, New York.

Buckley, S.E., and Leverett, M.C. 1941. Mechanism of Fluid Displacement in Sands, Petrol. Trans. AIME **146**, 107.

Welge, H.G. 1952. A Simplified Method for Computing Oil Recovery by Gas or Water Drive, Petrol. Trans AIME **195**, 91.

Rhee, H-K, Aris, A. and Amundson, N.R. 1970. Phil. Trans. Roy. Soc. London Ser. A. 267, pp. 419-455.

Johansen, T. and Winther, R. 1988. The Solution of the Riemann Problem for a Hyperbolic System of Conservation Laws Modelling Polymer Flooding, SIAM J. of Math. Anal., **19**(3), pp. 451-566.

Johansen, T. and Winther, R. 1989. The Riemann Problem for Multicomponent Polymer Flooding, SIAM J. of Math. Anal., **20**, pp. 909-929.

Dahl, O., Johansen, T., Tveito, A., Winther, R. 1992. Multicomponent Chromatography in a Two Phase Environment. SIAM J. Appl. Math. Vol. 52, No.1, pp. 65-104.

Johansen, T., Wang, Y., Orr, F.M.Jr. and Dindoruk, B. 2005. Four-Component Gas/Oil Displacement in One Dimension: Part I: Global Triangular Structure. Transp. In Porous Media, 61, pp. 59-76.

Wang, Y., Dindoruk, B., Johansen and Orr, F.M.Jr. 2005. Four-Component Gas/Oil Displacement in One Dimension: Part II: Analytical; Solutions for Constant Equilibrium Ratios. Transp. In Porous Media, 61, pp. 177-192.

Orr, F.M. Jr. 2007. Theory of Gas Injection Processes. Tie-Line Publication, Denmark.